The Dissertation Committee for Narae Yoon
certifies that this is the approved version of the following dissertation:

Characterization of, and Novel Architectures for, Strained-Layer Superlattice Infrared Photodetectors

Committee:

Daniel M. Wasserman, Supervisor

Jack Lee

Seth R. Bank

Leonard F. Register

Eric A. Shaner

Characterization of, and Novel Architectures for, Strained-Layer Superlattice Infrared Photodetectors

by

Narae Yoon

DISSERTATION

Presented to the Faculty of the Graduate School of

The University of Texas at Austin

in Partial Fulfillment

of the Requirements

for the Degree of

DOCTOR OF PHILOSOPHY

THE UNIVERSITY OF TEXAS AT AUSTIN

August 2019

To my parents, brother, and husband

Acknowledgments

First of all, I would like to thank my advisor, Professor Daniel Wasserman for his endless support, great patience, continuous encouragement and wise guidance to successfully conduct the research. Among many things, I specially thank him for giving me an opportunity to join Mid-IR Photonics group as an undergraduate to have my first research experience. I have no doubt that this opportunity has changed my life to start my Ph.D. study. I believe that five years of experience at University of Illinois at Urbana-Champaign and University of Texas at Austin have developed me to become a professional scientist. Needless to say, I could have not achieved any of it without his guidance. It is a great honor to be his first Ph.D. at UT-Austin.

I thank Prof. Erhan Kudeki at UIUC for the undegraduate scholarships. Without his recommendation letters, I could have not won any of those scholarships to complete my undergraduate study. I also thank Prof. John Dallesasse and Prof. Weng Cho Chew for writing me recommendations to win the Semiconductor Research Corporation (SRC) Fellowship, and I acknowledge Intel for this fellowship.

I also thank my committee members, Prof. Jack Lee, Prof. Seth Bank, Prof. Frank Register, and Dr. Eric Shaner, for offering helpful feedback on my work. I also would like to thank my collaborators from Air Force Research Laboratory (AFRL) at Wright-Patterson for growing superlattice materials, sharing external quantum efficiency results, and having insightful discussions.

I thank my brilliant labmates: Sukrith Dev, Leland Nordin, Abhilasha Kamboj, Kun Li, Zuoming Dong, and Yinan Wang. I especially thank Sukrith for chatting with me on

any topics. It was my pleasure to have a complete overlap of B.S., M.S., and Ph.D. study. I thank Dr. Daniel Zuo for teaching me how to perform EBIC measurement. I thank Leland for growing T2SL materials, and thank Abhilasha for helping me in many things. I also thank Dr. Runyu Liu for sharing his industry experience.

In addition, I would like to thank my loving friends, Ashley D Youn and Claire Jeong, for their presence for 10+ years. I also thank MRC friends, Soonil Lee, Yoonho Seo, Jae-Hyun Kim, Myungsoo Kim, Kyoungmin Yoo, Tae-Hyeon Kim, Dr. Seohee Kim, Dr. Kyounghwan Kim, and Dr. Joon-Seok Kim.

Lastly, I thank my husband, Dr. Saungeun Park, for his endless love and support.

Narae Yoon

Austin, Texas

August 2019

"Rejoice always, pray continually, give thanks in all circumstances; for this is God's will for you in Christ Jesus." - 1 Thessalonians 5:16-18 NIV

Characterization of, and Novel Architectures for, Strained-Layer Superlattice Infrared Photodetectors

Narae Yoon, Ph.D.
The University of Texas at Austin, 2019

Supervisor: Daniel M. Wasserman

The current generation of infrared photodetectors, used in imaging and sensing applications, are predominantly made of an expensive II-VI material, HgCdTe (mercury cadmium telluride, MCT). A viable alternative class of materials, the III-V type-II superlattices (T2SLs), have been actively studied due to several potential and predicted advantages over MCT. T2SLs offer an easier path to the design of arbitrarily small effective bandgaps by controlling the layer thickness, more uniform material growth across the wafer, significantly greater flexibility in detector architecture, reduced Auger recombination due to the light-hole and heavy-hole splitting, and theoretically higher operating temperatures at longer wavelengths. However, despite the proposed superior performance offered by T2SL-based detectors, this improved performance has not yet been realized, a fact largely believed to be a result of defects and growth imperfections in the T2SL materials. To improve the material quality, it is important to characterize and understand the carrier dynamics of T2SLs. The primary thrust of this thesis is the description and development of experimental techniques for characterizing T2SL detectors. The first part of this dissertation focuses on establishing a new approach to electron beam induced current (EBIC) measurements, used to study the diffusion characteristics of InGaAs/InAsSb superlattices. By measuring the current generated by the electron beam of a scanning electron microscope (SEM), EBIC allows us

to extract the minority carrier diffusion length (L) and the surface recombination velocity to diffusivity ratio (S/D) of a material. When combined with information on minority carrier lifetime (τ), for instance from time-resolved photoluminescence measurements, the minority carrier mobility (μ) of the material can be extracted. By performing TRPL and EBIC, InGaAs/InAsSb photodetectors with varying InGaAs Ga-fraction have been studied to show that the minority carrier mobility increases as the gallium composition increases.

In the second part of this dissertation, we investigate InGaAs/InAsSb detectors with varying unit cell thicknesses in order to characterize the minority carrier diffusion length as a function of layer thickness.

Carrier transport studies (including EBIC) of infrared (IR) detector materials typically focus on the vertical transport of minority carriers, as the photoexcited charge in these devices is almost always collected across a junction in the vertical (growth) direction. However, with the growing technological importance of IR focal plane arrays (FPAs), understanding the lateral diffusion of photo-excited carriers becomes increasingly important, particularly in quantum-engineered IR absorber materials such as T2SLs, whose layered design would be expected to give anisotropic charge transport properties. In the third portion of the dissertation we develop and discuss a technique for extracting the anisotropic carrier diffusion in T2SL materials. In order to extract both vertical and lateral minority carrier diffusion lengths of InGaAs/InAsSb superlattices, a two-dimensional electron beam induced current (2D-EBIC) technique is developed. The results from our 2D-EBIC studies show the lateral hole mobility to be between 3 to 5 times greater than the vertical hole mobility in 6 ML $In_{0.88}Ga_{0.12}As$ / 6 ML $InAs_{0.65}Sb_{0.35}$ superlattice material.

The final part of this dissertation proposes an architecture for enhanced absorption in ultra-thin strained-layer superlattice detectors utilizing a hybrid optical cavity design. The

proposed detector architecture utilizes a highly doped semiconductor ground plane beneath the ultra-subwavelength thickness long-wavelength infrared absorber material, upon which we pattern metallic antenna structures. Using realistic material parameters, the detector absorption achieves near 50 % in absorber layers with thicknesses of approximately $\lambda_o/50$. The detector absorption is investigated as a function of wavelength and incidence angle, as well as detector geometry. The proposed device architecture offers the potential for high efficiency detectors with minimal growth costs and relaxed design parameters.

Table of Contents

List of Tables

List of Figures

Chapter 1

Introduction

1.1 Infrared Light

The research described in this dissertation is focused on the investigation and characterization of materials used for infrared detection, and motivated by the technological importance of infrared detectors. While the infrared (IR) is often described as the region of the electromagnetic (EM) spectrum covering the wavelengths from 700 nm to 1 mm (longer than that of visible light and shorter than that of the microwave), such a description blurs the unique characteristics and applications of the smaller sub-regions that make up the IR. Waves in the longer wavelength portion (λ > 100 μm) of the greater IR range are most frequently referred as terahertz (THz) or sub-millimeter (sub-mm) radiation, which leaves the the 700 nm to 100 μm range as what is most commonly referred to as the infrared. Even across this smaller portion of the EM spectrum, the IR is can be further subdivided into the near IR (NIR) from 750 nm to 1 μm, the short-wavelength IR (SWIR) from 1 μm to 3 μm, the mid-wavelength IR (MWIR) from 3 μm to 8 μm, the long-wavelength IR (LWIR) from 8 μm to 15 μm, and the far IR (FIR) from 15 μm 100 μm, as shown in Figure 1.1.

The spectral ranges associated with these subcategories are chosen according to both atmospheric transmission bands and the peak emission of blackbody emitters as a function of temperature. Figure 1.2 shows the transmission of the atmosphere across the infrared, with two clear bands of transmission from 3 - 5 μm (the MWIR) and 8 - 14 μm (the LWIR). Overlaid on this figure is the normalized blackbody emission from an object

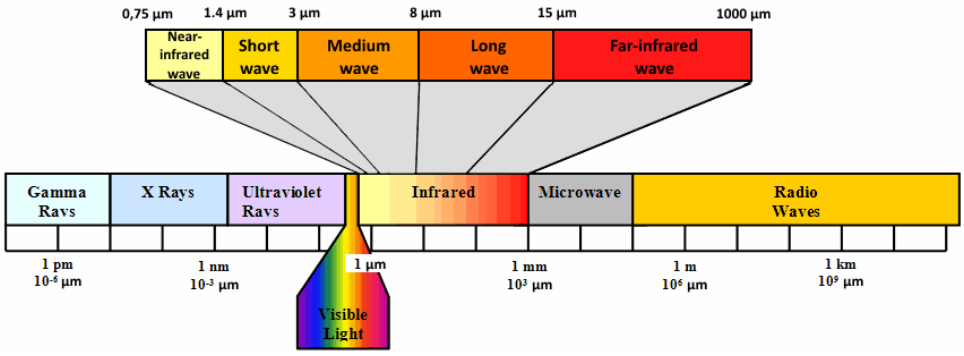

Figure 1.1: The electromagnetic waves with a highlight of IR spectrum, which shows subdivisions of IR ranges.

at 700 K (blue) and 300 K (red). Planck's Law of Blackbody radiation gives the spectral power density emitted from a perfect blackbody (a surface that absorbs 100 % of incident radiation, regardless of temperature). The spectral radiance per unit wavelength, L_λ, is defined as:

$$L_\lambda(\lambda, T) = \frac{2hc^2}{\lambda^5} \frac{1}{\exp\left(\frac{hc}{\lambda kT} - 1\right)}, \tag{1.1}$$

where h is Planck's constant, c is the speed of light, λ is the free space wavelength of the thermal emission, k is Boltzmann constant, and T is the temperature. The MWIR and LWIR are also referred as the thermal infrared: MWIR covers the 3 - 8 μm range, where objects, such as stars, jet engine exhaust, or turbines, have their operational temperature, much higher than that of the human body. As can be seen in Figure 1.2, this wavelength range overlaps with the 3 - 5 μm atmospheric transmission band. Thus, for detection of thermal emission from hot objects, the MWIR is the preferred spectral band. The LWIR, on the other hand, covers the 8 - 15 μm range, overlapping with the longer wavelength IR atmospheric transmission band, and is generally associated with the blackbody temperatures of biological objects (such as human beings). The overlap of the atmospheric transmission bands with

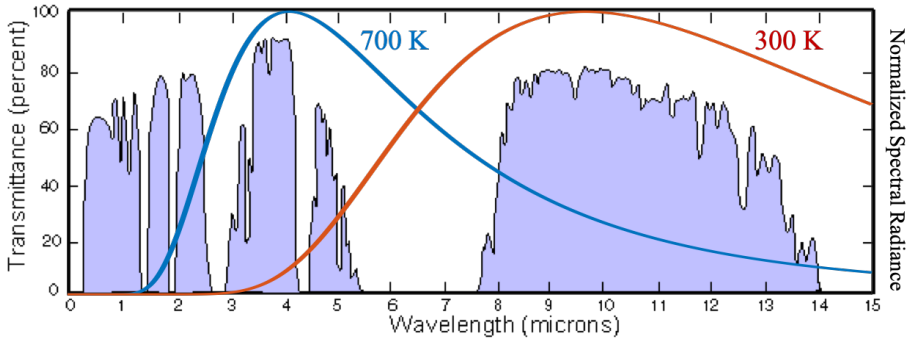

Figure 1.2: The atmospheric transmission in the infrared regime [2] is plotted, and the normalized spectral radiance profiles at 700 K (blue) and 300 K (red) are overlaid.

both "hot" and "biological" objects points to a significant technological motivation behind the development and optimization of IR detectors, namely the ability to image and/or track mechanical or biological objects without ambient lighting. Thus, infrared detectors have gained a significant interest for a range of applications related to thermal imaging, such as night vision, astronomy spectroscopy, IR countermeasures, and military target acquisition.

However, IR imaging applications are far from the only technology driving the development of IR detectors. A wide range of molecules absorb infrared light at wavelengths determined by the masses of the molecular elements and their bonding energies [10]. The absorption from such molecules typically consists of a large number of strong and narrow absorption lines (most often in the 3 - 12 μm range), corresponding to different molecular resonances [10]. The combination of these resonances provides a unique absorption spectra for each molecule. For this reason, the mid-IR wavelength range is often referred to as the "molecular fingerprint" portion of the EM spectrum, due to the uniqueness of each molecular absorption spectra. The approximate location of the strongest absorption resonances for a range of technologically important molecules is shown in Figure 1.3. Optical detection provides an accurate and sensitive measure of the presence (and concentration) of any of these strongly absorbing molecules. Thus optical sensing serves as another significant

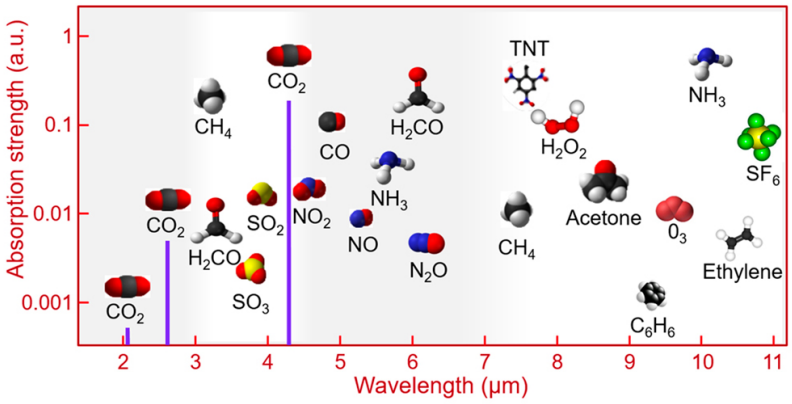

Figure 1.3: The strongest absorption resonances for several technologically important molecules as a function of wavelength in IR regime [3].

driving motivation for the development of infrared detectors.

1.2 Infrared Detection

1.2.1 Thermal detectors

The first IR detectors demonstrated generally fell into the class of detectors known as thermal detectors. Such detectors provide a signal resulting from a change in the temperature of the detecting element. In 1800, Herschel used a thermometer to demonstrate that the emission from sun included infrared rays [11]. A subclass of thermal detectors, the bolometer, uses the temperature dependence of the absorbing element's resistance to measure the absorbed power. The first bolometer was invented by Langley in 1880, and consisted of two thin platinum foil ribbons, one covered in lamp-black and facing the thermal source, the other uncovered. The two ribbons were integrated as two arms in a Wheatstone Bridge configuration, with the lamp-black ribbon's photo-dependent resistance determining the read out voltage across the bridge. It was said that Langley's bolometer was so sensitive it could detect a cow from 1/4 mile away [12]. From their first demonstration, bolometers

have proven to be extremely sensitive detectors. However, they are quite slow, and generally tend to have limited dynamic range. For a large number of applications, photon detectors are much preferred to bolometers. Photon detectors convert incident light to excited charge carriers (instead of heat, as is the case in a thermal detector), capable of conducting current.

1.2.2 Photoconductive devices

The first demonstrations of IR photon detectors typically utilized narrow bandgap semiconductors as the photoconductive absorber. In such photoconductors, the conductivity of the material is altered when incident light excites an electron from the valence band to the conduction band of the semiconductor, where it is able to carry current. The bandwidth of a photoconductor is thus limited by the semiconductor bandgap, and for IR detection, narrow bandgap materials are required. Lead sulphide (PbS) was introduced as a photoconductive material in 1945, and extrinsic Hg-doped germanium (Ge) was used as a photodetector. The range of these materials was limited, however, with PbS and Ge having bandgap of 3.3 μm and 1.8 μm, respectively [13]. A number of ternary narrow bandgap semiconductor alloys such as $InAs_{1-x}Sb_x$, $Pb_{1-x}Sn_xTe$, and $Hg_{1-x}Cd_xTe$ have also been actively studied, where the material's bandgap can be controlled by choice of the alloy composition. However, photoconductors are less than an ideal choice for IR detection applications. The narrow band gaps required for such materials guarantee significant intrinsic carrier concentrations and thus dark currents, which will reduce detector figures of merit.

1.2.3 Photodiodes

The key principle of a photodetector is to collect excess charge carriers that are generated by incident and absorbed photons. For such a device it is the minority excess carriers that are the most important, since the electron and hole recombination occurs

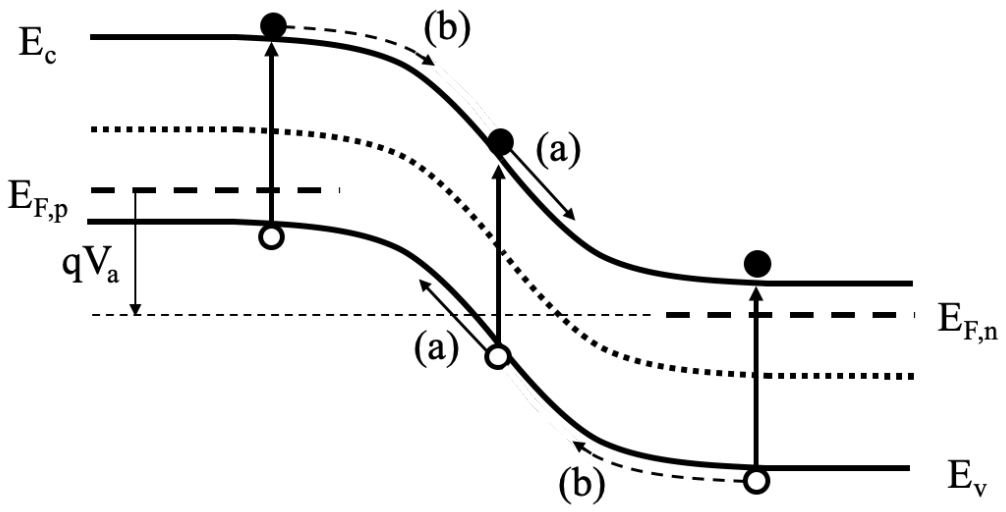

Figure 1.4: Band diagram of a reverse-biased p-n junction, showing the conduction and valence band edges (E_C and E_V) and the Fermi levels ($E_{F,p}$ and $E_{F,n}$ for p-type and n-type, respectively). In the depletion region at the junction, generated electron hole pairs (a) are separated by the electric field to produce current. Additionally, minority carriers outside of the depletion region (b) can diffuse to the depletion region and then be swept to the opposite side.

as a pair, and the minority excess carriers ultimately limit the recombination process (the differential change in majority carriers is minimal compared to that of the minority carriers). By employing the potential difference in a reverse-biased p-n junction, the photo-generated excess carriers can be more efficiently collected as current. Figure 1.4 shows a band diagram of a reverse-biased p-n junction, and illustrates (a) the photo-generated excess carrier that is swept by the electric field or (b) the excess carriers that diffuse into the depletion region. Since the excess minority carriers that are outside of the depletion region can still contribute to current if they are able to diffuse to the electric field in the junction, an improvement in minority carrier diffusion length can enhance the detector quantum efficiency. In order to increase the probability of photo-generated carriers getting collected as current, the intrinsic semiconductor can be inserted between the p and n type materials in order to lengthen the depletion region. Such a photodetector architecture is referred as a p-i-n photodiode.

However, the pn or p-i-n photodiode are not the only detector architecture available for IR detection applicaitons. There are other types of photodetector architectures, such as nBn [14], CBIRD (complementary barrier infrared detector) [15], and W- or M-structured graded bandgap structures [16, 17], which may have significant advantages over the pn junction photodiode in the mid-IR. While the graded bandgap structures utilize the superlattices to engineer the gradually increasing bandgaps, both nBn and CBIRD are the structures that utilize the wide bandgap material, referred as the barrier, which work as a carrier blocking layers. One of the barrier-utilizing structures, the nBn, was first demonstrated in 2006 [14]. The nBn structure consists of an n-type top contact layer, a carrier blocking undoped barrier layer, and an n-type absorbing semiconductor. Photocurrent is carried by the photoexcited minority carriers (holes, in this case), while the barrier acts to prevent majority carrier current from flowing in the device (and thus minimize dark current). Figure 1.5 shows a band alignment of an nBn structured photodetectors that is biased under the operating conditions. This structure has gained lots of attention due to the reduced dark current and its theoretically higher operating temperatures compared to other infrared detectors, such as p-n photodiodes [14], which will be further discussed in Chapter 1.4.

Before providing a deeper discussion of the history and recent development in IR photodetector materials and architecture, it is vital to understand the various figures of merit that are used to determine the suitability of a photodetector for IR imaging or sensing applications.

1.3 Figures of Merit

There are several figures of merit that help us to evaluate the operation and efficiency of photodetectors. These figures of merit can depend not only on the intrinsic material properties of the IR absorber material, but also the detector architecture employed. The

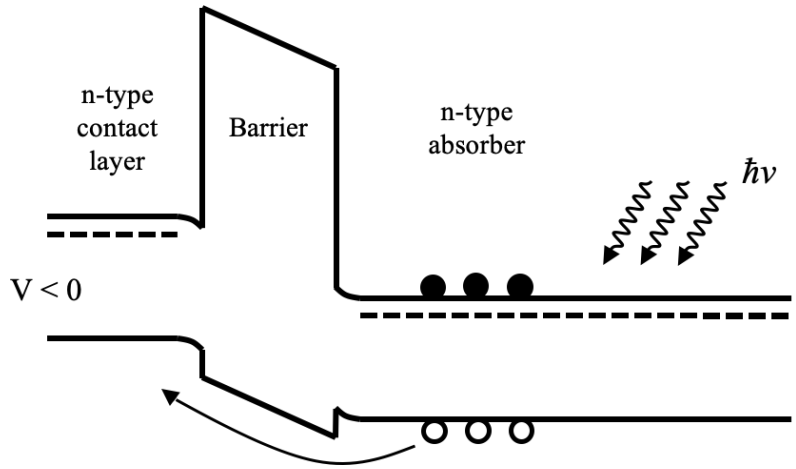

Figure 1.5: Band gap alignment of an nBn detector with a negative bias applied to the n-type contact layer. When the electron and hole pairs are generated by absorbed photons, the minority carriers (holes) contribute to current while the majority carriers (electrons) are blocked by a barrier.

performance of a photodetector can in large part be described by its cut-off wavelength, λ_c, absorption coefficient, α, carrier lifetime, τ, quantum efficiency, η, responsivity, $R(\lambda)$, noise equivalent power, NEP, detectivity, D^*, and dark current, I_{Dark}. In this section, these figures of merit are briefly explained.

1.3.1 Cut-off wavelength

The cut-off wavelength, λ_c, of a photodetector is the maximum wavelength of a photon that can be absorbed by the light-absorbing material in the photodetector. The cut-off wavelength is related to the band gap (or effective bandgap, for a superlattice), E_g, of the material as shown in Equation 1.2.

$$\lambda_c = \frac{hc}{E_g} \approx \frac{1.24\ [\mu m \cdot eV]}{E_g\ [eV]} \tag{1.2}$$

where h is Planck's constant and c is the speed of light in a vacuum. The infrared photodetector material of choice for the MWIR, InSb, has a cut-off wavelength of 5.5 μm at 77 K, and any light of free-space wavelength longer than this value will not be absorbed,

and thus not detected. Thus InSb is only used for MWIR applications, and is unsuitable for the LWIR. The ternary material system, HgCdTe (MCT), can have a range of cut-off wavelengths (from 1 - 30 μm), since the band gap of MCT varies depending on alloy composition. Similarly, the effective band gap of the type-II superlattices (T2SLs, deeper discussion in Chapter 1.4.3) can also be engineered by adjusting the layer thicknesses and constituent alloys, or alloy composition. Since changing the layer thickness of a T2SL is much easier than controlling the molar composition of MCT [18], T2SLs can offer better material uniformity and thus more uniform optical properties across an epitaxially-grown wafer. The cut-off wavelength or the band gap of absorbing material is often experimentally studied via photoluminesence measurements, which will be discussed in Chapter 2.1. When using experimental absorption spectra, the cut-off wavelength can be more difficult to determine, as the rising edge of absorption in these narrow bandgap materials is often (usually) not sharp. Thus, the cut-off wavelength is usually chosen to be the position half-way up the edge of the absorption turn-on [19]. Cut-off wavelength is purely an optical property associated with the absorber material chosen for any detector architecture.

1.3.2 Absorption coefficient

The absorption coefficient of a material, $\alpha(\lambda)$ gives the rate of decrease in light intensity for a plane wave propagating through the material, due to any light-absorbing mechanism. For photodetector absorber materials, larger absorption coefficients are almost always more desirable, as this indicates that more light can be absorbed in thinner materials, thus improving both internal and external quantum efficiency. Equation 1.3 shows the relationship between the incident light intensity and the transmitted light intensity.

$$I(\lambda) = I_o(\lambda)e^{-\alpha(\lambda)z}, \tag{1.3}$$

where $I_o(\lambda)$ is the incident light intensity, $I(\lambda)$ is the transmitted light intensity, $\alpha(\lambda)$ is the absorption coefficient, and z is the distance from the surface of the material. The absorption coefficient is typically given in units of cm^{-1}, and can be thought of as the inverse of the depth δ at which the light intensity decreases to $1/e$ of its value at the surface of the material ($\delta = 1/\alpha$). Beer's Law gives the transmittance, T, through a material as a function of position, where T is equal to $\frac{I}{I_o}$, and the absorbance, is defined as given in Equation 1.4:

$$A(\lambda) = -\log(T(\lambda)) = -\log\left(\frac{I}{I_o}\right). \tag{1.4}$$

As a result, the absorption coefficient, $\alpha(\lambda)$, can be extracted from the experimental measurement discussed in Chapter 2.4, as shown in the following equation:

$$\alpha(\lambda) = -\frac{1}{t}\ln\left(\frac{I(\lambda)}{I_o(\lambda)}\right) = \frac{A(\lambda)}{t}\ln(10) = 2.3026 * \frac{A(\lambda)}{t}, \tag{1.5}$$

where $A(\lambda)$ is the absorbance and t is the thickness of the material.

1.3.3 Carrier Lifetime

The carrier lifetime, or more accurately described as the minority carrier lifetime, is defined as the average time it takes for an excess minority carrier to recombine. The effective carrier lifetime consists of a bulk carrier lifetime, τ_{bulk}, and the surface recombination carrier lifetime, τ_s, as shown in Equation 1.6:

$$\frac{1}{\tau_{eff}} = \frac{1}{\tau_{bulk}} + \frac{1}{\tau_s}. \tag{1.6}$$

In the bulk material, the carriers recombine by either radiative recombination or non-radiative recombination: the latter most often coming from Shockley-Read-Hall (SRH) or Auger recombination. The overall bulk carrier recombination rate ($\propto \frac{1}{\tau_{bulk}}$) can be expressed as a sum of the above recombination rates:

$$\frac{1}{\tau_{bulk}} = \frac{1}{\tau_{rad}} + \frac{1}{\tau_{SRH}} + \frac{1}{\tau_{Auger}}. \tag{1.7}$$

where τ_{rad} is the radiative lifetime, τ_{SRH} is the SRH lifetime, and τ_{Auger} is the Auger lifetime. Since the carrier lifetime is directly related to several different recombination mechanisms, it is important to understand each of the generation/recombination processes.

Recombination Mechanisms

To study IR photodetectors, it is crucial to understand the carrier generation and recombination processes in the semiconductors used as IR absorbing material. In general, there are two types of carrier generation-recombination processes: 1) radiative processes which involves the creation or annihilation of photons, and 2) non-radiative processes which involve the interaction with phonons and/or the energy and momentum exchange via another electron or hole. In this section, the radiative band-to-band process, non-radiative Shockley-Read-Hall, and the non-radiative Auger process will be discussed.

Band-to-band

The radiative band-to-band transition in a semiconductor is described in Figure 1.6, which shows the carrier generation and recombination between the valence band and the conduction band of the semiconductor [20, 21].

In equilibrium, or steady state, the generation rate of electrons, G_n, and the generation

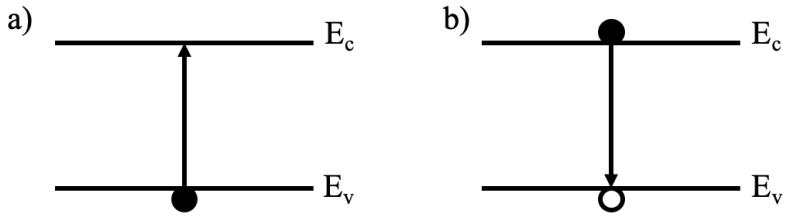

Figure 1.6: The illustration of the radiative band-to-band a) generation and b) recombination in a semiconductor that has the valence band, E_v, and the conduction band, E_c.

rate of holes, G_p are equal to the emission rate, e_r, due to the thermal or optical process:

$$G_n = G_p = e_r. \tag{1.8}$$

In addition, the radiative recombination rates of electrons and holes are proportional to the electron and hole concentrations:

$$R_n = R_p = Bnp, \tag{1.9}$$

where R_n is the electron recombination rate, R_p is the hole recombination rate, B is the bimolecular recombination coefficient, n is the electron concentration, and p is the hole concentration.

Under the low-injection regime, where the excess electron and hole concentrations $\delta n, \delta p \ll (n_o + p_o)$, the radiative lifetime can be expressed as the following:

$$\tau_{rad} \simeq \frac{1}{B(n_o + p_o + \delta n)}, \tag{1.10}$$

where δn is the excess carrier concentration generated by the electrical or the optical injection and n_o and p_o are the equilibrium electron and hole concentrations, respectively [20].

Shockley-Read-Hall

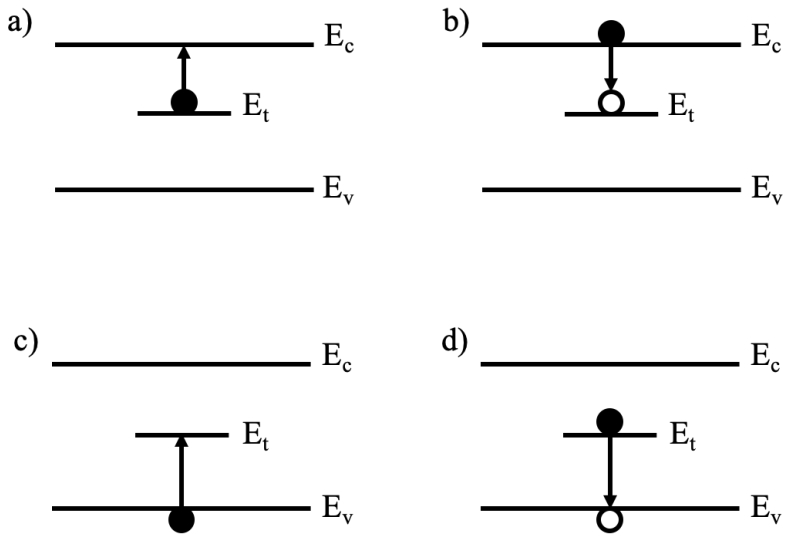

Figure 1.7: The illustration of the non-radiative Schokley-Read-Hall a) electron emission, b) electron capture, c) hole emission, and d) hole capture in a semiconductor that has the valence band, E_v, the conduction band, E_c, and the trap state, E_t.

The Shockley-Read-Hall (SRH) process is a type of non-radiative process, mainly resulting from crystalline defects and impurities in the semiconductor lattice [20]. These defects (including vacancies, interstitial atoms, and dislocations) change the periodic structure of the crystal and generate trap states where the electrons and holes most often recombine non-radiatively. The SRH recombination rate is proportional to the trap density:

$$R_{SRH} = \sigma \nu_{\mathrm{th}} N_{\mathrm{t}} \delta n, \tag{1.11}$$

where σ is the capture cross section, ν_{th} is the thermal velocity of the electron, N_{t} is the trap density, and δn is the excess carrier concentration. Figure 1.7 shows four generation/recombination processes with a defect energy state, E_{t}.

In Figure 1.7 a), the electron emission (from a trap state) rate is $G_n = e_n N_t f_t$, where e_n is the electron emission coefficient, N_t is the trap concentration, and f_t is the probability of the trap in consideration being occupied by an electron. In Figure 1.7 b), the electron

capture rate is $R_n = c_n n N_t(1 - f_t)$, where c_n is the capture coefficient for electrons, n is the electron concentration, and $(1 - f_t)$ is the probability of traps that are empty. In Figure 1.7 c), the hole emission rate is $G_p = e_p N_t(1 - f_t)$, where e_p is the hole emission coefficient. In Figure 1.7 d), the hole capture rate is $R_p = c_p p N_t f_t$, where c_p is the capture coefficient for holes and p is the hole concentration.

At thermal equilibrium, there is no net generation-recombination of electrons and holes: $R_n - G_n = R_p - G_p = 0$. Based on the generation and recombination rate expressions as a function of c_n, c_p, e_n, and e_p, the net recombination rate, R, can be shown as in Equation 1.12 [20].

$$R = \frac{np - n_i^2}{\tau_p(n + \frac{e_n}{c_n}) + \tau_n(p + \frac{e_p}{c_p})}, \tag{1.12}$$

where the hole lifetime is $\tau_p = 1/c_p N_t$, and the electron lifetime is $\tau_n = 1/c_n N_t$. Under the low-level injection condition, $\delta n << N_D$, the net recombination rate is $R = \frac{\delta n}{\tau_o}$. As a result, the carrier lifetime due to SRH processes is expressed as the following [20]:

$$\tau_{SRH} = \frac{\tau_p(n + \frac{e_n}{c_n}) + \tau_n(p + \frac{e_p}{c_p})}{(n_o + p_o)} \tag{1.13}$$

Auger

Auger generation/recombination is another type of non-radiative process. Auger generation occurs when an energetic electron's energy is given to a bound charge carrier (impact ionization), and generates an electron-hole pair, as illustrated in Figure 1.8 (a) and (b). When the electron and hole recombine (Auger recombination), instead of generating a photon, the energy is transferred to the nearby electron (or hole). This causes the nearby electron (or hole) to get excited to the upper state (or the lower state), as described in Figure 1.8 (c) and (d).

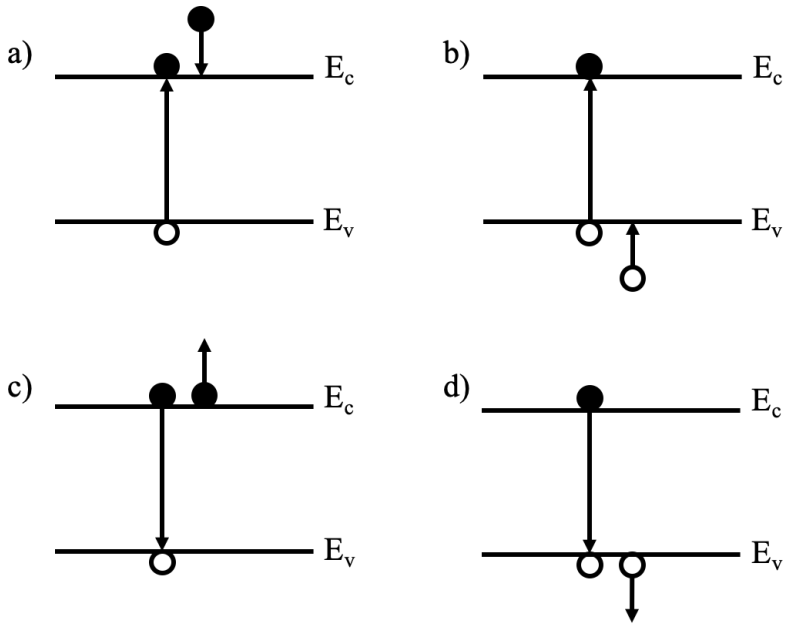

Figure 1.8: Illustration of the non-radiative Auger generation and recombination processes. a) Electron emission occurs when a high energy electron in the conduction band impact ionizes, generating an electron-hole pair. b) Hole emission occurs when a high-energy hole in the valence band impact ionizes, also generating an electron-hole pair. c) Electron capture occurs when the electron and hole recombine, and the resulting energy generated is transferred to a nearby electron which is then excited to higher energy states in the conduction band. d) Hole capture occurs when the electron and hole recombine, and instead of generating a photon, the resulting energy is transferred to a hole, exciting the hole to higher energy states in the valence band. In this figure, E_c represents the conduction band, while E_v denotes the valence band.

For the electron emission process, as shown in Figure 1.8 (a), the energetic electron impact ionizes a valence band electron, which then causes the valence band electron to be excited to the conduction band. During this process, the electron and hole pair is generated with the rate of $G_n = e_n n$. The hole emission process is described in Figure 1.8 (b). In this process, an energetic hole impact ionizes a valence band electron, generating an electron-hole pair with the rate of $G_p = e_p p$. During the electron capture process (Figure 1.8 (c)), the recombination of electron and hole excites the nearby electron to a higher state in the conduction band. This process has a recombination rate of $R_p = C_p n p^2$. When the electron and hole recombine, instead of generating a photon, the energy associated with the recombination process excites a nearby hole to a higher energy state in the valence band. This is the hole capture process with the generation rate of $G_p = e_p p$, and is illustrated in Figure 1.8 (d).

At thermal equilibrium, there is no net generation/recombination: $R_n - G_n = C_n n_o^2 p_o - e_n n_o = 0$. This gives: $e_n = C_n n_o p_o = C_n n_i^2$, and similarly, $e_p = C_p n_i^2$. The total net Auger recombination rate, R_{Aug}, can be expressed as the following equation [20]:

$$\begin{aligned} R_{Aug} &= R_n - G_n + R_p - G_p \\ &= C_n n^2 p - e_n n + C_p p^2 n - e_p p \\ &= C_n n^2 p - C_n n_i^2 n + C_p p^2 n - C_p n_i^2 p \\ &= C_n n(np - n_i^2) + C_p p(np - n_i^2) \\ &= (C_n n + C_p p)(np - n_i^2). \end{aligned} \tag{1.14}$$

Under the high-level injection condition, $n = p >> n_i^2$, the total Auger recombination rate, $R_{Auger} = Cn^3$. The Auger coefficient C_n and C_p increase exponentially with the inverse of the semiconductor bandgap. This, combined with the cubic dependence

on carrier concentration, indicates the potentially significant contribution from Auger processes in devices with narrow bandgaps, and/or high doping, elevated temperatures, and high injection.

1.3.4 Quantum efficiency

The quantum efficiency of an absorber material, η, is ratio of the collected charge carriers to incident photons. This is sometimes referred as an external quantum efficiency, η_{ext}, which can be expressed as a function of the injected optical power, P_{opt}, and the collected photocurrent, I_{ph}:

$$\eta_{ext} = \frac{I_{\text{ph}}}{P_{\text{opt}}} \frac{hv}{q}. \tag{1.15}$$

The intrinsic quantum efficiency, η_{int}, also commonly used, is perhaps a better indicator of the intrinsic charge collection efficiency of an IR detector architecture. The intrinsic quantum efficiency is the ratio of collected charge carriers to absorbed (not incident) photons. This requires a conversion from the number of incident photons to the number of absorbed photons, so that the intrinsic quantum efficiency is simply the external quantum efficiency divided by the absorbance:

$$\eta_{\text{int}} = \frac{\eta_{ext}}{(1-R)(1-e^{-\alpha d})}, \tag{1.16}$$

where R is the reflectivity between the air and semiconductor, α is the absorption coefficient of the semiconductor, and d is the thickness of the absorbing material (ignoring any cavity or secondary reflection effects).

For a photodetector, the internal quantum efficiency, η_{int}, is the probability that a photo-generated carrier, excited by an absorbed photon in a detector structure, will be collected and converted into an electrical signal. The external quantum efficiency, η_{ext}, on the other hand, is the probability that an photon incident upon the detector will be collected as an electrical signal. Thus, external quantum efficiency takes into account the probability that the photon enters the photodetector material and the probability that it is then absorbed by the material (as well as the internal quantum efficiency).

1.3.5 Responsivity

Responsivity, $R(\lambda)$, also commonly referred to as spectral responsivity, is the ratio of the electrical output per optical input as shown in Equation 1.17.

$$R(\lambda) = \frac{\Delta I}{P_{\text{opt}}} \frac{[A]}{[W]} \tag{1.17}$$

where ΔI is the output photocurrent in Amperes and P_{opt} is the incident optical power in Watts. The higher responsivity of a detector indicates that the optical incident power is more efficiently converted to the output photocurrent, which is desirable for any photodetectors. Spectral responsivity is material dependent, but will also depend on the design and geometry of the chosen photodetector architecture.

1.3.6 Noise Equivalent Power

The noise equivalent power (NEP) is the incident power that produce a signal-to-noise ratio (SNR) of 1 in a bandwidth of 1 Hz [20, 22]. NEP can be expressed in terms of responsivity, $R(\lambda)$:

$$\text{NEP} = \frac{I_n}{R(\lambda)}[W], \tag{1.18}$$

where I_n is the output noise current, and $R(\lambda)$ is the current spectral responsivity. While the responsivity is an important metric for understanding detector performance, the noise

associated with any detector material or architecture is often the limiting factor in detector performance. Minimizing the intrinsic noise in any semiconductor is often the single most important concern in detector design. The dark current is related to the noise, as such that the increase in dark current causes more fluctuations in current, and results in more noise.

1.3.7 Detectivity

The specific detectivity, D^* is the inverse of NEP, normalized per sqaure root of the detector area, A, and the frequency bandwidth, Δf, as suggested by Jones [20]:

$$D^* = \frac{\sqrt{A\Delta f}}{\text{NEP}}. \tag{1.19}$$

The unit for the specific detectivity is cm$\sqrt{\text{Hz}}$/W, which is often called "Jones." More discussions on the specific detectivity of the state-of-the-art photodetectors will be discussed in Chapter 1.4. The specific detectivity is usually the single most important figure of merit used to compare detectors across a range of materials and architectures.

1.3.8 Dark current

Dark current, as the name suggests, is the current through a photodetector when no light is incident upon the detector. In Figure 1.9, four main mechanisms of the dark current are illustrated, and the dark current, I_{Dark} can be expressed as Equation 1.20:

$$I_{\text{Dark}} = I_{\text{Auger}} + I_{\text{SRH}} + I_{\text{TAT}} + I_{\text{Surface}} \tag{1.20}$$

where I_{Auger} is the Auger generation current, I_{SRH} is the Shockley-Read-Hall (SRH) current, I_{TAT} is the trap-assisted tunneling (TAT) current, and I_{Surface} is the surface leakage current.

Auger generation current is the current resulting from Auger generation processes, where a high energy charge carrier impact ionizes a bound charge and creates an electron-hole pair. If the charge from the Auger-excited electron-hole-pair is collected, a current

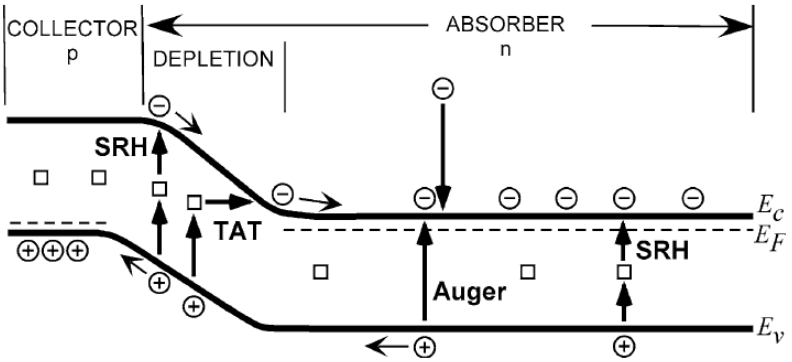

Figure 1.9: The illustration of several dark current mechanisms in a p-n homojunction: Shockley-Read-Hall (SRH), trap-assisted-tunneling (TAT), and Auger current [4]. The square signs indicate the mid-gap generation/recombination centers.

is produced without photo-illumination. The carrier concentration dependence of Auger processes generally means that Auger current can be large, and dominate the dark current, for high temperatures or higher doping concentrations. SRH current is another type of the dark current, where charge carriers are excited via trap or defect states in the bandgap of the detector. At low injection, SRH currents can be the dominant dark current mechanism for IR detectors, and minimizing SRH processes is key for developing high quality IR detectors. TAT current is generated when the electron is excited to the trap states and tunnels to the conduction band. In the sub-section of Chapter 1.3.3, more detailed explanations of the various recombination/generation mechanisms listed above are discussed.

The dark current is not desirable for any photodetector, essentially resulting in a current not associated with any incident IR illumination. Due to the statistical nature of the carrier generation and current flow processes, there will be a noise associated with the dark current: $I_n \propto \sqrt{2qI_{dark}}$ [23]. The reduction in each dark current mechanism is thus a fundamentally important subject of investigation for next generation IR detectors. Chapter 1.4 will discuss how artificially engineered materials can reduce dark current in IR detectors.

1.4 State-of-the-art IR Photodetectors

In this section, state-of-the-art narrow bandgap photodetectors and quantum dot and quantum well infrared photodetectors are discussed. Subsequently, the relatively new, artificially engineered, type-II superlattices (T2SLs) materials, the subject of the majority of this thesis, will be discussed at some length.

1.4.1 Narrow bandgap semiconductors

The vast majority of commercial IR photodetectors use either InSb or HgCdTe (mercury cadmium telluride, MCT) p-n junctions in a photodiode architecture. Between the two, the MCT is the more wavelength flexible, as InSb detector cut-off wavelengths are fixed at 5.5 μm, the position of the low-temperature InSb bandgap, while MCTs offer cut-off wavelengths ranging from 1 to 30 μm depending on alloy composition. MCT detectors have been the market dominant infrared photodetector since the 1960's, and significant effort has gone into the characterization and optimization of MCT detectors. Although material quality has been greatly improved and the band structure has well been studied, MCT detectors have several limitations: control of alloy composition is difficult, and for this reason, large-area, uniform epitaxial growth of MCT is challenging. In addition, significant Auger recombination limits the minority carrier lifetime, as is the case in any narrow bandgap bulk semiconductor.

1.4.2 Quantum well infrared photodetectors

Narrow bandgap materials are not the only semiconductors capable of providing IR photodetection. Significant effort has gone into the development of alternative IR absorbing materials with an eye towards supplanting MCT as the dominant IR detector material system. One particularly promising approach focused on the design of IR photodetectors based

on intersubband transitions in engineered heterostructures. Engineered semiconductor heterostructures allow for bandstructure engineering and the ability to design intersubband or intersublevel optical absorption in semiconductor materials. The intersubband optical absorption spectrum from the ground state to first excited state transition in a semiconductor quantum well can be expressed as the following [20]:

$$\alpha(\hbar\omega) = \frac{\omega}{n_r c \epsilon_o} \frac{|\mu_{21}|^2 \gamma}{(E_2 - E_1 - \hbar\omega)^2 + \gamma^2} \frac{m_e^*}{\pi \hbar^2 L_w} (E_2 - E_1), \tag{1.21}$$

where the intersubband dipole moment is given by $\mu_{21} = e \int_0^{L_w} \phi_2(z) z \phi_1(z) dz$. The simplest way to engineer this absorption spectrum is to adjust the width of the quantum well, L_w. Figure 1.10 (a) shows the bound-to-bound state transition, and Figure 1.10 (b) shows the bound-to-continuum transition. For the bound-to-bound state transition, the excited electrons need either thermionic emission or tunneling to get collected as current. Thus, it is desirable to design the upper level to be close to the barrier energy, so that the intersubband dipole moment and the escape probability can be optimized. For the bound-to-continuum transition, the width of the well, L_w, should be small enough to contain only one bound state. Although the photoexcited electrons sit in continuum states, and thus more easily contribute to the current, the intersubband dipole moment between the bound state to continuum may be smaller than that of a bound to bound transition, due to the large spatial extent of the continuum states and thus the reduced overlap of the bound and continuum wavefunctions.

Since the intersubband dipole matrix element between bound states in QWs will be in the growth direction, QWIPs require surface structuring (gratings, usually) to couple incident light into the TM-polarization capable of exciting the QW electrons. A structure similar to the QWIP utilizes quantum dots in place of quantum wells (and is thus refered to as a quantum dot infrared photodector, or QDIP), which allows for absorption of normal

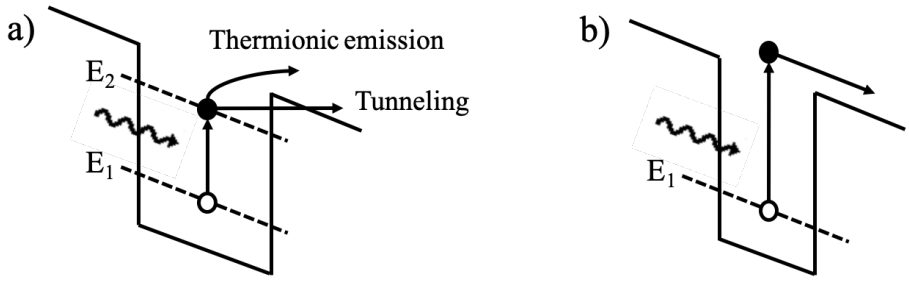

Figure 1.10: Two types of state transitions in a biased quantum well infrared photodetector (QWIP) with different widths of the quantum well. (a) Bound-to-bound state transitions from the ground state to the first excited state, which requires either thermionic emission or tunneling to generate current. When the well is designed to have a single bound state, the carriers will be excited from the ground state to the continuum , called (b) bound-to-continuum state transition.

incidence light without coupling structures, due to the vertical and lateral confinement of states in the 3D QD nanostructures.

While it might seem that QDIPs offer the greatest potential for supplanting the MCT as IR detector of choice, these IR detectors have gained little to no foothold as commercially available IR detectors. QWIPs, on the other hand, have gained a niche market, particularly for ultrafast IR detection for some sensing modalities [24, 25, 26].

1.4.3 Type-II Superlattice (T2SL)

In 1970, it was recognized that periodic layering of semiconductor materials with varying bandgaps resulted in an engineered 'superlattice' on top of the atomic lattice of the constituent semiconductors [27]. This superlattice structure results in the formation of minibands of allowed energies, when the period of the superlattice is on the order of the electron (and/or hole) wavelength. Early superlattices used materials with type-I band offsets (Figure 1.11 (a)), such that the resulting minibands were positioned entirely in the conduction and valence bands of both constituent materials. However, utilization of constituent materials with type-II offsets, either staggered or broken gap (Figure 1.11

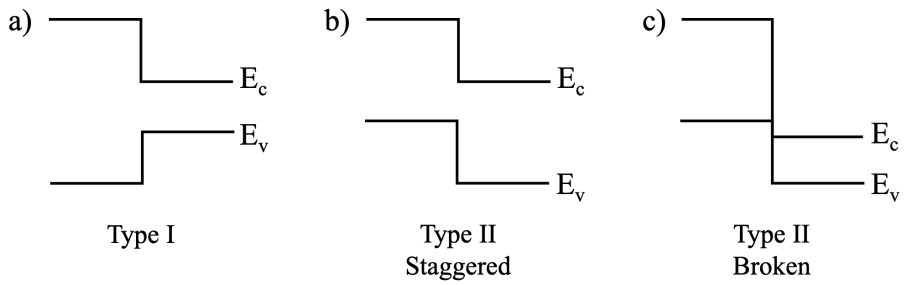

Figure 1.11: Three different types of the band alignment: (a) type-I, (b) type-II staggered, and (c) type-II broken (or type-III) band alignment.

(b,c)) can result in superlattice minibands where the highest valence miniband and lowest conduction miniband are separated by energies less than the bandgap of either of the constituent materials. Such a system allows for significant flexibility in the design of artificial semiconductors with effective bandgaps across a wide range of frequencies. Not surprisingly, the above superlattices, often referred to as type-II superlattices (T2SLs), quickly gained interest as potential materials for infrared detection [28, 29, 30, 31].

One example of the type-II superlattice (T2SL) material system is InAs/GaSb. The band alignment of an InAs/GaSb T2SL is illustrated in Figure 1.12, where both the conduction and valence band of the GaSb sit above the conduction band of the InAs. When alternating layers of GaSb and InAs are grown epitaxially, electrons are confined in the InAs conduction band quantum wells and holes in the GaSb valence band quantum wells. For short T2SL periods, the confined states in the superlattices overlap, forming the minibands shown.

There are multiple advantages of the T2SL materials over standard narrow band bulk semiconductors for IR detection applications. The first is the relative ease in controlling the effective band-gap of the T2SL by control of the layer thicknesses and composition. Most T2SLs designed for IR absorption utilize III-V semiconductor materials, whose epitaxial

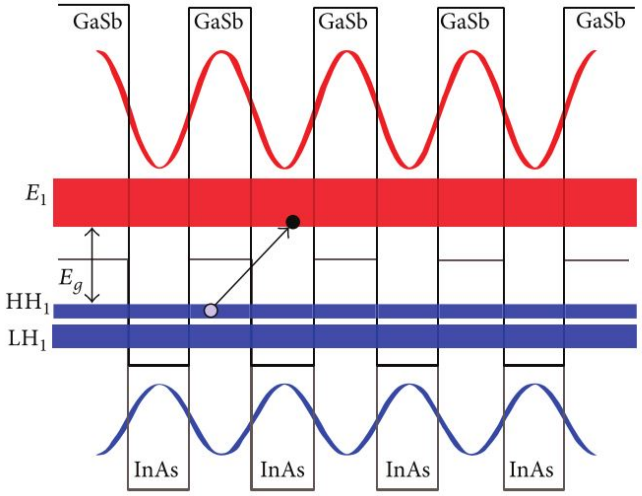

Figure 1.12: The type-II band alignment of InAs/GaSb T2SL is illustrated with an effective band gap that is employed for infrared detection [5].

growth is technologically mature and controllable, resulting in growth uniformity over large area wafers [32]. In addition, and perhaps most importantly, T2SLs are predicted to suppress Auger recombination when compared to the bulk semiconductors with equivalent bandgaps [33, 34, 35, 36, 37]. However, the benefits associated with longer non-radiative recombination times (improved diffusion lengths and thus collection efficiency) are offset by weaker absorption in the T2SL [38, 39], an important trade-off which must be considered when designing IR detectors. Not surprisingly, these advantages associated with T2SLs have resulted in significant investigation into their potential as viable alternatives to the current market-dominant MCT detectors.

After the advent of T2SLs, many different approaches for improving the infrared detection properties of the T2SL were investigated. A brief timeline of the T2SL history is shown in Figure 1.13, Figure 1.14, and Figure 1.15. InAs/Ga(In)Sb T2SL (black) is the T2SL material system that has been most investigated, particularly in the early days of T2SL development, owing to the fact that they have reasonably small lattice mismatch,

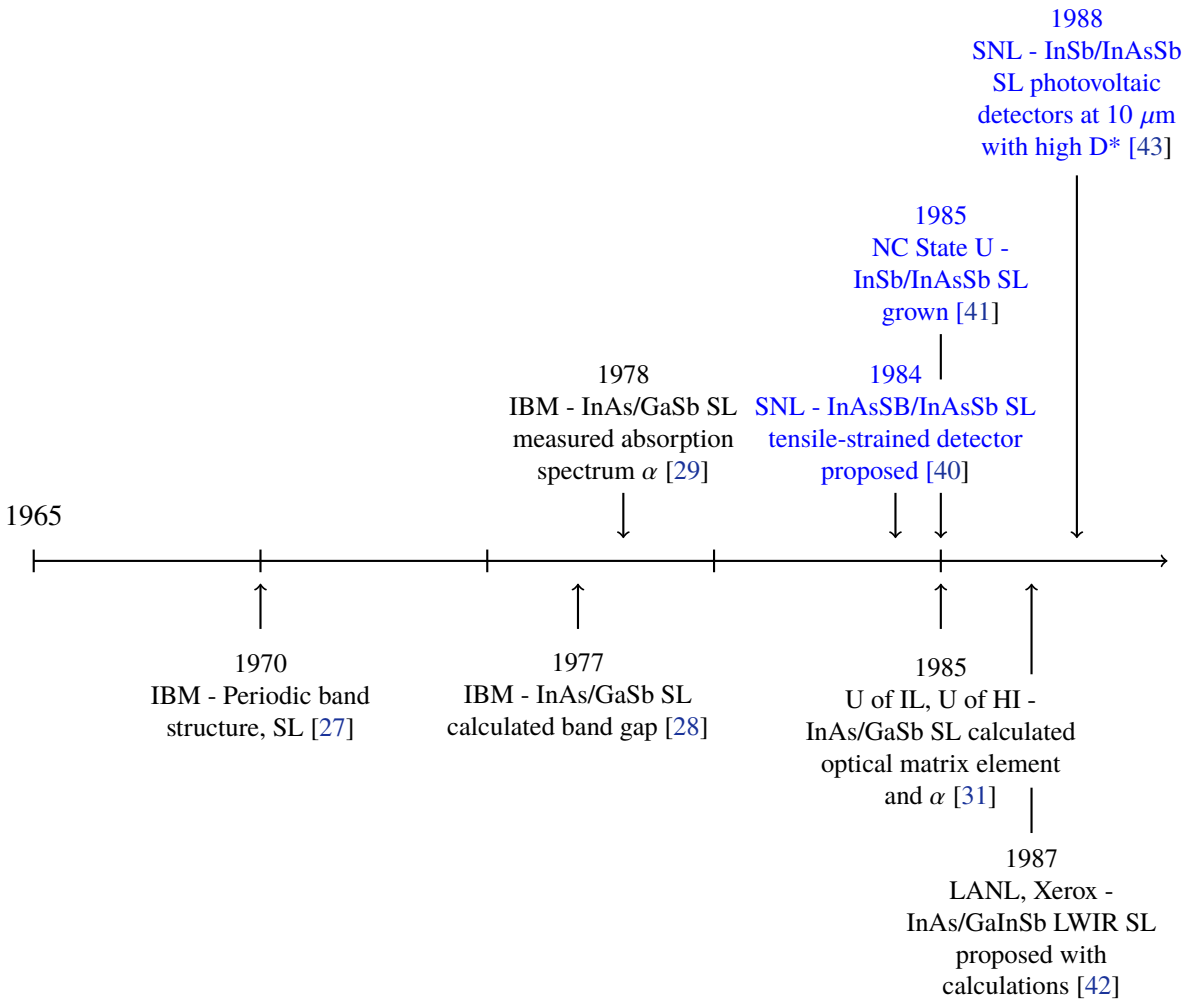

Figure 1.13: A timeline of T2SL history

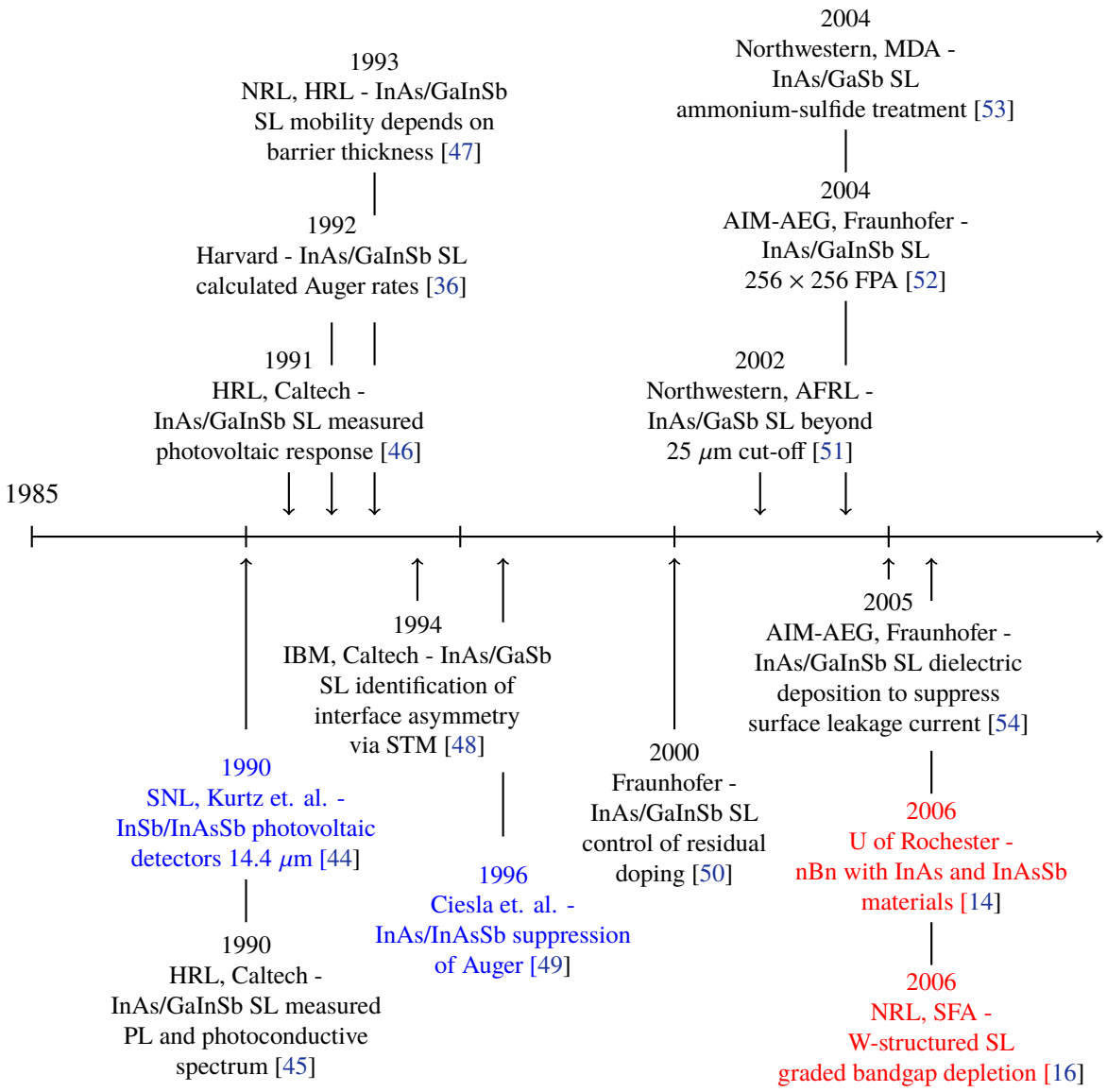

Figure 1.14: A timeline of T2SL history (continued)

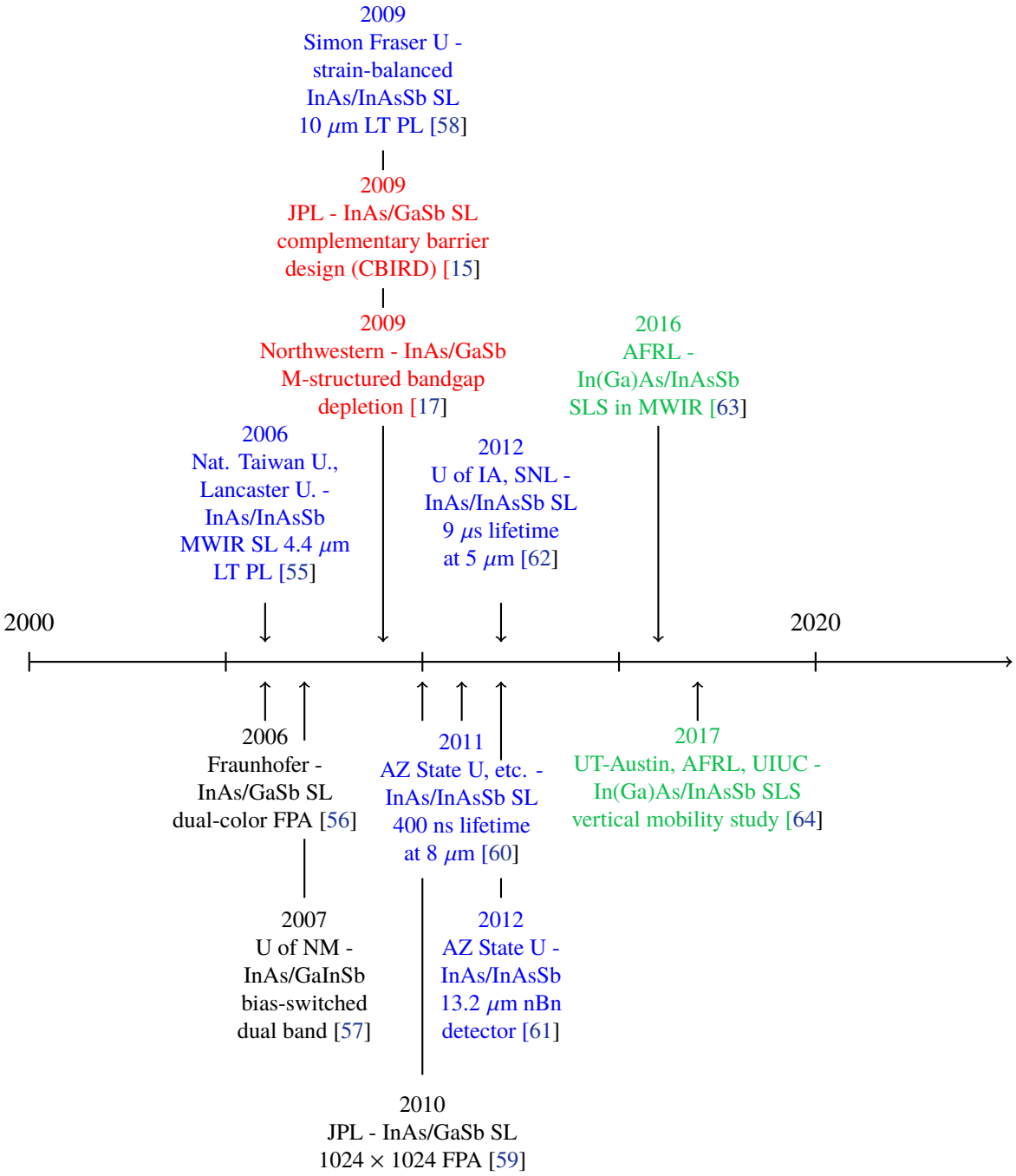

Figure 1.15: A timeline of T2SL history (continued)

while having a broken type-II band alignment. Another T2SL material system that has been actively studied is the InAs/InAsSb (blue) T2SL [40, 41, 43, 44, 49, 55, 58, 60, 61, 62]. These T2SLs are often referred to as Ga-free T2SLs, and are believed to offer significant improvement in IR detector quality the replacement of GaSb with InAsSb eliminates point defects associated with Ga in GaSb, which is one of the possible reasons for the degradation of diffusion length and minority carrier lifetime observed in InAs/GaSb T2SLs [65]. In this thesis, the recently proposed modified version of the Ga-free InAs/InAsSb material system, In(Ga)As/InAsSb (shown in green in Figure 1.15) strained-layer superlattices (SLSs), are comprehensively studied as a function of Ga content.

It is important to note that the T2SL materials not only offer a range of absorber designs, but can be integrated into a range of detector architectures as well (refer to Figure 1.13, Figure 1.14, and Figure 1.15). Photodiode architectures are well-established as the dominant photodetector device architecture in the visible and near-IR, and such an architecture can certainly be achieved using T2SL materials. Although both p-i-n and nBn structures (Chapter 1.2.3) can be employed for T2SL detectors, the nBn structures demonstrate several advantages over the p-i-n devices.

1.4.4 nBn structured T2SL photodetectors

The nBn detector was first demonstrated in 2006 by Maimon and Wicks, where they successfully showed the achievable dark current reduction of the nBn devices when compared to p-n photodiodes. In this work, bulk InAs or InAsSb material was used as an n-type absorber [14]. In a p-n junction, the SRH generation process can be very efficient in the depletion region, where the midgap traps are activated. Especially at low temperature (below 200 K), the SRH generation process is found to be the main source of the dark

current [14], and the SRH current density can be expressed as the following:

$$J_{\mathrm{SRH}} \approx q\frac{n_i}{\tau_{\mathrm{SRH}}}W_{\mathrm{dep}}, \tag{1.22}$$

where q is the charge of the electron, n_i is the intrinsic concentration of the semiconductor, τ_{SRH} is the SRH minority carrier lifetime, and W_{dep} is the depletion width of the p-n junction.

Unlike the p-n junction, the nBn device architecture utilizes a majority carrier blocking layer (refer to Figure 1.5) to inhibit SRH currents. This is because the field in the nBn largely drops over the barrier, and SRH generation must occur over the large bandgap of the barrier (which will result in a significant quenching of the SRH processes). Instead, the diffusion current (which depends on Auger generation) is the main dark current mechanism for the nBn device. The diffusion current density is:

$$J_{\mathrm{diff}} \approx q\frac{p_n}{\tau_{\mathrm{diff}}}L_h = q\frac{n_i^2}{N_D\tau_{\mathrm{diff}}}L_h, \tag{1.23}$$

where q is the charge of the electron, n_i is the intrinsic concentration of the semiconductor, τ_{diff} is the diffusion-based lifetime, N_D is the doping concentration of the n-type semiconductor, and L_h is the hole diffusion length. Since $J_{\mathrm{SRH}} \propto n_i \sim \exp(-E_g/2kT)$ and $J_{\mathrm{diff}} \propto n_i^2 \sim \exp(-E_g/kT)$, an nBn detector will operate with comparable dark current at a temperature twice that of a comparable pn junction device.

In summary, the main advantage of an nBn detector is the reduction in dark current, which results in less noise, and theoretically higher operating temperatures. By combining the nBn structured device and T2SL absorbing materials, the advantages associated with the nBn architecture (reduced SRH processes) and the T2SL (reduced Auger processes) offer the opportunity for photodetectors competitive with the current state of the art MCT system. In this thesis, the nBn structured T2SL infrared detectors are comprehensively studied using a variety of characterization techniques.

1.5 Outline of thesis

The presented research demonstrates an enhancement to the material characterization methodology, and proposes absorption-enhanced novel architectures, for infrared photodetectors. The main characterization technique discussed is electron beam induced current (EBIC), which is used to study the minority carrier diffusion length in photodetector devices. The modified EBIC modeling approach is introduced to more accurately analyze the experimental data, and a two-dimensional (2D) EBIC technique is also demonstrated in order to investigate both vertical and lateral diffusion lengths. Although the work presented is generally applicable to other semiconductor materials and devices, the main focus of this thesis is in the investigation of In(Ga)As/InAsSb strained-layer superlattices for IR photodetectors.

Chapter 2 describes several characterization techniques which are used in conjunction with the primary characterization technique covered in this thesis (EBIC). In Chapter 2, the following techniques will be discussed: Photoluminescence (PL), time-resolved photoluminescence (TRPL), absorption coefficient measurements, dark current measurements, and responsivity measurements.

Chapter 3 covers EBIC techniques. After discussing a brief history and the basic technical concept of EBIC, the state-of-the-art EBIC approach, including how to examine the data and how to model EBIC for parameter extractions, is explained in detail. Then, a modified EBIC technique is introduced to achieve more accurate parameter extraction.

Chapter 4 presents the experimental studies on the nBn structured In(Ga)As/InAsSb strained-layer superlattice (SLS) photodetectors as a function of Ga content. Following a discussion on the advantages of In(Ga)As/InAsSb SLSs, both previous and modified EBIC techniques are performed to demonstrate the importance of the new EBIC approach. With

the conjunction of time-resolved photoluminescence (TRPL), the minority carrier vertical mobility is determined to experimentally verify the proposed advantages.

Chapter 5 studies the dependence of carrier transport on the unit cell thickness of nBn structured InGaAs/InAsSb SLS devices. PL measurements are used to determine the effective bandgaps, and TRPL measurements provide the minority carrier lifetimes. Lastly, EBIC measurements are performed to extract the minority carrier vertical diffusion lengths.

Chapter 6 introduces a two-dimensional cross-sectional EBIC technique which allows us to understand both vertical and lateral minority carrier diffusion lengths in the same detector device. In order to simultaneously observe both vertical and lateral EBIC profiles, a new device architecture design is employed. After obtaining experimental cross-sectional 2D EBIC data on InGaAs/InAsSb SLS devices, a careful 2D EBIC modeling is performed to extract both vertical and lateral minority carrier diffusion lengths.

Chapter 7 proposes novel architectures for enhanced absorption infrared photodetectors utilizing highly doped semiconductor materials as a ground plane of the optical cavity. Finally, Chapter 8 summarizes the work presented in this thesis and discusses potential future work enabled by the results presented in this thesis.

Chapter 2

Characterization Techniques

In this thesis, various techniques are utilized to comprehensively characterize the optical and electrical properties of quantum engineered strained-layer superlattice (SLS) material systems. The bulk of this thesis focuses on the electron beam induced current (EBIC) technique, which will be extensively discussed in Chapter 3. This chapter is dedicated to describing the other techniques utilized to provide a full picture of SL behavior and to supplement the EBIC measurements that are at the center of this thesis.

2.1 Photoluminescence Spectroscopy

Photoluminescence (PL) spectroscopy is one of the core characterization techniques for understanding the optical properties of optoelectronic materials. In a semiconductor material, incident light of energy above the semiconductor band gap is absorbed by a valence band electron which is excited to the conduction band, leaving behind an empty energy state, which are typically referred to as "holes". Thus, because an absorbed photon creates a valence band hole and a conduction band electron, this process, photo-excitation, is said to generate electron hole pairs (EHPs). The optical generation of EHPs creates excess carrier concentrations in the semiconductor, now out of equilibrium. The system wants to return to its equilibrium state, which it does when the photo-excited electron falls back into the valence band, a process referred to as recombination. This recombination occurs by the emission of a photon (radiative recombination) though often times it occurs

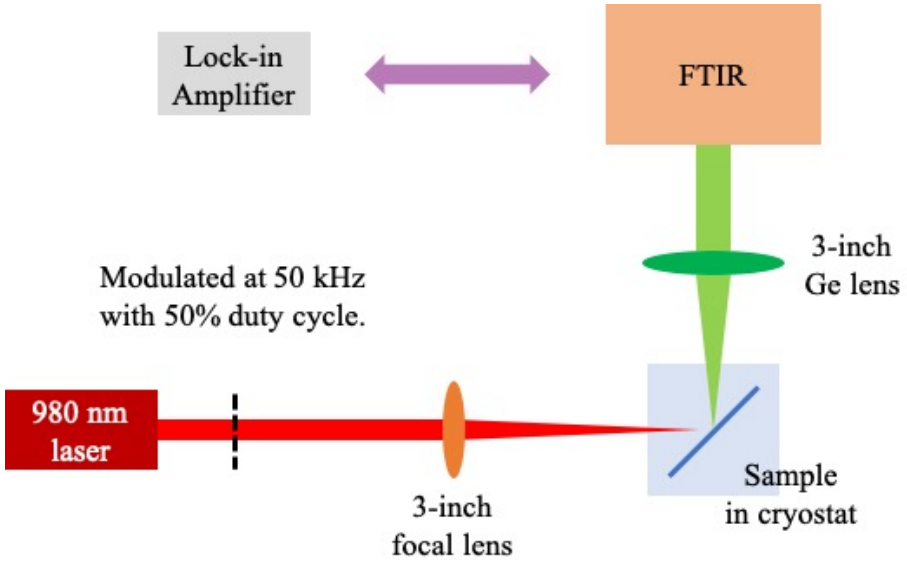

Figure 2.1: Schematic of the PL setup used to characterize the materials discussed in this thesis.

by giving its energy to other charge carriers or the lattice (non-radiative recombination). When the photo-excited carriers recombine radiatively, the emitted light is referred to as photoluminescence (PL). The measured PL signal as a function of wavelength often provides important information, such as the cut-off wavelength, λ_o, on the band structure and optical properties of a semiconductor material. The experimental set-up for a standard PL experiment is illustrated in Figure 2.1. The basic set-up requires a number of components: i) a proper light source providing photons with energies larger than the bandgap of the semiconductor material being interrogated, in order to excite EHPs, ii) optics to focus the excitation source onto the sample and to collect the light emitted from the sample, and iii) a spectrometer to measure the emitted light as a function of wavelength (or frequency). The PL experiments in this thesis all utilize a Fourier transform infrared (FTIR) spectrometer, which is the preferred spectroscopic tool for mid-infrared wavelengths.

The FTIR spectrometer is, in many ways, the single most important piece of equipment in a mid-IR PL experiment. The FTIR spectrometer is fundamentally based on the

Michelson interferometer, whose configuration is shown in Figure 2.2. The basic setup consists of a beam splitter, a stationary mirror, and a moving mirror. As shown in Figure 2.2, the beam splitter splits the incoming light. Half of the incoming light goes to a stationary mirror, while the other half is directed to a mirror whose translational position can be modulated. Both beams get reflected by the two different mirrors, and are then combined after going through the beam splitter again. For a given wavelength, the path difference between the two arms of the interferometer determine whether the light interferes constructively or destructively at the detector. As the moving mirror translates, the detector records an interferogram, which is nothing more than the intensity of detected light as a function of the mirror position. Taking a Fourier transform of the recorded interferogram provides a plot of light intensity as a function of wavelength, or in other words, a spectrum.

At shorter wavelengths, such as the near-IR, and for strongly emitting samples, the moving mirror can scan rapidly many times per second (so called rapid scan mode) providing numerous interferograms which are then averaged and Fourier transformed to provide a spectrum. However, for weak signals in the mid-IR the background thermal emission from the FTIR, optics, and the surrounding laboratory environment can be as large as the signal to be measured. This makes extracting the signal of interest from the background quite challenging. To overcome this background thermal signal, our PL measurements are typically taken using amplitude modulation step scan. In this approach, the emission from the source is modulated, and the FTIR detector records the modulated signal at a given fixed mirror position. The modulated detector signal is then taken to a lock-in amplifier, which demodulates the signal and thus filters the DC component (the thermal background) collected by the detector. The demodulated signal (now a DC signal) is recorded by the FTIR for the given mirror position, and then the FTIR's moving mirror steps in position and, following a delay to allow the detector signal to stabilize, the process

is performed again. In this manner, step-scan amplitude modulation PL spectroscopy is able to measure extremely weak signals from a device or material without being overwhelmed by the thermal background.

In our PL setup (Figure 2.1), the emitted light from a sample is used as a source. The sample is mounted in a liquid nitrogen cooled cryostat to perform the temperature dependent PL measurement. First, a 980 nm laser is modulated at 50 kHz with 50% duty cycle, then this modulated light is focused into the sample to excite carriers, which recombine and emit the photoluminescence signal to be detected. This emitted light is collimated by a Ge lens (focal length of 3 inches and diameter of 2 inches) and is directed to the optical port of the FTIR. The signal detected by the internal FTIR detector (in our case, a MCT detector) is sent to the lock-in amplifier, which is synched to the initial modulation of the laser. At the fixed mirror position, the lock-in amplifier returns the DC signal back to the FTIR. This procedure repeats as the mirror steps to the next position, then it slowly builds the interferogram with each step. By taking the Fourier transform of the intergerogram, the photoluminescence (PL) as a function of the wavelength can finally be obtained.

2.2 Time-Resolved Photoluminescence

Time-resolved photoluminescence (TRPL) is a contactless measurement of the excess minority carrier lifetime in a light-emitting material. A pumping laser with short time duration generates electron-hole pairs in the material under test. These EHPs recombine at a rate determined by the excess carrier concentration and the relative strength of the radiative and non-radiative recombination processes in the material. The resulting decaying photoluminescence is recorded as a function of time. Note that in this experimental set-up, we do not obtain any spectral information regarding the material emission, though optical filters can be used to probe certain spectral ranges as long as the emission intensity in the

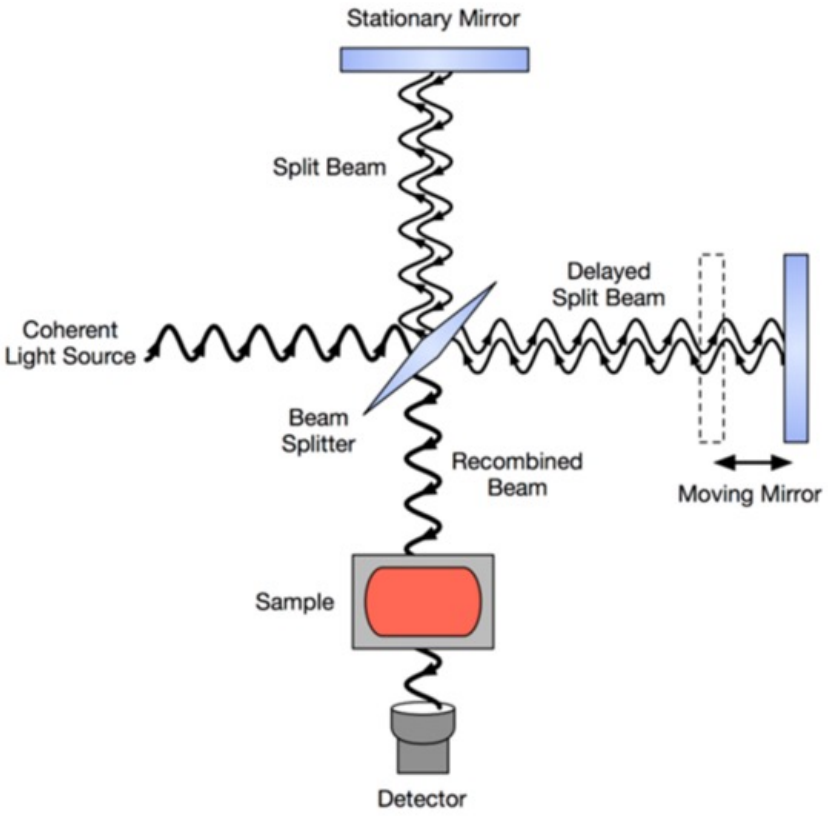

Figure 2.2: Schematic of a typical Michelson interferometer [6]. This figure shows the Michelson interferometer as it would be used to measure transmission through the sample in front of the detector.

transmitted spectral range is large enough to provide good signal to noise. With a proper fitting, a transient photoluminescence signal can be used to extract the minority carrier lifetime of the material under test. The configuration of the TRPL experimental setup is shown in Figure 2.3. In our experimental setup, a 1 ns pulsed laser operating at λ_o = 1064 nm is used to excite carriers in the material under test, and the emitted light from the sample is collected via a parabolic mirror. After going through the Ge focusing lens, the light travels through the low pass filter to block the scattered laser light and is then collected by the MCT detector. The emitted light is typically filtered with a longpass filter (in our case, a 3.6μm long pass filter) in order to remove scattered laser light and any light emission from the material substrate). The signal from the MCT pre-amp is now fed into the oscilloscope to obtain the time-resolved photoluminescence (TRPL) data. By mounting samples in a liquid nitrogen cooled cryostat, the temperature-dependent TRPL measurements can be obtained. In Chapter 4.2, the TRPL measurement is used to extract the minority carrier lifetime of SLS materials. The method used for parameter extraction from the TRPL data is discussed in 4.2 as well.

2.3 Dark Current

Dark current, as the name suggests, is the current as a function of applied bias for a device without any optical illumination. Since the detector noise is directly related to the detector dark current, the dark current provides an important measure of photodetector device performance. In this thesis, the dark current measurements are performed as a function of temperature using an Advanced Research Systems Closed-Cycle Cryogenic Probe Station [66]. This system provides a high vacuum and a close-cycle cooling process to achieve cryogenic environments as low as T = 10K. The temperature of our system is controlled by a Lakeshore Temperature Controller, which is coupled to the probe station. Once the

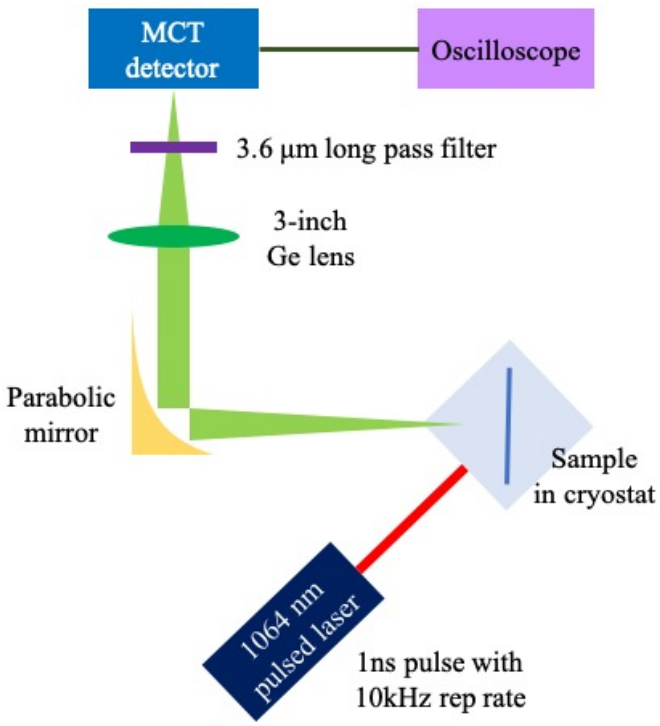

Figure 2.3: Schematic of the TRPL setup used to characterize the samples investigated in this thesis.

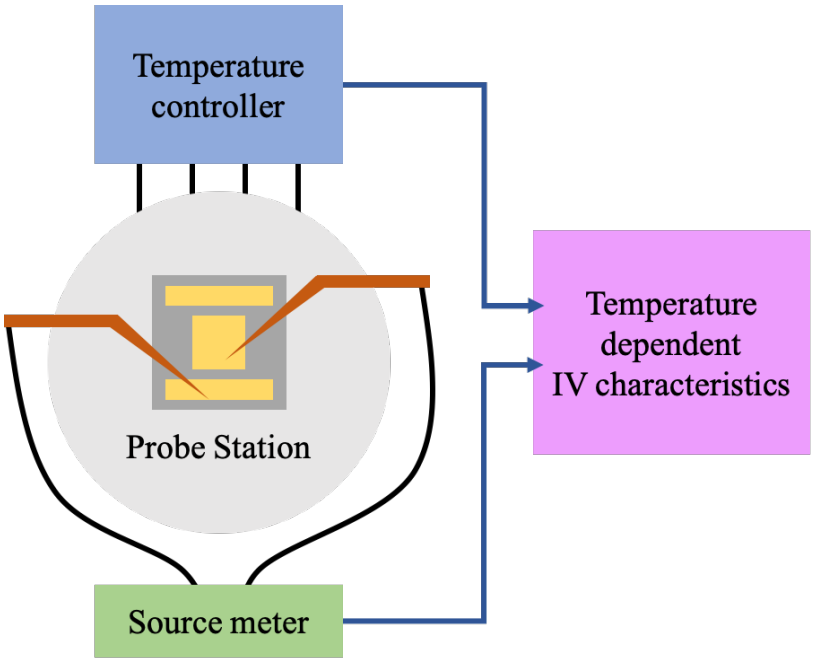

Figure 2.4: Schematic of the dark current measurement setup used to characterize the devices investigated in this thesis.

sample is placed in the probe station, the top and bottom contacts of the photodetectors are probed to attain IV characteristics using a Keithley 2460 Interactive SourceMeter. Figure 2.4 shows a schematic of the temperature dependent dark current measurement setup.

2.4 Absorption Coefficient

The absorption coefficient is one of the single most important optical properties determining the potential quality of a photodetector material. In this thesis, we measure the absorption coefficient of our materials by measuring the transmission spectra of two samples of the same material, but with different thicknesses. In most cases, we begin with an as-grown T2SL sample and then etch some depth into half of the sample leaving the remainder of the sample unetched. Measuring transmission through the etched and unetched portion of the sample offers the transmission spectra through absorbers of differing

thickness. Absorption coefficient measurements are performed using a Bruker Vertex70 FTIR spectrometer in an experimental setup shown schematically in Figure 2.5. In this set-up,light from the broadband infrared light source (globar) in the FTIR passes through the FTIR's interferometer, and exits the FTIR in a collimated beam, at which point it is focused onto the sample. The light transmitted through the sample is then collimated and focused onto an external MCT detector. The MCT detector output is measured as a function of the mirror position of the FTIR, providing the interferogram which is then Fourier transformed to give the transmitted spectrum. Using the measured transmission spectra for the etched and unetched portions of the sample, the absorption coefficient of the material can be extracted based on Equation 2.1:

$$T_{etched}(\lambda) - T_{unetched}(\lambda) = e^{-\alpha(\lambda)t}, \tag{2.1}$$

where $T_{etched}(\lambda)$ is the transmission of the etched material, $T_{unetched}(\lambda)$ is the transmission of the unetched material, $\alpha(\lambda)$ is the absorption coefficient, and t is the thickness of the material that has been etched.

It should be noted that the above approach provides accurate absorption coefficients for materials only when minimal internal reflection between material layers occurs, in other words when a single-pass assumption for the incident light is valid. For materials with significant variation in refractive index, internal reflections can set up interference within the sample, which can vary depending on the sample thickness, and can thus result in inaccurate measurement of the material absorption coefficient, $\alpha(\lambda)$.

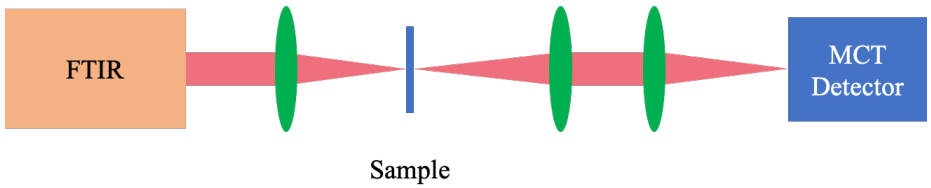

Figure 2.5: Schematic of the transmission measurement setup used to determine the absorption coefficients of the samples studied in this work.

2.5 External Quantum Efficiency

One of the standard measures of detector performance, External Quantum Efficiency (EQE), can be measured as the percentage of the incident photons converted to an electric signal. The EQE measurements reported in this thesis are performed by our collaborators at the Air Force Research Laboratory at Wright-Patterson. To perform the temperature dependent EQE measurement, the samples are mounted in the pour-fill dewar. The spectral photoresponse of the photodetectors was measured with a FTIR spectrometer by using a calibrated blackbody with spectral filters, while the samples are under the operating conditions.

Later in this thesis, the minority carrier diffusion lengths extracted from electron beam induced current (EBIC) technique (detailed in Chapter 3) are compared to those extracted from EQE measurements. Since the EQE is primarily determined by the absorption coefficient of the semiconductor material and the minority carrier diffusion length, the minority carrier diffusion length can be extracted by combining both EQE and absorption coefficient measurements. In a p-n photodiode, external quantum efficiency, η, consists of three following factors: $\eta = \eta_p + \eta_{dep} + \eta_n$ [20]. The quantum efficiency in the p-type semiconductor, η_p, the QE in the depletion region, η_{dep}, and the QE in the n-type semiconductor, η_n, can be expressed as the followings:

$$\eta_p = (1-R)\frac{\alpha L_h}{(\alpha L_h)^2 - 1}\left(\frac{\alpha L_h - e^{-\alpha x_n} sinh(x_n/L_h)}{cosh(x_n/L_n)} - \alpha L_h e^{-\alpha x_n}\right), \tag{2.2}$$

$$\eta_{dep} = (1-R)e^{\alpha x_n}(1 - e^{-\alpha x_{dep}}), \tag{2.3}$$

$$\eta_n = (1-R)\frac{\alpha L_e}{(\alpha L_e)^2 - 1}e^{-\alpha(x_n + x_{dep})}\left(\frac{-\alpha L_e e^{-\alpha x_p} - sinh(x_p/L_e)}{cosh(x_p/L_e)} + \alpha L_e\right), \tag{2.4}$$

where R is the reflectivity, α is the absorption coefficient, L_h (L_e) is the hole (electron) diffusion length, x_n (x_p) is the penetration of the transition region into the n-type (p-type) material, and x_{dep} is the width of the depletion region.

In Chapter 4 and 5, the EQE of fully reticulated single element detectors at different temperatures was measured [1] following a standard radiometric characterization technique described in Ref. [67]. The variation of the theoretically expected quantum efficiency with the diffusion length (L_h) for the same set of detectors was analytically calculated as described in Ref. [68], using the experimentally determined absorption coefficient from the detector materials, measured using the technique described in Refs. [69, 70]. The diffusion length values at different temperatures were then extracted by fitting the experimental EQE data points at corresponding temperatures [68].

Chapter 3

Electron Beam Induced Current

[1]Electron beam induced current (EBIC) measurements have been used extensively to characterize the carrier dynamics of semiconductor materials and devices [71, 72, 73, 74, 75, 76, 77, 78]. In the EBIC technique, a beam of high energy electrons (typically in a scanning electron microscope, or SEM) is directed at the surface (or exposed cross-section) of a semiconductor device. Figure 3.1 illustrates two different EBIC setups: one showing the set-up for (a) a plan view EBIC and the other for a (b) cross-sectional EBIC measurement.

A plan view EBIC scan uses a configuration where the high energy electron beam is impinging at the top surface of the device, while a cross-sectional EBIC has the electron beam scanning the cross-sectional area of the junction. Plan view EBIC measurements are mostly used to study grain boundaries or dislocations in semiconductor materials [79, 80], and cross-sectional view EBIC measurements are performed to understand the diffusion lengths and the surface recombination velocity [77, 78, 81, 82] in semiconductor devices. This chapter will focus on cross-sectional EBIC technique to investigate the vertical carrier transport of the infrared detector materials.

Fundamentally, electron beam induced current (EBIC) measures the amplified cur-

[1]This work has been published as "Modified electron beam induced current technique for In(Ga)As/InAsSb superlattice infrared detectors" in J. Appl. Phys., vol. 122, no. 7, p. 074053, 2017. The first author, N. Yoon, has contributed to the majority of the work except the SLS material growth and EQE measurements, which have been performed by the authors at AFRL.

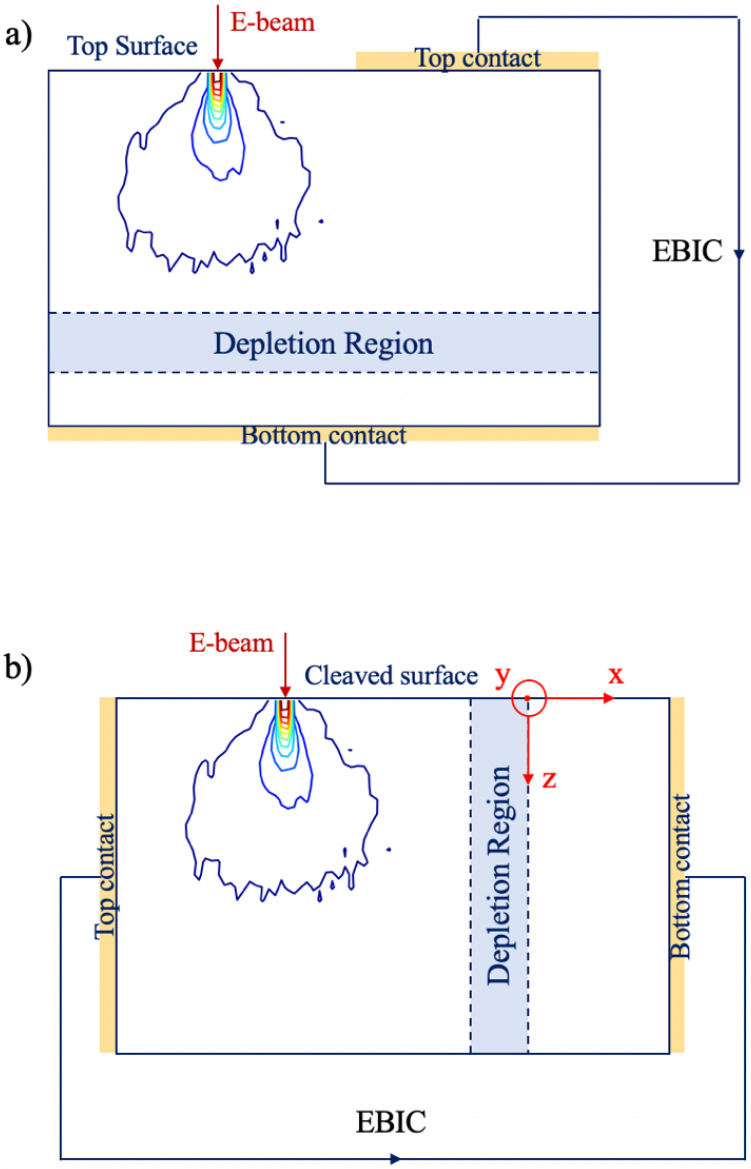

Figure 3.1: The schematics of the two most commonly used EBIC measurement setups. (a) Plan view EBIC uses a planar-collector geometry, since the electron beam is scanning across the sample top surface, in a plane parallel to the depletion region. (b) Cross-sectional EBIC uses a normal-collector geometry, where the electron beam is scanned in a plane orthogonal to the depletion region.

rent signal due to the collection of excess charge carriers generated by a high electron beam in a scanning electron microscope (SEM). In a representative experiment, the high energy electron beam, at some position on a semiconductor device, generates an excess carrier distribution dependent on the beam energy. The excess carriers can either i) recombine in the material bulk or at the material surface, or alternatively, ii) can be collected as a current by the electrical contacts to the device under test. The current collected depends on the transport properties of the material and the device under test, as well as the location of the electron beam on the device surface and the energy of the beam (which determines the distribution of excess carriers in the device). By scanning the beam, and collecting a current at every beam position, one maps out a current image of the device, which provides a qualitative picture of excess carrier transport.

3.1 Cross-sectional EBIC

The cross-sectional geometry gives EBIC profiles as an electron beam scans in the direction normal to the collector, as illustrated in Figure 3.1 b). The high energy electrons generate electron hole pairs (EHPs) which can then be collected at the device contacts, and the current generated by the electron beam is measured as a function of beam position. The EBIC measurement thus generates a "current image" of the device, as opposed to the secondary electron emission image typically obtained in an SEM. Figure 3.2 shows a cross-sectional SEM image of a fabricated reverse biased pn junction device along with its EBIC image where the signal is maximized in the depletion region.

In principle, the extremely small electron beam spot size offers the potential for spatially-resolved information on fundamental material parameters in active devices. This technique has been applied over the past few decades to characterize electronic and opto-electronic devices, providing valuable information on the electronic properties of the device

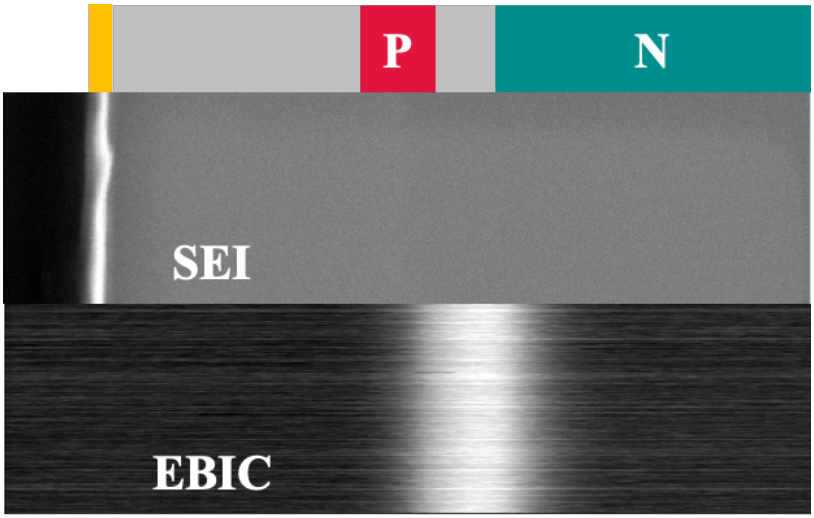

Figure 3.2: The illustration of a simple p-i-n junction along with a SEM image and an EBIC image taken of the same p-i-n junction device. The metal layer is the brightest region in the SEM image, while the depletion region shows the greatest EBIC signal [7].

material [76, 78]. In comparison to the closely related XBIC [83] and LBIC [84] measurements (x-ray- and laser- beam induced current, respectively), EBIC offers more accurate material parameter extraction for materials with short diffusion lengths [85] as well as straightforward integration with scanning electron microscopes. Material parameters are most typically extracted by fitting the experimentally obtained EBIC data to a model, so that it is very important to accurately model the experimental outputs of the EBIC measurement.

3.2 Theory of EBIC

The power of the EBIC technique is somewhat offset by the significant modeling required to extract meaningful values from the experimental data. It is very critical to understand the EBIC theory and to accurately model the EBIC signal, since the parameter extraction is done by fitting the experimental data to the model. The amount of current induced by the electron beam bombardment can be expressed as a product of the carrier

generation volume, $h(x, y, z)$, and the probability of collection, $\phi(x, y, z)$. The carrier generation volume is the spatial carrier distribution generated by the electron beam relative to its impinging point. The probability of collection represents the chance for a generated carrier at a given position to contribute to the EBIC current by reaching a collecting boundary after the diffusion process. These two volumetric functions are multiplied and convoluted, resulting in an expression for the EBIC profile as a function of the electron beam position:

$$\eta(x) = \iiint h(x - x_o, y, z)\phi(x, y, z)dxdydz, \tag{3.1}$$

where x is the position along the growth direction, y is the position along the growth plane, and z is the depth from the cleaved surface.

The EBIC signal, for a given electron beam position on the cleaved surface, is proportional to the minority carrier collection efficiency of the device junction. In the idealized picture of EBIC, an extremely narrow electron beam acts as a point source generator of electron hole pairs (EHPs), and thus for each beam position one can assume a singular collection efficiency.

In reality, the small spot size, high energy beam of electrons scatters upon reaching the material surface, and thus results in an EHP generation volume extending both laterally from the beam position (x, along the growth direction and y, along the growth plane) and into the sample (z, depth from cleaved surface). Figure 3.3 shows the orientation of the electron beam on the cross-sectional facet of an SLS infrared detector.

3.3 State-of-the-art EBIC

Before describing our new modified EBIC approach, the previous state-of-the-art EBIC technique is discussed to show how the EBIC profile has traditionally been analytically

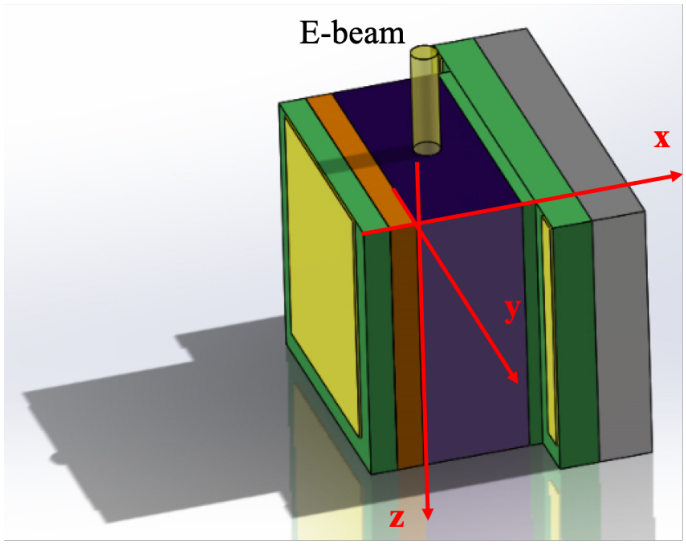

Figure 3.3: The electron beam of SEM is impinging at the cleaved surface of the device under test. The directions are defined to help EBIC modeling - x is the growth direction, y is the growth plane direction, and z is the depth from cleaved surface.

modeled and how the experimental EBIC data is typically processed to fit the analytical model.

3.3.1 Analytical modeling

The previous state-of-the-art analytical EBIC modeling approach can be described as progressing in three steps: i) modelling carrier generation, ii) modelling probability of collection, and iii) calculating collection efficiency.

Carrier generation

The carrier generation volume, $h(x, y, z)$, depends on both the composition of the sample under study and the electron beam energy that impinges upon the sample. The distribution of excited carriers is usually based on either empirical formulae [78] or statistical methods, specifically the Monte Carlo method [86]. The most commonly used empirical expression for the carrier generation volume, $h(x, y, z)$, was proposed by Bonard and Ganière

for a two-dimensional system [78]:

$$h(x,z) = \frac{1}{H}\exp\Big(-\frac{x^2}{\sigma_1^2}\Big)z^2\exp\Big(-\frac{z}{\sigma_2}\Big). \tag{3.2}$$

where H is a normalizing factor, expressed as a function of σ_1 and σ_2: $H = 2\sqrt{\pi}\sigma_1\sigma_2^3$, where σ_1 represents the spread of excited carriers in x, and σ_2 represents the spread of excited carriers in the z direction. The most beneficial thing about utilizing this empirical expression is that it gives an analytical solution to the total EBIC current, which is further discussed in the following subsection

In Bonard and Ganière's paper, $\sigma_1 = \sqrt{0.05 + 0.0001E_b^{2.78}}$ and $\sigma_2 = 0.02 + 0.003E_b^{1.5}$ for InP or $Al_{0.4}Ga_{0.6}As$, since both materials have comparable densities and atomic numbers [78]. For other material systems, the expressions for σ_1 and σ_2 could be adjusted to account for differences in atomic mass or density, though the basic generation volume shape would be similar.

With the significant improvement in computational power over decades since the work of Bonard and Ganière, recent, the state-of-the-art EBIC studies tend to use the statistical Monte Carlo method to calculate the high energy electron trajectories as they scatter in the material under test [81, 82]. This approach permits the study other materials, such as the superlattice materials upon which this thesis is primarily focused on characterizing, because the Monte Carlo approach requires only the material properties as inputs and then is able to generate a carrier generation profile for any material system or alloy. By fitting this result of the Monte Carlo simulation to Equation 3.2, both σ_1 and σ_2 values can be extracted to provide an analytical expression for the carrier generation volume. This approach still enables the EBIC modeling to be almost completely analytical (with the obvious exception of the Monte Carlo model).

Probability of collection

Once the carriers are generated by the electron beam bombardment, only some portion of those carriers contribute to current. In the low-injection regime, one can assume that the carrier contribution to the current is mainly via the diffusion process. Therefore, the probability of a carrier reaching the collecting junction can be derived from the diffusion equation. Donolato [77] provides a detailed derivation which concludes that the probability of collection, $\phi(x, y, z)$, can be expressed as the following differential equation:

$$\nabla^2\phi(x, y, z) - \frac{\phi(x, y, z)}{L^2} = 0, \tag{3.3}$$

where L is the diffusion length of the material. When the lateral dimension is considered to be infinite, the expression above collapses to the two-dimensional case and results in the following boundary conditions:

$$\left.\frac{\delta\phi}{\delta x}\right|_{x=0} = s\phi(0, z) - s, \tag{3.4}$$

$$\left.\frac{\delta\phi}{\delta z}\right|_{z=0} = s_0\phi(x, 0), \tag{3.5}$$

$$\phi|_{x=\infty} = 0, \tag{3.6}$$

$$\left.\frac{\delta\phi}{\delta z}\right|_{z=\infty} = 0, \tag{3.7}$$

where s is the junction edge recombination velocity, and s_0 is the surface recombination velocity. For the case of an ideal sample with a perfect collection interface (in other words, where every carrier which diffuses to the interface contributes to the current), s approaches infinity. The final solution is shown below, and its further derivation can be found in Ref. [78].

$$\phi(x, z) = \frac{2}{\pi}\frac{s_0}{D}\int_0^\infty \frac{\exp[-\mu(x)]}{k^2 + (s_0/D)^2}\left[\cos(kz) + \frac{s_0}{Dk}\sin(kz)\right]dk, \tag{3.8}$$

where $\mu(k) = \sqrt{k^2 + 1/L^2}$, k is the Eigen function solution to the transcendental equation

[77], and D is the diffusivity. In Chapter 3.4, the probability of collection, $\phi(x, z)$ is modified to a piece-wise function for the nBn structured devices.

Collection efficiency

As briefly discussed in Chapter 3.2, the EBIC current can be expressed as the convolution integral of the carrier generation distribution and the probability of collection, shown in Equation 3.1. By combining Equations 3.1, 3.2, and 3.8, the final analytical solution of the collection efficiency is shown as the following [78]:

$$\begin{aligned}\eta(x) =& \frac{1}{\pi}\int_0^{\infty}\left[\frac{S_h}{D_h}\vartheta_h(k,x) + \frac{S_e}{D_e}\vartheta_e(k,-(x+d_j))\right]dk \\ &+ 0.5\left[\mathrm{erf}\left(\frac{x+d_j}{\sigma_1}\right) - \mathrm{erf}\left(\frac{x}{\sigma_1}\right)\right],\end{aligned} \tag{3.9}$$

where

$$\begin{aligned}\vartheta_{h,e}(k,x) =& \frac{1}{k^2 + (S_{h,e}/D_{h,e})^2}\mathrm{erfc}\left[\frac{\sigma_1}{2}\left(\mu(k,L_{h,e}) - \frac{2x}{\sigma_1^2}\right)\right] \\ &\times \exp\left[\frac{\sigma_1\mu(k,L_{h,e})}{2}\right]^2 \\ &\times \exp[-\mu(k,L_{h,e})x]\frac{1}{(1+k^2\sigma_2^2)^3} \\ &\times \left[1 + 3\frac{S_{h,e}\sigma_2}{D_{h,e}} - k^2\left(\frac{S_{h,e}\sigma_2^3}{D_{h,e}} + 3\sigma_2^2\right)\right].\end{aligned} \tag{3.10}$$

This analytical solution is used for EBIC modeling, thus the EBIC profile is a function of diffusion length, L, and the surface recombination to diffusivity ratio, S/D, where the subscripts h or e indicates the expression for holes or electrons, respectively.

3.3.2 Normalized experimental data

With this analytical approach, the collection efficiency, $\eta(x)$, is normalized to 1 and is independent of the electron beam energy. Therefore, the experimental data should

all be normalized regardless of the electron beam energy values. In recent EBIC literature [81, 82], both the experimental EBIC data and the modeled EBIC are normalized to study the diffusion characteristics. In the following chapter, the modified numerical EBIC modeling approach is proposed along with the direct comparison to the previous state-of-the-art analytical EBIC, and I discuss the limitations associated with the normalization of the experimental and modeled EBIC profiles.

3.4 Modified EBIC

With the rapid recent increase in computational speed and power, an analytical approach to EBIC modeling may no longer be the only suitable technique for parameter extraction. To demonstrate this, we developed a technique for our EBIC modeling which leverages a numerical approach to solve Equation 3.2. In this chapter, the modified numerical EBIC modeling approach is proposed, along with the comparison to the previous state-of-the-art analytical EBIC approach.

3.4.1 Numerical modeling

The modified numerical EBIC modeling technique can be explained in three parts: i) carrier generation, ii) probability of collection, and iii) collection efficiency.

Carrier generation

In previous approaches to EBIC modeling, the normalized 2D carrier generation function $h_{E_b}(x - x_o, z)$, is analytically expressed as shown in Equation 3.11 (Ref. [78]):

$$h_{E_b}(x, z) = \frac{1}{H}\exp\Big(-\frac{x^2}{\sigma_1^2}\Big)z^2\exp\Big(-\frac{z}{\sigma_2}\Big), \tag{3.11}$$

where H is the normalization factor, σ_1 represents the spread of the generation profile in the x direction, and σ_2 is the spread of the profile in the z direction (both of which have

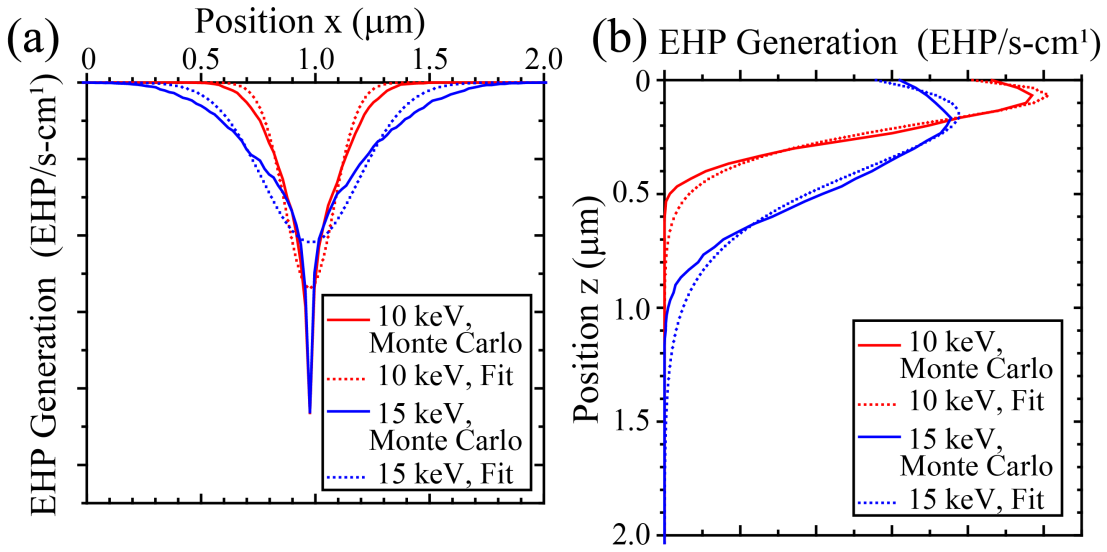

Figure 3.4: The Monte Carlo simulation (solid) of, and analytical fit (dashed) to, the excited carrier generation distribution created by the electron beam (10 keV-red and 15 keV-blue) of a scanning electron microscope (SEM) plotted as a function of the position in the (a) x-direction, integrated in y and z and (b) z-direction, integrated over x and y.

an empirical dependence on beam energy). Equation 3.11 is used to fit the normalized Monte-Carlo simulated generation distribution, with the fitting performed in the x and z directions separately.

Figures 3.4 (a) and 3.4 (b) show the Monte Carlo simulated EHP generation profiles in the x and z directions, respectively, for incident electron beam energies of 10 and 15 keV, for the electron beam impinging at $x_o = 1\mu$m (with $x = 0$ again being the barrier/absorber interface). The analytical fitting functions ($h_{E_b}(x-x_o, z)$) for each beam energy are plotted as dashed lines in Figures 3.4 (a) and 3.4 (b). Comparison between the numerically simulated generation distribution and the analytical fitting functions shows good agreement in the z direction, into the sample. However, the analytical expression for the x-dependence (along the growth direction) of the generation profile does not accurately capture the strength of EHP generation near the position of the incident electron beam (x_o). To quantify this,

we compare the percentage of EHPs generated within the range $x_o \pm 40$ nm for both the analytical and numerical generation distributions as a function of beam energy. At low beam energies (10 keV), the two approaches are similar (62% vs. 61%), but as beam energy increases, the analytical approach diverges from our numerical results: 37% vs. 30%, 27% vs. 19%, 21% vs. 13%, and 17% vs. 10% (numerical vs. analytical) for 15, 20, 25, and 30 keV beam energies, respectively. In addition, the normalization of the beam profiles removes the ability to model the relative amplitude of the EBIC signal as a function of beam energy and current.

As described in 3.16 above, the integral of the product of the 2D EHP generation function, $h_{E_b}(x - x_o, z)$, and the probability of collection, $\phi(x, z)$, over the x-z plane, returns the efficiency of collection, $\eta(x_o)$. The use of the analytical expression for the EHP generation function given in Equation 3.11 and the probability of collection expressions derived from the diffusion equation shown in Equations 3.12 - 3.15 allow for an analytical expression to be derived for the collection efficiency, $\eta_{E_b}(x_o)$, significantly simplifying the EBIC modeling process. However, because both the EHP generation function and the probability of collection are typically normalized, the resulting $\eta_{E_b}(x_o)$ does not reflect the relative changes in $\eta_{E_b}(x_o)$ with changing beam energy and current. In addition, as mentioned earlier, while the analytical expressions for the generation distribution allow for a final analytical expression for $\eta_{E_b}(x_o)$, they do not offer an entirely accurate picture of the actual EHP generation distribution, especially in the lateral (x and y) directions. This can lead to weaker fits to the data, and thus slightly more uncertainty in the extracted values for L_h and S_h/D_h.

Probability of collection

We define the probability of collection, $\phi(x, y, z)$, as the probability that a hole gen-

erated at point (x, z) will diffuse to the detector junction and be collected as a photocurrent. The collection probability for EHPs generated at different x positions (for the same position of the electron beam, x_o) will vary, depending on their relative proximity to the junction. The EHPs' probability of collection will also vary as a function of depth into the sample (z), due to surface recombination effects. Finally, $\phi(x, y, z)$ can also depend on y, for EBIC measurements close to detector mesa sidewalls, on samples with metal aperture contacts, or for samples with inhomogeneous defect densities (on a length scale on the order of the width of the carrier generation volume).

The diffusion equation, describing the transport of beam-generated minority carriers, is used to determine the probability of collection, $\phi(x, z)$ [78]. Originally, this expression was derived for EBIC modeling of bulk p-n junction diode devices [75] and later also used to model SLS p-n junction detectors [78]. The probability of collection expression for SLS nBn detectors must be adjusted somewhat, and is given below in Equations 3.12 - 3.15:

For $-0.4 < x < -0.2\mu$m (top contact),

$$\phi(x, z) = \frac{2S_h}{\pi D_h} \int_0^\infty e^{x\sqrt{k^2+(\frac{1}{L_h})^2}} \frac{cos(kz) + \frac{1}{k}\frac{S_h}{D_h} sin(kz)}{k^2 + (\frac{S_h}{D_h})^2} dk. \tag{3.12}$$

For $-0.2 < x < 0\mu$m (barrier),

$$\phi(x, z) = 1. \tag{3.13}$$

For $0 < x < 2\mu$m (absorber),

$$\phi(x, z) = \frac{2S_h}{\pi D_h} \int_0^\infty e^{-x\sqrt{k^2+(\frac{1}{L_h})^2}} \frac{cos(kz) + \frac{1}{k}\frac{S_h}{D_h} sin(kz)}{k^2 + (\frac{S_h}{D_h})^2} dk. \tag{3.14}$$

For $x > 2\mu$m (substrate),

$$\phi(x, z) = 0 \tag{3.15}$$

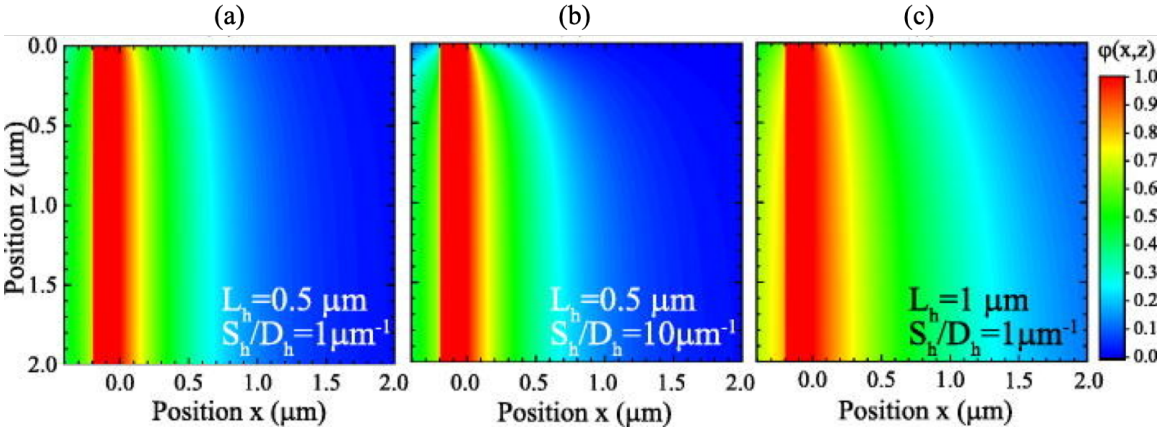

Figure 3.5: The calculated probability of collection for an nBn detector plotted for (a) $L_h = 0.5\mu m$ and $S_h/D_h = 1\mu m^{-1}$, (b) $L_h = 0.5\mu m$ and $S_h/D_h = 10\mu m^{-1}$, and (c) $L_h = 1\mu m$ and $S_h/D_h = 1\mu m^{-1}$, showing the effect of each variable on the probability of collection.

As can be seen in the above expressions, $\phi(x, z)$, once integrated over k, depends entirely on the minority (hole) carrier diffusion length, L_h, and the surface recombination velocity to diffusivity ratio, S_h/D_h. Here the k's denote discrete solutions to the transcendental equation governing the z-dependence of the probability of collection, which for thick materials ($z >> L$) becomes continuous, resulting in the integrals of Equations 3.12 - 3.15, as detailed in Ref. [78]. In Figures 3.5 (a)-(c), we show contour plots of the probability of collection in our SLS structures for various L_h and S_h/D_h combinations: $L_h = 0.5\mu m$ and $S_h/D_h = 1\mu m^{-1}$, $L_h = 0.5\mu m$ and $S_h/D_h = 10\mu m^{-1}$, and $L_h = 1\mu m$ and $S_h/D_h = 1\mu m^{-1}$, respectively. From these plots one can clearly see the effect of higher S_h/D_h values, significantly reducing the probability of collection at the cleaved surface ($z = 0\mu m$) as more of the generated EHPs recombine via surface states before they can be collected. As expected, increases in L_h broaden the probability of collection towards the substrate.

Collection efficiency

The efficiency of collection, $\eta(x_o)$, is effectively a measure of the EBIC current generated by the EHP generation distribution associated with a beam position x_o, and can

be calculated by taking the volume integral of the product of the probability of collection, $\phi(x, z)$, and the electron hole pair (EHP) generation function, $g_{E_b}(x - x_o, y, z)[\frac{EHP}{s-cm^3}]$, where the subscript E_b indicates the fact that our EHP distribution depends on the electron beam energy. The solid metal contact pads, the location of our EBIC measurement (far from the mesa sidewalls), and the fact that we see consistent EBIC signals across the lateral range (y-direction) of the sample cross-sections enable us to approximate the probability of collection in our measurement as having no y-dependence, such that we can integrate our three-dimensional (3D) generation function to give a two-dimensional (2D) generation function $h_{E_b}(x - x_o, z) = \int_{-\infty}^{\infty} g_{E_b}(x - x_o, y, z)dy$. For a sample using metal contacts with apertures for light transmission, or with defect spacing on the order of the width of the generation function, the full 3D generation function would need to be used, as we demonstrate in Chapter 6. At each beam position (x_o), we solve the integral

$$\eta_{E_b}(x_o) = \int_{-\infty}^{+\infty} dx \int_{0}^{\infty} h_{E_b}(x - x_o, z)\phi(x, z)dz, \tag{3.16}$$

where $x = 0$ denotes the position of the collection junction (at the barrier/absorber interface) and $z = 0$ the cleaved surface of the device. The 2D generation function, $h_{E_b}(x - x_o, z)$, is determined numerically using CASINO Monte Carlo software [86] simulations for each position (x_o) across the growth direction of the device, while the probability of collection, $\phi(x, z)$, can be derived from the diffusion equation [78].

The Monte Carlo simulations effectively return a volumetric distribution of EHP generation, $h_{E_b}(x_i - x_o, z_j)$, for some number of incident high energy electrons (N, typically in the 10's of thousands). Using the recorded beam current (I_{beam}, measured by a Faraday cup) for each beam energy, we can determine the EHP generation rate as a function of position, $G_{EHP}(x_i - x_o, z_j) = \frac{h_{E_b}(x_i - x_o, z_j)I_{beam}}{Ne}$ [EHPs/s], where e is the charge of an electron.

Using this Monte Carlo-simulated generation distribution, as opposed to the analytical fit of Equation 3.11, we can perform a numerical integration by dividing our device into discrete differential volumes and summing the current contributed to the total EBIC signal from each of these differential volumes [Equation 3.17], which we can use to determine the EBIC current ($i_{E_b}(x_o)$) and normalized EBIC current ($I_{E_b}(x_o)$) as a function of position [Equation 3.18]

$$\eta_{E_b}(x_o) = \sum_{i=-\infty}^{+\infty} \Delta\tilde{x}_i \sum_{j=0}^{+\infty} h_{E_b}(x_i - x_o, z_j)\phi(x_i, z_j)\Delta z_j \tag{3.17}$$

$$I_{10\text{keV}}(x_o) = \frac{\eta_{10\text{keV}}(x_o) I_{beam}(10\text{keV})}{NA_{mod}} = \frac{i_{10\text{keV}}(x_o)}{A_{mod}}, \text{where } I_{10\text{keV}}(x = 0) = 1. \tag{3.18}$$

The fitting process then begins by looking at the lowest energy electron beam data. For our initial fitting, we normalize both our modeled and experimental data such that $I_{10\text{keV}}(x = 0) = 1$, using scaling factors A_{mod} and A_{exp} (10 keV), respectively. We evaluate the numerical sum in Equation 3.17, and the scaling of Equation 3.18, for a range of L_h and S_h/D_h values, and then measure the fit error by summing the square of the deviation of our modeled current profile to the experimental current profile.

3.4.2 Relative experimental data

With this modified numerical solution for the collection efficiency, the modeled EBIC profiles are now normalized relative to the lowest beam energy EBIC data. Thus, in order to compare our modeled to experimental results, we must normalize our experimental EBIC profiles in a similar manner to the modeled results.

3.5 Comparison

Analytical integration of the product of the carrier generation profile and the carrier collection probability requires the use of analytical fits to the carrier generation profile, fits which do not accurately reflect the numerical simulations, resulting in a loss of spatial resolution for the modeled EBIC, and poorer fits to the experimental data. In addition, the most frequent examples of EBIC modeling fit normalized experimental data and modeled results (with fitting parameters of diffusion length L and surface recombination velocity to diffusivity ratio, S/D) for a range of electron beam energies [81, 82]. By normalizing both experimental and modeled data, these approaches look to fit only the shape of the EBIC signal, and omit valuable information obtained from the relative magnitude of the EBIC signal as a function of beam currents and energies [87]. This results in uncertainty in the extracted parameters, with broad ranges of L and S/D offering similar fits to the experimental data, thus weakening the significance of the extracted data. For EBIC measurements on bulk materials and large areas or cross-sections with weak surface recombination and long diffusion lengths, these uncertainties are minimized, but this is not the case for more complicated devices, having shorter active regions, multiple material layers, and/or significant surface recombination. By retaining both the shape and the magnitude of the EBIC signal, improvements to the fit of the EBIC data, as well as improvements to the uncertainty in the extracted data, can be achieved. In addition, the comparison of excited EHP densities (which can be obtained from the beam energy and current) and the magnitude of the collected current can provide additional insight into carrier dynamics in devices, potentially offering the opportunity to observe transitions where carrier lifetimes are changing as a function of excess carrier concentration. Thus, it is conceivable that a new approach to EBIC modeling, which takes into account not only the shape of the EBIC data, but also its relative magnitude, would offer the potential to realize the full capability of EBIC.

One example of the more complex devices mentioned above is the set of material systems leveraging strained layer superlattices (SLS), such as InAs/GaSb, InAs/InAsSb, and InGaAs/InAsSb, which have attracted significant interest over the past few decades due to their potentially superior performance in detecting mid-wave or long-wave infrared (MWIR or LWIR) light [60, 88, 89, 90, 91, 92, 93, 94, 95, 96, 97, 98, 99, 100]. Compared to the already commercialized state-of-the-art mercury cadmium telluride (MCT) detectors or quantum well infrared photodetectors (QWIPs), SLS detectors have competitive advantages such as a theoretically higher operating temperature, a suppression of Auger recombination, and an ability to control the detectors' effective band-gaps by engineering layer thicknesses in a binary system of ternary or quaternary alloys [88, 91]. However, the theoretically superior performance of SLS detectors is yet to be demonstrated experimentally or commercially, with material defects and growth imperfections considered as the major limiting factors for these infrared detector material systems [96, 101, 102]. Improving the material quality of SLSs requires techniques to characterize and understand the carrier dynamics of this material. However, characterizing material quality, and understanding the effect of material quality on device operation, for the narrow effective band-gap SLSs, often consisting of hundreds of alternating layers of alternating group V materials, and the potential concerns regarding intermixing, strain, and defect formation, requires a multi-pronged approach. Invaluable information can be gleaned from electron microscopy [101, 102, 103] and optical and electronic material and device characterization techniques [94, 96, 98, 99]. In addition, various techniques are already being utilized for measuring the minority carrier lifetime of SLSs [60, 98]. However, no viable technique has been reported so far to measure the vertical mobility, which is the other most important parameter for SLS detectors. EBIC offers a potential approach for characterizing both material quality and device operation, measuring the minority carrier diffusion characteristics of SLS materials, and has been

utilized as a valuable supplemental characterization tool for understanding material quality, for instance in InAs/GaSb SLS detectors as a function of interfacial layers [81] and for the promising Ga-free InAs/InAsSb T2LS material system [82]. The latter SLS material system has attracted growing interest resulting from demonstrated reductions in dark currents and longer minority carrier lifetimes compared to the early versions of SLS detectors employing the InAs/GaSb material system, hypothesized to result from the absence of native Ga-associated defects in the GaSb layers [60, 95, 97]. Recently, the introduction of Gallium into the InAs layer of InAs/InAsSb SLSs has been proposed as a possible improvement to SLS detector active region design, and has been experimentally shown to improve the detector absorption coefficient due to increased overlap of electron and hole states in the superlattice [1]. In addition, the InGaAs/ InAsSb SLS material system, when compared to the Ga-free InAs/InAsSb material system, is theoretically expected to show higher vertical hole mobility due to reduced hole effective mass. However, the diffusion length and vertical carrier mobility in these SLS structures, key parameters for understanding carrier dynamics and potential device performance in the material system, are yet to be investigated.

In Chapter 4, we investigate the effect of the Ga content in In(Ga)As/InAsSb SLS detector devices using a combination of time-resolved photoluminescence (TRPL) and EBIC measurements, leveraging a new approach to EBIC parameter extraction. We demonstrate that the previous approaches to EBIC modeling leave uncertainty in the fitting parameters for our SLS materials, and demonstrate our new numerical approach to EBIC modeling which improves the spatial resolution of our model and reduces the uncertainty in our extracted fitting parameters, modeling not only the EBIC lineshape as a function of position, but the magnitude of the EBIC response. We use the latter to better understand the effects of non-equilibrium carrier concentration on the minority carrier transport properties, and discuss the limitations of EBIC associated with changes in minority carrier lifetime at

higher non-equilibrium carrier concentrations. We apply our developed numerical EBIC modeling technique to understand the behavior of our In(Ga)As/InAsSb SLSs and discuss the agreement and discrepancies between our developed model and experimental results. The extracted fitting parameters are compared to those extracted using external quantum efficiency measurements performed on the same material with good agreement.

Chapter 4

InGaAs/InAsSb SLS Devices with Varying Ga Content

[1]Due to the great interest in type-II superlattices (T2SLs), a range of combinations of epitaxially grown materials have been explored as potential T2SL systems, as briefly discussed in Chapter 1.4.3. Although these efforts have mostly focused on the InAs/Ga(In)Sb and InAs/InAsSb superlattice systems, there remains interest in exploring and understanding the properties of alternative superlattice material systems for IR detector development.

InGaAs/InAsSb strained-layer superlattices (SLSs) are a relatively new material system offering mid-wave infrared (MWIR) light absorption and detection. In this chapter, In(Ga)As/InAsSb strained-layer superlattices (SLSs) are studied as a function of the Ga content of the In(Ga)As layer. We investigate detector devices with superlattices consisting of: InAs/InAsSb, $In_{0.95}Ga_{0.05}As$/InAsSb, and $In_{0.80}Ga_{0.20}As$/InAsSb. The introduction of Ga into the InAs layer has been suggested to offer three potential advantages when compared to the original Ga-free T2SL material system InAs/InAsSb: 1) InGaAs provides greater opportunity for strain compensation, because the addition of Ga to the InAs allows for control of the In(Ga)As lattice constant, offering strain balancing with thinner InGaAs layers (when compared to the InAs thickness of a comparable superlattice). 2) The InGaAs/InAsSb bandstructure offers increased electron-hole wavefunction overlap, and thus enhances infrared

[1]This work has been published as "Modified electron beam induced current technique for In(Ga)As/InAsSb superlattice infrared detectors" in J. Appl. Phys., vol. 122, no. 7, p. 074053, 2017. The first author, N. Yoon, has contributed to the majority of the work except the SLS material growth and EQE measurements, which have been performed by the authors at AFRL.

absorption, and 3) the effective mass of holes decreases, offering a potential improvement in the vertical hole mobility [68].

Before discussing the techniques employed to characterize our detectors, we begin by detailing the layer structure and device design of the $In_{1-x}Ga_xAs$/InAsSb samples investigated. We then go on to describe the photoluminescence (PL) measurements performed to determine the materials' effective band gaps. The carrier lifetimes are extracted via time-resolved photoluminescence (TRPL) measurements on the bulk materials. Then these samples are fabricated into detectors to perform electron beam induced current (EBIC) measurements. As discussed in Chapter 3, the previous analytical approach and the modified numerical approach are used to extract minority carrier diffusion lengths. Following the presentation of the EBIC measurements, we discuss the general trends observed and any discrepancies between samples and between characterization techniques.

The temperature-dependent EBIC measurements provide diffusion lengths for our devices as a function of temperature. However, a more holistic understanding of minority carrier transport is achieved when the extracted diffusion lengths are combined with minority carrier lifetimes (τ_p). Based on the diffusion length equation, $L_h = \sqrt{D_h \tau_p}$, and the Einstein relationship, $D_h/\mu_h = kT/q$ [20], the hole diffusivity (D_h) and the minority carrier vertical mobility (μ_h) can be extracted. The vertical hole mobilities extracted from EBIC show a good agreement to those calculated from EQE measurements, and our results experimentally verify the expected increase in vertical hole mobility with increasing Ga-content of our absorber materials.

Ga fraction, x (%)	$In_{1-x}Ga_xAs$ thickness (Å)	$InAs_{0.65}Sb_{0.35}$ thickness (Å)	# of Periods	Calc. Bandgap (eV)
0	51.73	16.73	292	0.252
5	39.56	19.78	337	0.255
20	25.86	27.38	376	0.252

Table 4.1: Design parameters for three different Ga-dependent $In_{1-x}Ga_xAs/InAs_{0.65}Sb_{0.35}$ SLSs, reproduced from Ref. [1]. The layer thicknesses used were chosen such that each of the SLSs would have similar calculated bandgaps.

4.1 Sample Designs

To study the effect of gallium composition in $In_{1-x}Ga_xAs/InAs_{0.65}Sb_{0.35}$ SLSs, samples were grown (by collaborators at AFRL) with varying molar fraction of Ga in the $In_{1-x}Ga_xAs$ layer ($x = 0.0$, $x = 0.05$, and $x = 0.20$). For each of these samples, while the Ga content differs, the thickness of each layer has been adjusted in order to achieve similar calculated effective bandgaps. Table 4.1 shows the design parameters for each [1].

Three In(Ga)As/InAsSb based nBn infrared photodetectors, grown by molecular beam epitaxy (MBE) on GaSb substrates, were investigated in this work. From the bottom to top, our devices consist of a GaSb buffer layer, a 2 μm n-type SLS absorption layer (n-doped 2×10^{16} cm^3), an undoped 200 nm AlGaAsSb electron-blocking barrier layer, and a 200 nm n-type SLS top contact (n-doped 2×10^{16} cm^3). The three different SLS designs are: 17 ML InAs/5.5 ML $InAs_{0.65}Sb_{0.35}$ (0% gallium content), 13 ML $In_{0.95}Ga_{0.05}As$/6.5 ML $InAs_{0.65}Sb_{0.35}$ (5% gallium content), and 8.5 ML $In_{0.80}Ga_{0.20}As$/9ML $InAs_{0.65}Sb_{0.35}$ (20% gallium content), each designed to be strain balanced and also to have similar effective band-gaps. Figure 4.1 (a) shows the schematic of the layer structure and device geometry of the SLS devices investigated in this work. Figure 4.1 (b) shows the orientation of the fabricated device under the SEM for the cross-sectional EBIC measurements, along with a schematic of the bandstructure of the nBn structured devices. Figures 4.1 (c-e) show the band diagram

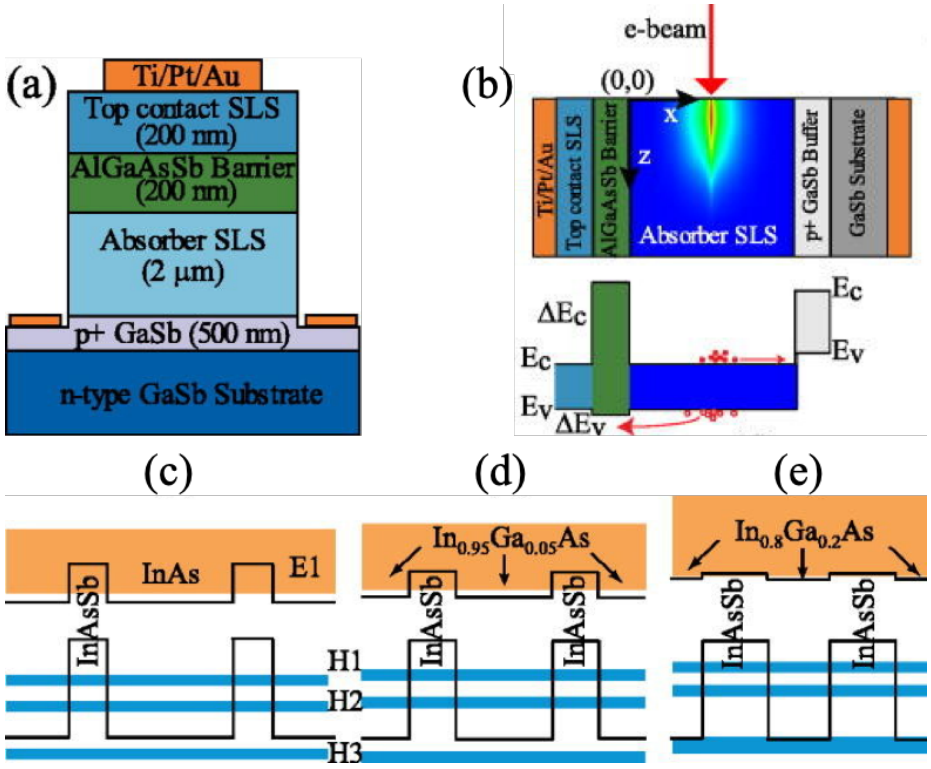

Figure 4.1: (a) Schematic of the layer structure and device geometry of the tested SLS infrared detectors, (b) EBIC experimental configuration with contour plot of generation distribution superimposed over the absorber region. Also shown is a band structure schematic of the detector samples studied.. Conduction and valence band profile along with electron and hole minibands for two periods of the (c) InAs/$InAs_{0.65}Sb_{0.35}$, (d) $In_{0.95}Ga_{0.05}As/InAs_{0.65}Sb_{0.35}$, and (e) $In_{0.80}Ga_{0.20}As/InAs_{0.65}Sb_{0.35}$ SLSs used for the absorber regions

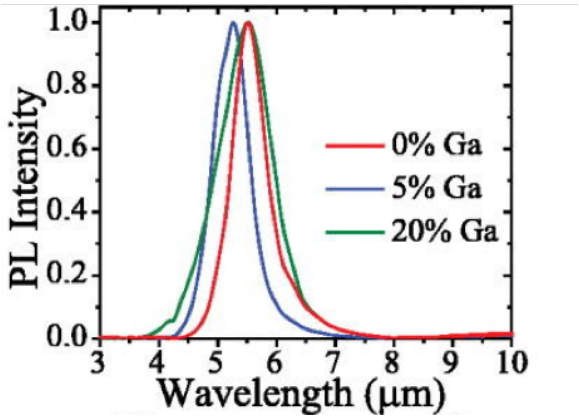

Figure 4.2: Normalized photoluminescence (PL) spectra of all three detectors at 80 K, showing similar cut-off wavelengths for each of the three designs: InAs / $InAs_{0.65}Sb_{0.35}$ (red), $In_{0.95}Ga_{0.05}As$ / $InAs_{0.65}Sb_{0.35}$ (blue), and $In_{0.80}Ga_{0.20}As$ / $InAs_{0.65}Sb_{0.35}$ (green).

of two periods of the three different absorbers: InAs/InAsSb, $In_{0.95}Ga_{0.05}As$/InAsSb, and $In_{0.80}Ga_{0.20}$ As/InAsSb designs, respectively.

4.2 PL and TRPL data

Samples were initially characterized with a Bruker v80V Fourier transform infrared (FTIR) spectrometer, using mid-IR photoluminescence (PL) spectroscopy in an amplitude modulation step-scan experiment. Figure 4.2 shows the low temperature (80 K) PL spectra for each sample, indicating similar cut-off wavelengths for the three SLSs detectors investigated in this work.

The same samples were also characterized using temperature dependent time-resolved photoluminescence (TRPL), as discussed in Chapter 2.2. The as-grown samples were pumped with a Q-switched diode-pumped laser emitting 1 ns pulses at λ = 1064 nm, with 10 kHz repetition rate and varying pulse energies (controlled by neutral density filters at the laser output). The light emitted from the samples is collected with a parabolic mirror, and focused onto a high-speed MCT detector (Kolmar Technologies) using a Ge lens (which

also serves, along with a long-pass filter at 3.6 μm , to block the scattered pump laser light). The output of the MCT detector is collected using a 14-bit LeCroy oscilloscope and the tail of the PL emission for all pulse energies is modeled using a single-exponential fit in order to extract the low-injection minority carrier lifetime [104]. TRPL data are collected from all samples for temperatures from 80 K to 200 K.

Time-resolved photoluminescence (TRPL) spectroscopy allows for the measurement of the minority carrier lifetime in the low injection regime, where typical IR detectors operate. The full expression for carrier lifetime in a SLS is most accurately expressed as [95]

$$\tau^{-1} = \frac{(n_o + \delta n)}{\tau_{po}(n_o + \delta n)} + B(n_o + \delta n) + C_n(n_o + \delta n)^2, \tag{4.1}$$

where δn is the excess carrier concentration, τ_{po} and τ_{no} are the minority and majority carrier Shockley-Read-Hall (SRH) lifetimes, B is the bulk radiative coefficient, and C_n is the Auger recombination coefficient.

For low injection, $\delta n << n_o$, and lightly doped material ($n_o < 2.5 \times 10^{15} cm^{-3}$), the minority carrier lifetime is dominated by the contributions from SRH and radiative recombination, and can be described by a single value for lifetime (independent of excess carrier concentration). Recent results have demonstrated that for more highly doped material ($n_o > 2.5 \times 10^{15} cm^{-3}$), the low injection lifetime is dominated by Auger recombination, although the resulting TRPL data can still be fitted with a single exponential [105]. Figure 4.3 shows the TRPL results from all of our samples for temperatures of 80, 120, 160, and 200 K, using a single-exponential fit to the tail of the TRPL data, from which we can extract the temperature dependent carrier lifetime. From these data we observe decreasing carrier lifetimes with increasing Ga content of our samples, with the 0% Ga sample showing

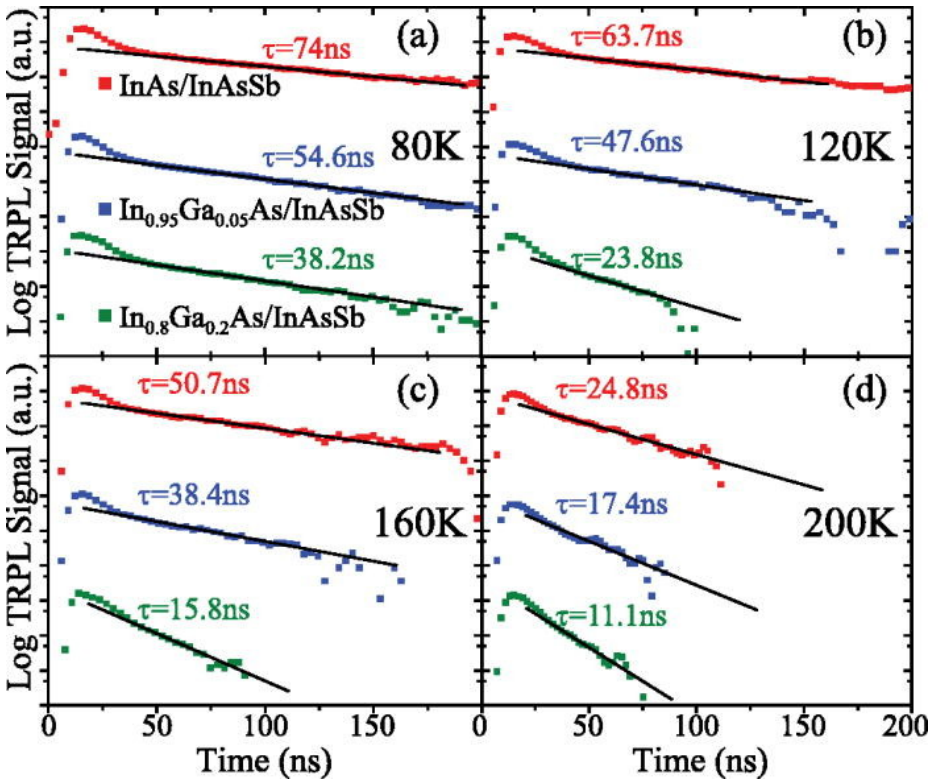

Figure 4.3: Time-resolved photoluminescence (TRPL) signals (scatter) from InAs / $InAs_{0.65}Sb_{0.35}$ (red), $In_{0.95}Ga_{0.05}As$ / $InAs_{0.65}Sb_{0.35}$ (blue), and $In_{0.80}Ga_{0.20}As$ / $InAs_{0.65}Sb_{0.35}$ (green), detector samples at (a) 80K, (b) 120 K, (c) 160 K, and (d) 200 K, with exponential fittings (solid lines) and the extracted low-injection carrier lifetimes shown for each temperature and sample.

a factor of 2 or greater lifetime than the 20% Ga sample across the entire temperature range investigated. All samples display similar decreases in minority carrier lifetimes as temperature increases, an indication that the extracted carrier lifetime is an Auger-limited lifetime, as opposed to resulting from SRH recombination, as would be expected at our intended doping concentrations of $n_o = 2 \times 10^{16} cm^{-3}$ [105]. The observed decrease in carrier lifetime with increased Ga concentration, in a more lightly doped SLS, could indicate the presence of additional defects associated with Ga in our SLSs. Alternatively, the decrease in lifetime with increasing Ga could result from the increased overlap between electron and hole wavefunctions in the InGaAs/InAsSb SLS material system [1, 68], and thus shorter radiative recombination times. However, low-injection lifetimes in our material system, as discussed above, are most likely Auger-limited. Thus, from the lifetime data alone, it cannot be said that the presence of Ga either introduces non-radiative recombination centers or improves radiative lifetimes in the SLS structure. The decrease in lifetime as a function of Ga content is more likely a result of changes in the Auger lifetime of our highly doped samples, an effect we will discuss below.

4.3 Experimental Setup for EBIC

The EBIC measurements were carried out on detector devices which are fabricated into mesa structures with solid, continuous metal contact pads. The fabrication process is documented in Appendix A. For the cross-sectional EBIC measurements, the fabricated devices are cleaved through the top contact and mesa, and then mounted in the chamber of a JEOL 7000F scanning electron microscope (SEM) such that the cleaved surface is positioned normal to the SEM's electron beam. As shown in Figure 4.4, the sample substrate is mounted to the SEM stage, and the top and bottom contacts to the detector are wire-bonded to ceramic stand-offs, connected to BNC cables.

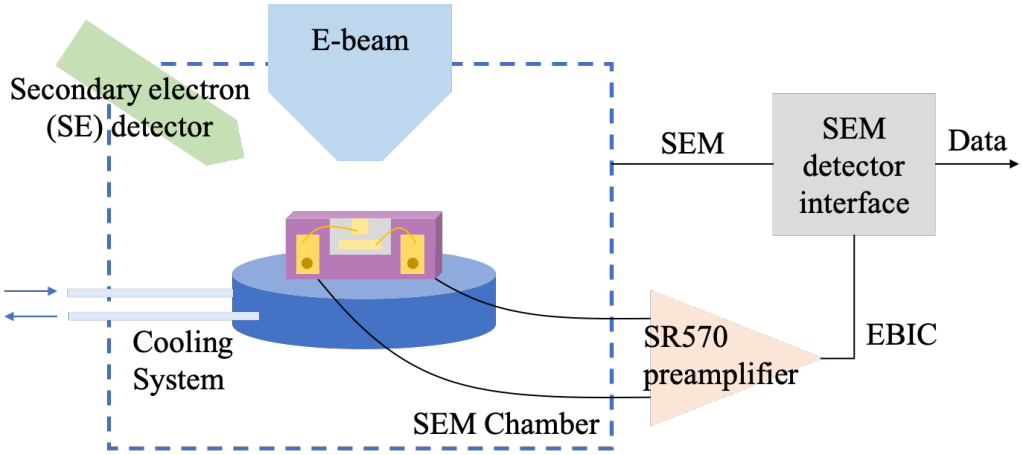

Figure 4.4: The experimental setup for the electron beam induced current (EBIC) using the scanning electron microscope (SEM). With a stage cooling system, the temperature dependent EBIC study can also be performed.

The current collected across top and bottom contacts of the device is amplified using a Stanford Research SR570 pre-amplifier connected via electrical feedthroughs in the SEM. The output of the pre-amplifier is fed into the SEM DigiScan control software and a "current image" of the sample is generated. It is important to note that this current image includes not only the EBIC signal, but also a DC dark current from the sample. This dark current (measured in the EBIC image as the current far from the collection junction) is removed from the final EBIC signal with a uniform background subtraction. The remaining EBIC image is averaged [parallel to the growth plane, along the y-direction of Figure 4.1 (b)] to produce a 1D EBIC profile as a function of beam position in the growth direction. Each device is measured at temperatures from 80 K to 200 K with beam energies ranging from 10 keV to 30 keV in 5 keV increments. The experimental EBIC profile is compared to the modeled profile, which allows for an extraction of the minority carrier diffusion length, L, and the surface recombination velocity to diffusivity ratio, S/D.

4.4 Comparison of EBIC Modeling Methods

In Chapter 3.4, two different EBIC modeling methods are discussed for modeling the carrier generation volume (Chapter 3.4.1. We describe these as the traditional analytical method and our modified numerical method. Figure 4.5 shows the contour plot generated from this fitting process for both the analytical [Figure 4.5 (a)] integration and the numerical [Figure 4.5 (b)] summation approaches, in this case using our data from the InAs/InAsSb SLS device at 120 K as representative data. For this figure, we plot the normalized fit error between the two approaches as a function of our two fitting parameters: diffusion length and surface velocity to diffusivity ratio.

A number of features can be observed from the comparison offered by Figure 4.5. First, we see that the effect of the S_h/D_h parameter on our fit quality is minimal, particularly for low S_h/D_h values ($< 0.1\mu m^{-1}$). This is to be expected, as once the surface recombination is slower than the diffusion of carriers toward the junction (effectively the carrier lifetime τ_p), one would not expect surface recombination to have a significant quantitative effect on the model. In addition, we do observe a narrower range of our fit quality when we utilize the numerical integration technique, suggesting at least a slight reduction in the uncertainty of the extracted L_h term, presumably a result of the improved spatial resolution offered by employing the raw output of our Monte Carlo simulations, as opposed to the analytical fit to this simulation. Once the best fit for the L_h and S_h/D_h parameters is obtained for the low energy electron beams, we model the higher beam energies by inserting the L_h and S_h/D_h, extracted for low beam energies, into the expression for $\phi(x_i, z_j)$ and now using generation distribution, $h_{E_b>15\text{keV}}(x_i - x_o, z_j)$ obtained for the higher beam energy, and the beam current measured for the higher beam energy conditions, we calculate the new EBIC

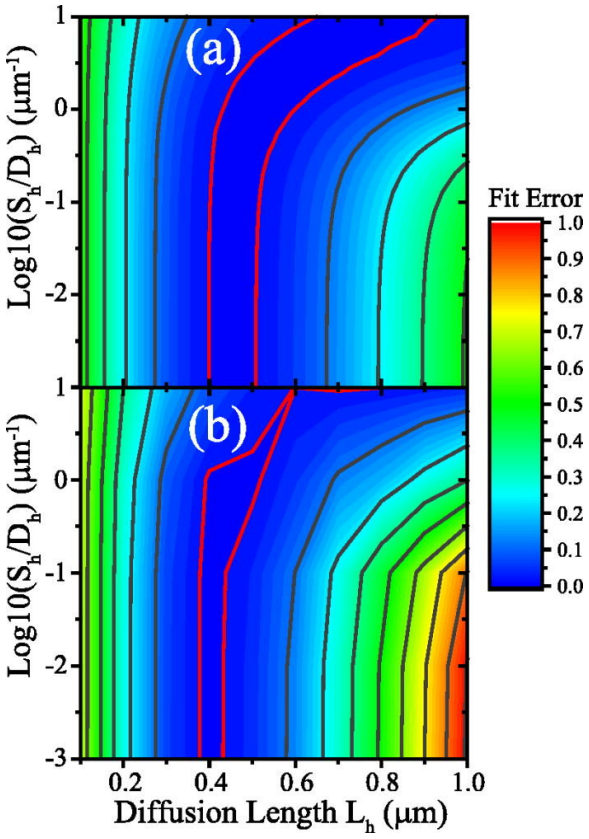

Figure 4.5: Contour plot of the normalized fit error between the low beam energy experimental data and modeled EBIC data obtained using (a) analytical and (b) numerical integration approaches as a function of the fitting parameters L_h and $S_h = D_h$. The experimental data used come from the InAs/InAsSb SLS device at 120 K. The calculated fit error for each approach, (a) analytical and (b) numerical integration, is normalized to the same value. In the plots above, we use the maximum calculated fit error of the numerical integration approach (b) across the parameter space investigated (the axes of our contour plots), as our normalization constant. Red lines show normalized SSE = 0.02, for comparison of fit uncertainty.

curve. For a beam energy of 20 keV, this would appear as

$$I_{20\text{keV}}(x_o) = \frac{\eta_{20\text{keV}}(x_o) I_{beam}(20\text{keV})}{N A_{mod} I_{beam}(10\text{keV})}, \text{ where now } I_{20\text{keV}}(x_o = 0) \neq 1. \tag{4.2}$$

The result of this approach is an EBIC curve scaled in amplitude (due to the changes in I_{beam} and $\eta_{E_b>15\text{keV}}$), with only slight changes in the EBIC profile shape resulting from the change in the carrier generation distribution at higher beam energies. The immediate and clear benefit of this approach is the ability to model not only the change in the EBIC profile, but the amplitude as well. Figure 4.6 (a) shows, for 10 and 15 keV beam energies, the comparison of our normalized experimental data to the normalized EBIC model using the analytical fit to the carrier generation profile. Thus for the data of Figure 4.6 (a), we scale both our modeled and experimental $I_{E_b}(x)$ such that, once again, $I_{10\text{keV}}(x_o = 0) = I_{15\text{keV}}(x_o = 0) = 1$, and in doing so lose any information regarding the relative strengths of the EBIC signals. In Figure 4.6 (b), however, we show the comparison of modeled and experimental data using our numerical approach [Equation 4.2]. Here, the experimental data are scaled by the very same factor as our 10 keV data, $A_{exp}(10\text{keV})$, while the scaling of our modeled data uses both the same factor as our 10 keV model, A_{mod}, and the additional scaling coming from the change in the beam current. Thus, the change in the magnitude of the modeled EBIC profile results from measurable experimental parameters (beam energy and current), more accurately reflecting the change in experimental parameters with increasing beam energy.

The advantage of this approach can be clearly seen in Figure 4.6 (b), where we observe excellent fits to both the shape and magnitude of the EBIC profile. As indicated in Figure 4.6, our averaged sum of squared error (SSE) for the 10 and 15 keV data improves from 0.0577 to 0.0346 using our numerical EBIC approach. At higher beam energies, the normalized EBIC model will give better fits, for reasons discussed later.

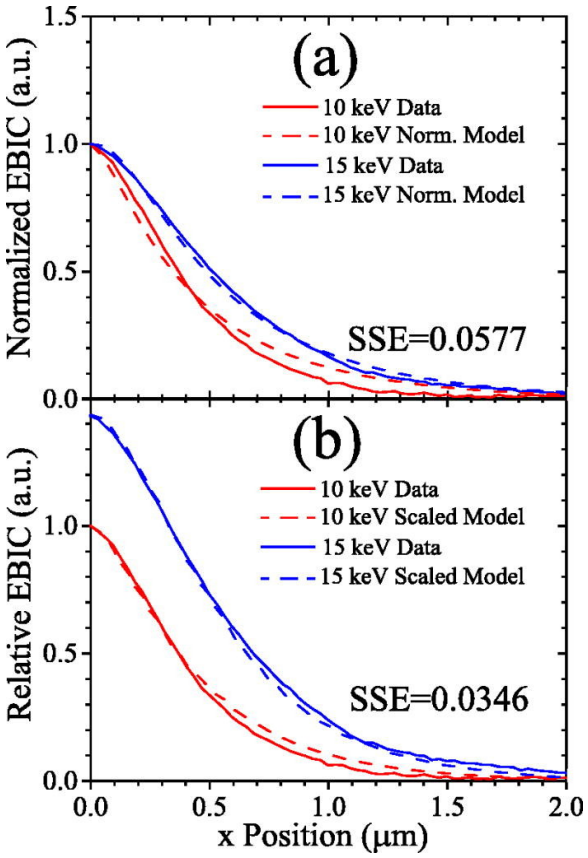

Figure 4.6: Experimental and modeled EBIC data for the InAs/InAsSb detector device at 120 K for beam energies of 10 and 15 keV. (a) Experimental data (solid) and modeled fit using analytical expression for $h_{E_b}(\tilde{x}-x_o, \tilde{z})$ (dashed), with experimental and modeled data normalized for each beam energy. (b) Experimental data (solid) and modeled fit using numerical expression for $h_{E_b}(\tilde{x}_i - x_o, \tilde{z}_j)$ (dashed), with modeled and experimental data for 15 keV is scaled by A_{mod} and A_{exp} , respectively, which were determined by fitting to the 10 keV data. The averaged fit error (SSE) for each approach is shown in each plot.

Our approach to EBIC modeling not only offers improved fitting to the experimental data with decreased uncertainty in the extracted values of L and S/D, but also allows us to predict the amplitude of the EBIC signal for increasing beam energies, as we can see in Figure 4.6 (b). This will provide us with additional valuable data points for understanding EBIC measurements of our samples. Below we discuss the results from the samples investigated, and benefits and challenges of the EBIC modeling technique described above.

4.5 EBIC data

As discussed in the previous section, two different parameter extraction methods are performed. The traditional analytically-modeled EBIC is fitted to the normalized EBIC data independent of the beam energies, while the modified numerical EBIC modeling is applied to the relative EBIC profiles. Then, our EBIC data are compared to values for the vertical hole mobility extracted from external quantum efficiency (EQE) measurements. In this section, the minority carrier lifetime, τ, and the minority carrier diffusion lengths, L, will be extracted using TRPL and our modified EBIC technique. In addition, we compare the results from our EBIC measurements with those extracted using an external quantum efficiency (EQE) measurement approach.

Extracting our temperature dependent lifetime from the TRPL measurements [Figure 4.7 (a)], and our temperature dependent diffusion length from the numerical model of the EBIC measurement [Figure 4.7 (b)], we are able to measure the vertical hole mobility for each of the SLS samples as a function of temperature. Figure 4.7 (c) shows the resulting temperature dependent vertical hole mobility for all three of our samples, where the uncertainty shown in our data is determined using the SSE < 0.02 metric depicted in Figure 4.5. In a separate analysis, the hole diffusion lengths for the same set of samples were determined by fitting the experimental external quantum efficiency (EQE) of the

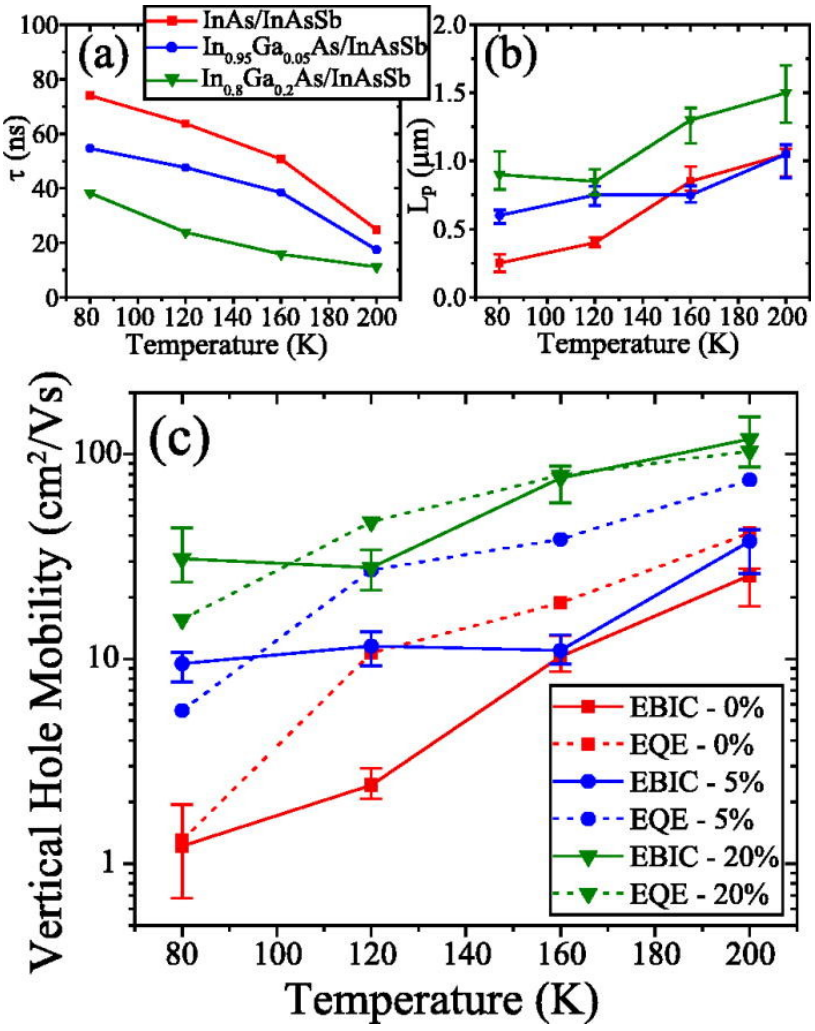

Figure 4.7: (a) Plot of minority carrier lifetimes at low injection levels as a function of temperature for the InAs/InAsSb (red), $In_{0.95}Ga_{0.05}As$/InAsSb (blue), and $In_{0.80}Ga_{0.20}As$/InAsSb (green) samples. (b) Extracted minority carrier diffusion lengths (Lh) for InAs/InAsSb (red), $In_{0.95}Ga_{0.05}As$/InAsSb (blue), and $In_{0.80}Ga_{0.20}As$/InAsSb (green) samples. (c) Vertical hole mobility for both InAs/InAsSb (red), $In_{0.95}Ga_{0.05}As$/InAsSb (blue), and $In_{0.80}Ga_{0.20}As$/ InAsSb (green) samples, as determined by EBIC (solid) and EQE (dashed) techniques.

detectors to the theoretically expected EQE at temperatures in the same range (80-200K). The EQE experimental approach is detailed in Ref. [69], and requires careful absorption and reflection measurements with a (spatially and spectrally) well-calibrated IR light source, and accurate current measurements, which when combined with an analytical model, allow for the extraction of the minority carrier diffusion length. Using the values of L_h extracted from the EQE measurements and the TRPL lifetime values, a second set of values for the vertical hole mobility was obtained. We compare the results from the EQE and EBIC measurements in Figure 4.7 and both approaches show vertical hole mobilities increasing as a function of temperature. In addition, both the EQE and EBIC techniques show increasing mobility, at all temperatures, for increasing Ga content in the SLS samples. Finally, we also observe a significantly stronger temperature dependence, across the T = 80 K to T = 200 K range of temperatures investigated, for the 0% Ga SLS sample (a factor of 20 increase) than the 5% and 20% Ga samples (factors of 4 and 5, respectively).

The increase in vertical carrier mobility with increasing Ga content can be understood by recalling that a primary benefit of the addition of Ga to the InAs layers of an InAs/InAsSb SLS is the increase in the wavefunction overlap between electron and hole states in the SLS [68]. This overlap is caused not only by the weaker quantization of the states in the conduction band (due to the decrease in the conduction band offset between the InAsSb and the In(Ga)As), but also from the decrease in thickness of the In(Ga)As barriers between the hole states in the InAsSb, which allows increased extension of hole states into the In(Ga)As hole barriers (which for the 20% Ga sample are only 8.5 ML thick), and thus improved vertical transport. Band structure calculations of the vertical hole effective mass indicated that the effective mass decreased from 2.97 m_o to 1.49 m_o as the gallium composition was increased from 0 to 20%. These calculations do not take into account intersubband scattering effects [106], which could explain the discrepancy between the expected change

in mobility and the actual change.

4.6 Discussion

Previous approaches to EBIC modeling search for the optimized fitting parameters (L and S/D) which most accurately fit the EBIC profiles (lineshapes) for all beam energies. The argument for this approach is that at higher beam energies, the carrier generation volume probes deeper into the device, essentially providing a variation in the effective depth of the average EHP generated. Finding the optimized fitting parameters for all beam energies is thus argued to offer the ability to extract a more accurate S/D value. However, for many material systems, large variations in the S/D value have little to no effect on the accuracy of the fit to EBIC data, as can clearly be observed in Figure 4.5. In fact, for the normalized EBIC fittings, many different combinations of L and S/D values can produce very similar EBIC profiles, with a greater uncertainty in the extracted diffusion length. At the same time, by focusing solely on the EBIC profile, it is possible that this technique discards valuable information which could be extracted from the relative magnitudes of the EBIC profiles. Using our scaled EBIC fittings, however, not only do we decrease the uncertainty in extracted L_h and S_h/D_h for a given experimental condition, we are able to use the relative magnitude of our modeled EBIC signal to obtain improved fits and qualitative information regarding the performance of our devices as a function of excess carrier concentration.

Figure 4.8 (a) shows the scaled fits to our EBIC data for the 0% Ga SLS sample at 120 K for all of the beam energies investigated in this work, in addition to the 10 and 15 keV data already presented in Figure 4.6 (b). The fits to our experimental data become progressively poorer as we move to higher beam energies. We can understand this effect by returning to our expression for carrier-dependent lifetime in Equation 4.1, which indicates that for higher carrier concentrations, we would expect a decrease in the average lifetime

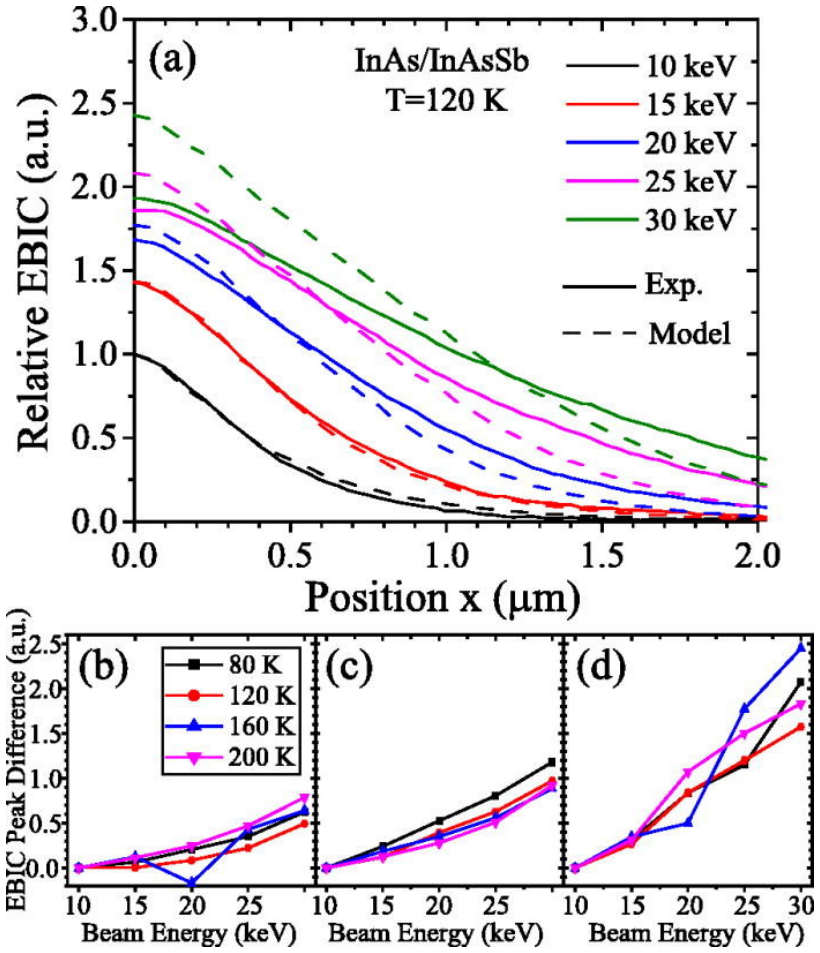

Figure 4.8: (a) Experimental (solid) and modeled (dashed) EBIC profiles for InAs/InAsSb SLS at T = 120K as a function of beam energy. Difference between modeled and experimental beam current at the SLS junction (x = 0) for the (b) InAs/InAsSb and (c) $In_{0.95}Ga_{0.05}As$/InAsSb and (d) $In_{0.80}Ga_{0.20}As$/InAsSb SLSs as a function of beam energy for all temperatures investigated.

of excited carriers due to increased Auger recombination, regardless of whether our SLS minority carrier lifetime is Auger- or SRH-limited at low excess carrier concentrations. A higher beam energy results in not only a broader carrier generation distribution, but also significantly higher carrier concentration (which is also affected by beam current). Thus, it would be expected that as we increase beam energy (and/or current), we would observe an increased deviation from our EBIC model (which we fit to the low beam energy data).

In fact, the deviation from our fit offers qualitative information regarding the carriers effectively "lost" to increased recombination rates (Auger) in our experiment. Figures 4.8 (b)-(d) show the difference between our scaled experimental and modeled EBIC signal at the SLS junction ($x = 0$) for the samples studied in this work. A largely monotonic increase in the deviation is observed for all samples at all temperatures (with the exception of one outlier data point: the 160 K, 20 keV data for the InAs/InAsSb SLS). In addition, we observe a weaker increase in the difference between our model and our data for the 0% Ga SLS than for the 5% Ga SLS, and significantly weaker than the 20% Ga SLS, whose experimental EBIC signal at high beam energies is far smaller than that predicted by our model. These results suggest that the effects of additional, carrier concentration-dependent, recombination mechanisms are correlated with increasing Ga content in our SLS structures. As Auger recombination is known to be quenched by increased quantization of charge carriers, the stronger signature of Auger recombination observed with increasing Ga content could be attributed to the decreasing conduction band offset and thus weaker quantization of conduction band electrons with increasing Ga content. Measuring the change in the difference between the modeled and experimental EBIC signal provides only a qualitative measure of the change in carrier lifetime. Future efforts will attempt to develop a quantitative understanding of this measure using samples with a clear transition between SRH and Auger limited lifetimes.

Previous approaches to EBIC modeling thus not only miss valuable information obtained from the relative magnitudes of the EBIC signal and model, but potentially could result in inaccurate parameter extraction. These approaches attempt to fit EBIC data from all beam energies simultaneously, including the higher beam energy data, where carrier lifetimes can be very different than for lower beam energy excitation. While this approach may be sufficiently accurate for materials with long diffusion lengths and relatively constant carrier lifetimes (small Auger coefficients), for materials with shorter diffusion lengths and larger Auger coefficients (such as narrow bandgap semiconductors), the fit to the data then may not accurately reflect the device parameters for typical operating conditions (low excess carrier concentration). Although our improved EBIC modeling technique is thus far only able to extract qualitative information regarding the behavior of our devices as a function of carrier concentration, the development of a more quantitative approach to understand the effects of beam energy (and/or current) on the EBIC profiles of our narrow bandgap materials can be done as a future work. In particular, we can investigate beam energy dependence of devices as a function of background doping. In doing so, we can also look to observe the transition between SRH- and Auger-limited lifetimes, either by control of beam energy or doping, and use these data to develop quantitative modeling techniques to extract device parameters as a function of excess carrier concentration.

In conclusion, we have presented a technique for modeling electron beam induced current measurements which offers improved fitting to experimental data, lower uncertainty in parameter extraction, and qualitative information on carrier dynamics as a function of carrier concentration. Our approach utilizes Monte Carlo-simulated carrier generation distributions combined with an expression for carrier diffusion modified for the devices investigated, with a numerical integration to obtain a modeled EBIC profile which more accurately fits our experimental data. We use the EBIC model presented to extract the minority carrier

diffusion length and the surface recombination velocity to diffusivity ratio for In(Ga)As/InAsSb strained-layer superlattice detectors with 0, 5, and 20% Ga content. Although we use the presented technique to measure vertical hole mobility in narrow bandgap SLS materials with nBn detector architectures and diffusion dominated transport, our approach could well be adapted for lateral mobility studies (plan view) or for studying alternative material systems and/or detector architectures, with adjustments to the probability of collection expression [Equations 3.12-3.15] and our Monte Carlo simulation parameters. Together with time-resolved photoluminescence (TRPL) measurements, we use our EBIC technique to extract the temperature dependent mobility of our samples. We observe increasing hole mobility as a function of the temperature, and higher mobilities for the InGaAs/InAsSb devices than the InAs/InAsSb device at all temperatures. In addition, we compare the deviation of our modeled EBIC response from the experimental data, and use this discrepancy to qualitatively understand the effect of additional recombination mechanisms, or changes in the existing recombination rates, in our samples. The In(Ga)As/InAsSb SLS material system provides the opportunity to investigate the effects of electron/hole wavefunction overlap in narrow bandgap materials by control of Ga content in the In(Ga)As layers. The extracted temperature dependent mobility and beam-energy dependent current amplitudes for our samples are discussed using the framework of wavefunction overlap and carrier quantization, and offer an understanding of the effects of bandstructure design on carrier dynamics in the SLS material system. The presented work offers an approach to electron beam induced current measurements and parameter extraction with improved fitting of the experimental data, lower uncertainty and the potential for measuring device properties as a function of injection regime. While in this work we investigate narrow bandgap SLS materials, the approach presented is applicable to the investigation of a wide range of semiconductor-based electronic and optoelectronic devices.

Chapter 5

InGaAs/InAsSb SLS Devices with Varying Layer Thicknesses

Continuing our EBIC studies of InGaAs/InAsSb strained-layer superlattices (SLS), this chapter discusses the dependence of SLS transport properties on the unit cell thickness of InGaAs/InAsSb superlattices. One of the challenges associated with SLS infrared photodetectors is that they tend to have poorer vertical transport properties than bulk materials of the same bandgap due to the inherent anisotropy of the SLS material system [107, 108, 109]. Designing SLS materials with improved vertical transport is desirable for improved carrier collection and photodetector operation. The vertical transport in superlattice systems has been studied for the GaAs/AlGaAs material system, using a photoluminescence characterization technique where emission from a quantum well below the superlattice is measured when the surface of the sample is excited optically. The PL intensity is expected to be proportional to the number of minority carriers which are able to diffuse to the buried QW, providing a measure of the diffusion length for the SL above the QW [110]. Later studies, using this technique, investigated diffusion length as a function of superlattice unit cell, and suggested an increase in vertical hole mobility with decreasing superlattice period, or unit cell thicknesses [111]. Moreover, with very thin layer thicknesses (period < 30Å), the vertical hole mobility was found to be comparable to that of alloys with the same fractional alloy composition as a single superlattice unit cell [111]. It is thus conceivable that the type-II and/or narrowband SL materials could exhibit improved vertical transport, in the form of increased vertical hole diffusion lengths, as the unit cell thicknesses of the SLs are

decreased. In this chapter we describe our studies of vertical transport in InGaAs/InAsSb superlattices with varying unit cell thicknesses. As we did in Chapter 4, sample designs are discussed first, then bulk, as-grown samples are characterized by performing photoluminesence (PL) and time-resolved photoluminesence (TRPL) measurements to obtain the effective bandgaps and the carrier lifetimes, respectively. These samples are then fabricated into detector devices to measure the electron beam induced current (EBIC) signal, which, with the help of careful modeling, gives a diffusion length (L) and surface recombination to diffusivity ratio (S/D). Then, the EBIC results are compared to external quantum efficiency (EQE) data obtained by our collaborators from Air Force Research Laboratory at Wright-Patterson.

5.1 Sample Designs

Four nBn $In_{0.88}Ga_{0.12}As/InAs_{0.65}Sb_{0.35}$ SLS photodetectors are grown by molecular beam epitaxy (MBE) on GaSb substrates. From top to bottom, these samples consist of a 200 nm n-type SLS top contact, a 200 nm electron barrier, 2 μm of SLS absorber material, a 200 nm p-type ($1 \times 10^{17} cm^{-3}$) GaSb contact layer, and then the GaSb substrate. Each SLS absorber material has different layer thicknesses: i) 2.5 ML $In_{0.88}Ga_{0.12}As$ / 2.5 ML $InAs_{0.65}Sb_{0.35}$ SLS, ii) 3 ML $In_{0.88}Ga_{0.12}As$ / 3 ML $InAs_{0.65}Sb_{0.35}$ SLS, iii) 6 ML $In_{0.88}Ga_{0.12}As$ / 6 ML $InAs_{0.65}Sb_{0.35}$ SLS, and iv) 9 ML $In_{0.88}Ga_{0.12}As$ / 9 ML $InAs_{0.65}Sb_{0.35}$ SLS. Table 5.1 shows the design parameters for the four $In_{0.88}Ga_{0.12}As/InAs_{0.65}Sb_{0.35}$ SLSs studied in this work. The bandgap calculation for each SLS, as denoted in Table 5.1, is performed by our collaborators at Air Force Research Laboratory, using NRL Band^{TM} software (integrated 8-band k·p and Poisson solver) [112].

Sample Name	$In_{0.88}Ga_{0.12}As$ thickness (Å)	$InAs_{0.65}Sb_{0.35}$ thickness (Å)	# of Periods	Calc. Bandgap (eV)
2.5 ML	7.62	7.62	1312	0.301
3 ML	9.14	9.14	1094	0.298
6 ML	18.29	18.29	547	0.281
9 ML	27.43	27.43	365	0.241

Table 5.1: Design parameters for the four $In_{0.88}Ga_{0.12}As/InAs_{0.65}Sb_{0.35}$ SLSs studied, with varying thickness unit cell periods.

Since the molar composition of both ternary materials are kept the same from sample to sample, the band offsets for the electrons and holes in the conduction and valence band stay the same, and the only factor that is changing is the thickness of each layer. Figure 5.1 shows the schematic of the conduction and valence band alignment, along with the effective bandgaps. The illustrations of the layer thicknesses are scaled accordingly for (a) 2.5 ML, (b) 3 ML, (c) 6 ML, and (d) 9 ML.

In the samples studied, both the conduction and valence band offsets are kept the same (due to their having the same molar compositions), while the well and the barrier thicknesses are changed. Since the conduction band offset for this material system is relatively small compared to the valence band offset, the position, in energy, of the lowest conduction band minibands are shown to be similar. As the thickness of each layer decreases, the ground state energy for the lowest hole miniband increases, so that the effective bandgap increases. This matches with the calculated bandgaps for these samples (Table 5.1), which decrease as the layer thickness increases. In addition to the change in the effective bandgap, the unit cell layer thickness can also impact the vertical hole mobility (the primary focus of this study). The 2.5 ML and 3 ML samples' layer thicknesses are thinner than 1 nm, which will increase the weighting of the hole wavefunction in the InGaAs valence band 'barriers'. Thus, these two samples are expected to have improved vertical transport and higher vertical

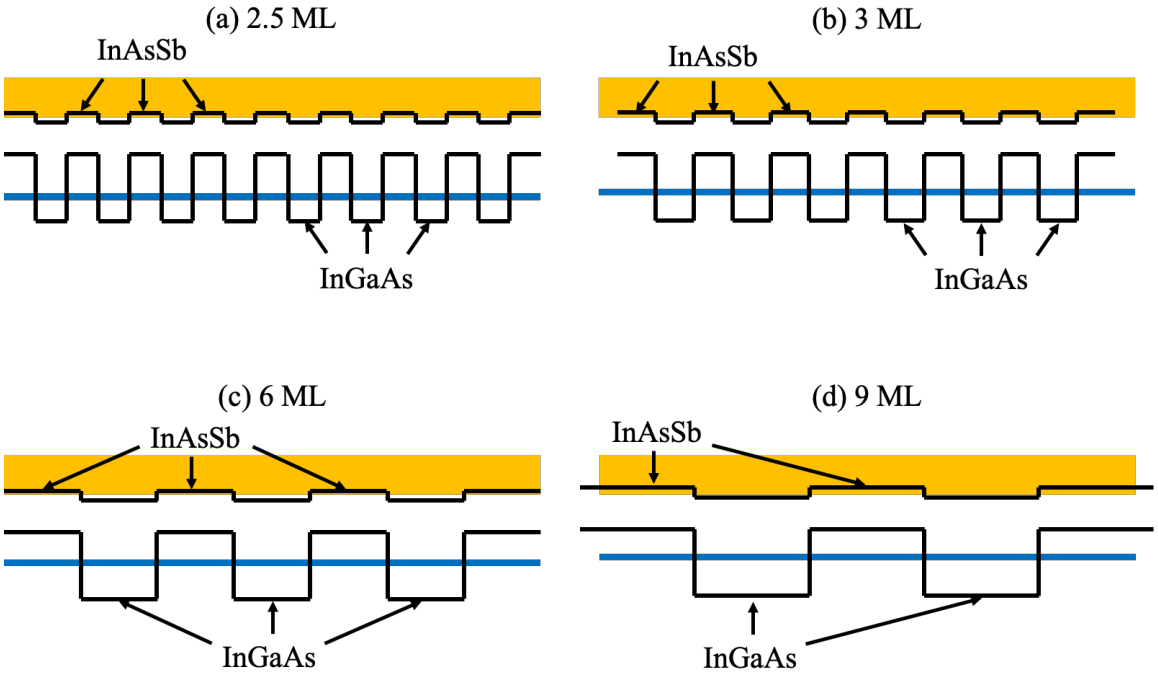

Figure 5.1: The conduction and valence band alignments, along with the effective band gaps, are illustrated for $In_{0.88}Ga_{0.12}As/InAs_{0.65}Sb_{0.35}$ SLSs with individual layer thicknesses: (a) 2.5 ML, (b) 3 ML, (c) 6 ML, and (d) 9 ML.

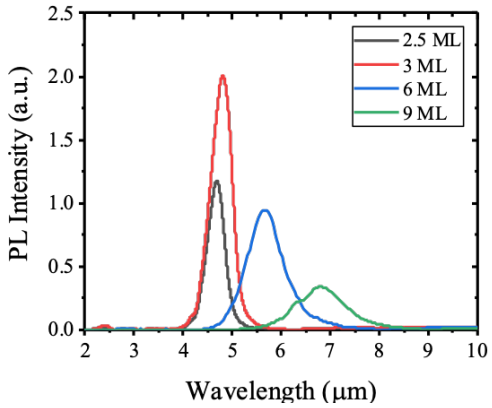

Figure 5.2: Relative PL spectra of four $In_{0.88}Ga_{0.12}As/InAs_{0.65}Sh_{0.35}$ SLS detectors at 80 K.

hole mobilities, similar to the results observed in the type-I superlattices (GaAs/AlGaAs) discussed above.

5.2 PL and TRPL Data

First we characterize the as-grown wafers with a Bruker v80V FTIR spectrometer, using mid-IR photoluminescence (PL) spectroscopy in amplitude modulation step-scan mode. Figure 5.2 shows the low temperature (80 K) PL spectra for each sample. The effective bandgap of the 2.5 ML sample is experimentally determined (based on the PL peak) to be ~4.69 μm (0.265 eV), 3 ML is ~4.80 μm (0.258 eV), 6 ML is ~5.67 μm (0.219 eV), and 9 ML is ~6.79 μm (0.182 eV) at 80 K. As can be seen in the PL spectra, increasing the thickness of the SLS unit cell results in a significant red-shift of the extracted effective bandgaps, an effect attributed to the decreased quantization of electron and hole wavefunctions in the conduction and valence bands of the SLS, as illustrated in Figure 5.1. As noted above, the majority of the shift in band gap energy comes from the change in the position of the first hole miniband.

Time-resolved photoluminescence (TRPL) measurements are performed on the

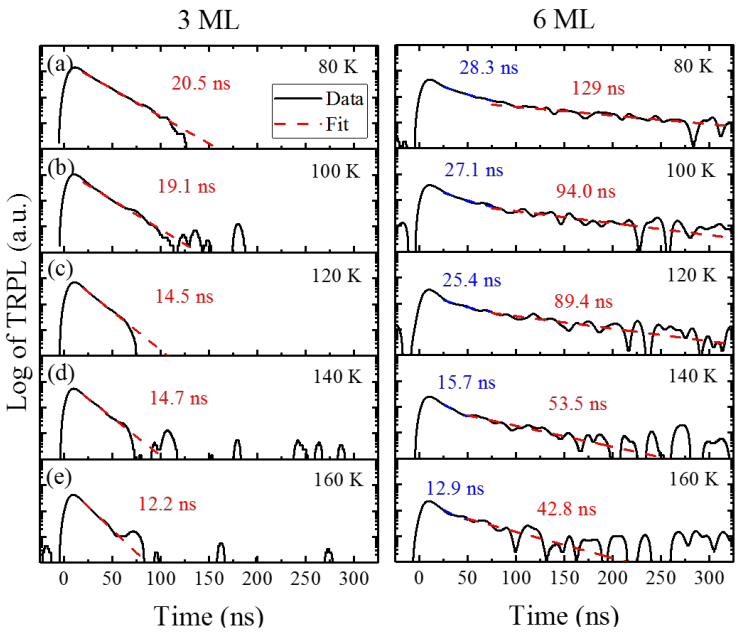

Figure 5.3: Representative time-resolved photoluminescence (TRPL) signals (solid lines) from 3 ML/3 ML InGaAs/InAsSb SLS (left) at (a) 80 K, (b) 100 K, (c) 120 K, (d) 140 K, and (e) 160 K, with exponential fittings (dashed lines), and TRPL data (solid lines) from 6 ML/6 ML InGaAs/InAsSb SLS (right) with two different exponential fittings (dashed lines).

same set of samples at various temperatures, as described in Chapter 4.2. Figure 5.3 shows representative TRPL signals with exponential fits for the 3 ML/3 ML InGaAs/InAsSb SLS (left) and those for 6 ML/6 ML InGaAs/InAsSb SLS (right) at various temperatures.

While the 2.5 ML and 9 ML samples show TRPL signals similar in form and decay rate to that of the 3 ML sample, the 6 ML sample shows a somewhat different time response. The 6 ML TRPL data appears to have at least two separate time constants associated with its decay, depending on where the exponential fitting is conducted. The 0-50 ns range shows a fast recombination time, similar to the times extracted for the other 3 samples. At longer times, $\tau > 50$ ns, the 6ML sample shows a much longer lifetime than what is observed for any of the other samples. TRPL data with multiple time constants are not unusual, Auger recombination rates' dependence on carrier concentration usually results in

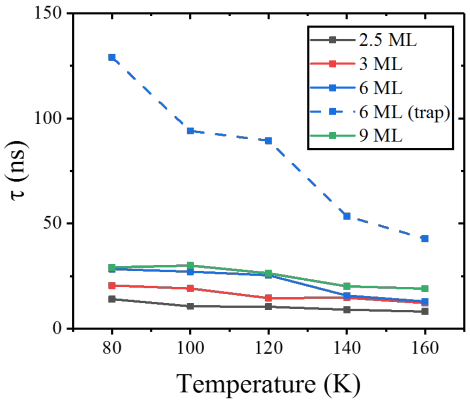

Figure 5.4: Minority carrier lifetimes are extracted from TRPL measurements and plotted as a function of temperature for (blue) 2.5 ML, (red) 3 ML, (yellow) 6 ML, and (purple) 9 ML InGaAs/InAsSb SLSs.

TRPL data, from narrow bandgap materials, with extremely fast recombination times in the first few ns, before carrier concentrations return to the low injection regime. However, the change in carrier lifetime in the 6ML sample occurs at much longer time scales than would be expected from the transition away from Auger recombination. The 6ML sample data potentially indicates the presence of trap states, which capture a certain number of excited carriers, proportional to trap density. At low times, when the traps are full, the TRPL signal is dominated by the time associated with band to band transitions in the SLS. At lower densities, however, the TRPL signal instead depends on the rate at which the traps release the captured charge carriers. A long minority carrier lifetime has been demonstrated for InAs/InAsSb superlattices due to the low active defects, and posited carrier localization, which would negatively affect the vertical carrier transport [113]. If the first portion of the 6 ML TRPL data is used to perform a signal exponential fit, as in Figure 5.4, the carrier lifetime for 6 ML (blue solid) sample falls in line with the observed behavior from the other samples. However, if the hypothesis regarding carrier trapping is correct, EBIC may offer the opportunity to observe its effect in the 6ML device's diffusion lengths.

Figure 5.4 shows the minority carrier lifetimes for each of the four samples as a function of the temperature. The carrier lifetimes extracted show a decrease in carrier lifetime as the unit cell layer thickness decreases. Note that both lifetimes from the 6 ML sample are shown, with the longer, low carrier concentration lifetime plotted as a dashed line, and the higher carrier concentration, initial lifetime plotted as the solid blue line. As the unit cell layer thickness decreases, there will be an increasing number of interfaces in the same total thickness of SLS. It is possible that the increase in interfaces could result in shorter SRH lifetimes due to defects at these interfaces, as studied in InAs/GaSb superlattice system [114].

5.3 EBIC Data

The unit cell thickness dependent $In_{0.88}Ga_{0.12}As/InAs_{0.65}Sb_{0.35}$ SLS samples are now fabricated into detectors using a UV photolithography, chemical wet etch, and metal deposition process. The layer structure of the fabricated devices is illustrated in Figure 6.1 (c) and (d). These fabricated devices are cleaved through the mesa, and mounted in the chamber of a TESCAN VEGA 3 scanning electron microscope (SEM). Note that this EBIC system is custom built in the Mid-IR Photonics group at University of Texas at Austin. In order to check the reliability of this new EBIC system, the $In_{0.80}Ga_{0.20}As/InAs_{0.65}Sb_{0.35}$ (Ga 20%) SLS, which was studied in Chapter 4, is measured in the UT Austin system to compare to results from the same device obtained at UIUC. Figure 5.5 shows the normalized EBIC data taken at the University of Illinois at Urbana-Champaign (solid) and those taken at University of Texas at Austin (dashed). The EBIC profiles obtained from the two systems show an excellent match, indicating that the UT Austin EBIC system is comparable to the system used for our previous set of samples characterized at UIUC.

The basic experimental setup is the same for the UT Austin system as for the UIUC

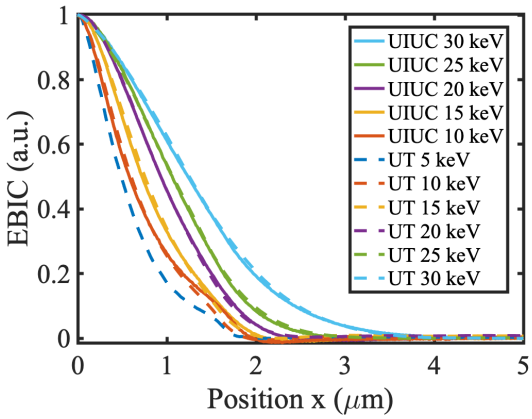

Figure 5.5: EBIC data for $In_{0.80}Ga_{0.20}As/InAs_{0.65}Sb_{0.35}$ (Ga 20%) SLS are taken from two different EBIC systems at 80 K. The data taken at UIUC is plotted in solid, and the data taken at UT-Austin is plotted in dashed.

system described in Figure 4.4. For this work, the EBIC signals are measured with beam energies of 5 keV and 10 keV at various temperatures, and the modeled EBIC profiles are fitted to extract the minority carrier diffusion length (L) and the surface recombination to diffusivity ratio (S/D). Figure 5.6 shows the experimental EBIC data (solid) and the modeled EBIC (dashed) for the SLS's as a function of the unit cell thicknesses. Figure 5.6 shows the experimental data (a) for 2.5 ML and the modeled fit with L = 2.4 μm and S/D = 3 μm^{-1}, (b) for 3 ML and the modeled fit with L = 2.6 μm and S/D = 1 μm^{-1}, (c) for 6 ML and the modeled fit with L = 0.6 μm and S/D = 1 μm^{-1}, and (d) for 9 ML and the modeled fit with L = 1.3 μm and S/D = 2.5 μm^{-1}. The EBIC model matches well with the experimental EBIC when the electron beam energy is 5 keV, while the model with 10 keV over-estimates the EBIC signal. This shows that these samples might already be in the Auger limited regime, even at the beam energy of 10 keV due to the increased carrier concentration resulting from the higher beam energies. The 6 ML SLS device shows a very good fitting for both 5 keV and 10 keV, and it suggests that this SLS is still in the low-injection regime at 10 keV. These results can possibly linked to our observations from

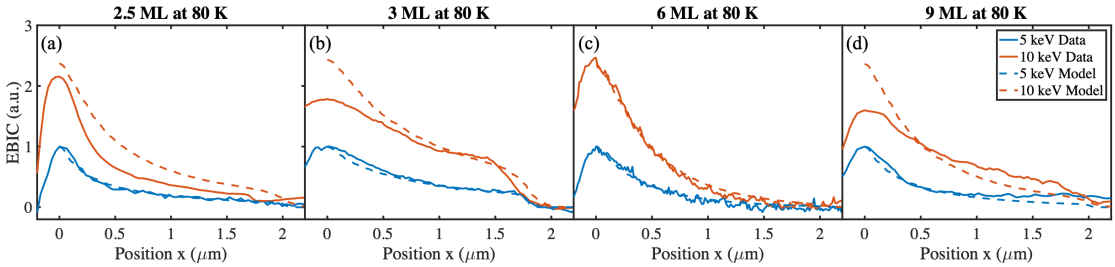

Figure 5.6: Experimental and modeled EBIC profiles for various unit cell thicknesses, (a) 2.5 ML, (b) 3 ML, (c) 6 ML, and (d) 9 ML $In_{0.88}Ga_{0.12}As/InAs_{0.65}Sb_{0.35}$ SLS detectors at 80 K with beam energies of 5 keV and 10 keV.

the TRPL data, where 6 ML sample shows longer carrier lifetime than any other samples, suggesting that the anomalously long carrier lifetime for 6 ML might be resulted from SRH process, while other samples are Auger-limited.

The EBIC measurements and the modeling process are repeated at different temperatures, and Figure 5.7 shows the minority carrier diffusion length (L) and the surface recombination velocity to diffusivity ratio (S/D) plotted as a function of the temperature. For the 2.5 ML and 3 ML SLS devices, the vertical hole diffusion lengths are similar to that of the comparable alloy, InGaAsSb, which has been reported to have a hole diffusion length of 3 μm [115]. For the 6 ML SLS, the minority carrier diffusion length is found to be shorter than that of 9 ML at low temperatures, which is the primary deviation from the unit cell thickness dependence of our devices' diffusion lengths. This anomalous extracted diffusion length can be correlated to the TRPL data from the 6 ML device, which indicates the possible existence of trap states, which would be expected to have a significant deleterious effect on the material's diffusion length. In such a situation. the carriers excited by the electron beam can be captured by trap states, which would result in a reduced diffusion current. As the temperature increases, thermal excitation will empty the trap states, promoting carriers into the SLS minibands and significantly increasing diffusion current. This is exactly what is observed in our temperature dependent diffusion length data, where at high temperatures,

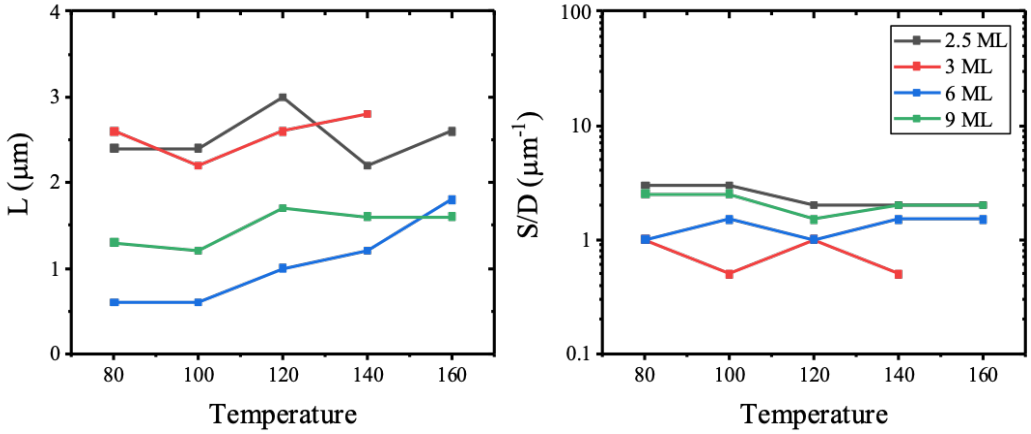

Figure 5.7: (Left) Minority carrier diffusion length (L) and (right) surface recombination velocity to diffusivity ratio (S/D) are plotted as a function of temperature for (black) 2.5 ML, (red) 3 ML, (blue) 6 ML, and (green) 9 ML $In_{0.88}Ga_{0.12}As/InAs_{0.65}Sb_{0.35}$ SLS detectors.

the 6ML device's diffusion length increases to lie between the 2.5 ML device and the 9 ML device. We currently do not have a full understanding of why the 6ML device might have significantly more trap states than the other devices, and understanding this will be the subject of further study.

In this study, the EBIC measurements are performed on the shallow etched devices, where the effective lateral diffusion length determines the effective mesa dimension [116, 117]. As shown in Figure 5.8, the shallow etched device (b) is only etched to the barrier, while the deep etched device (d) is etched to the bottom of the absorber. The EBIC data from the shallow etched devices (Figure 5.8 (a)) show sharper peaks at the barrier and absorber interface ($x = 0$), when compared to those of deep etched samples (Figure 5.8 (c)). For the shallow etched device, the parameters are extracted to be $L = 1.3\ \mu m$ and $S/D = 2.5\ \mu m^{-1}$, while the deep etched shows $L = 1.3\ \mu m$ and $S/D = 0.01\ \mu m^{-1}$. The main difference between a shallow etched and a deep etched device is that the shallow etched device shows significantly larger S/D values, though it is notable that the extracted diffusion length for

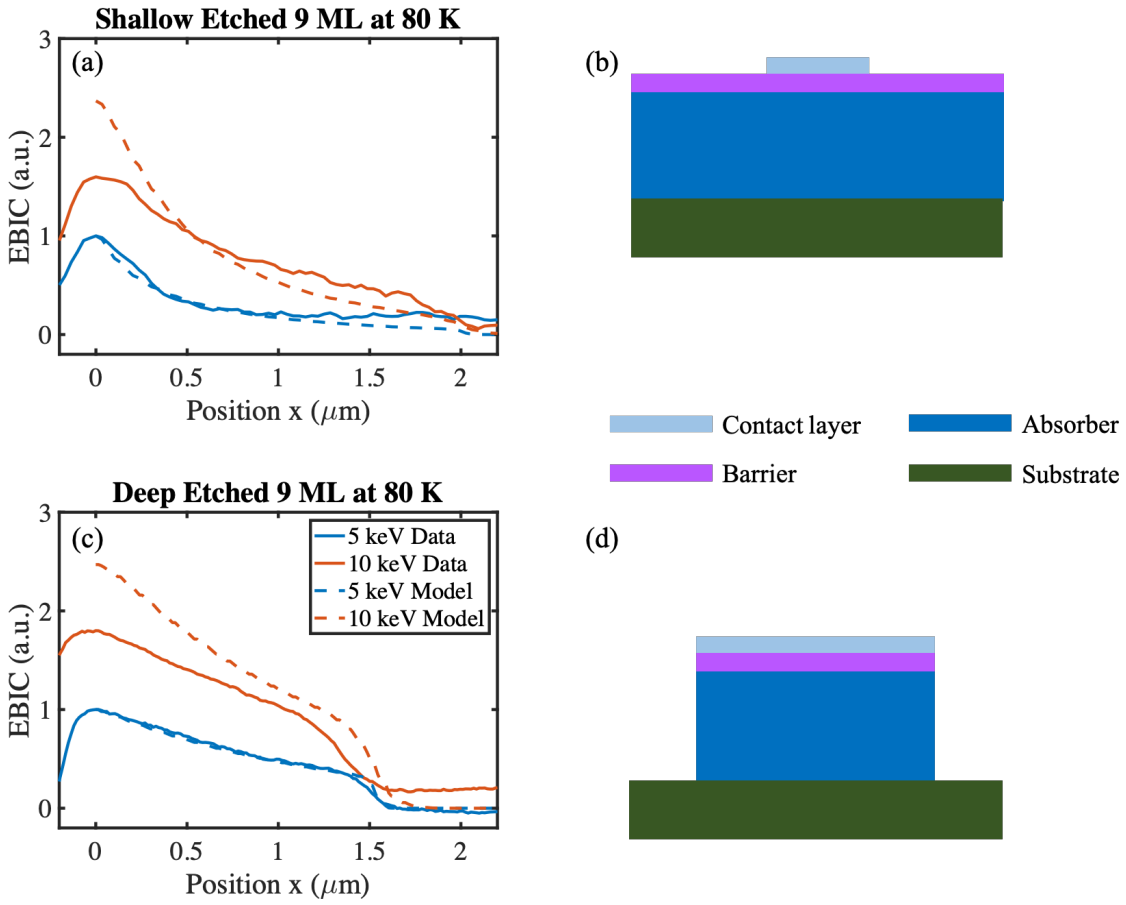

Figure 5.8: (a) The EBIC data from the shallow etched 9 ML device, and the modeled EBIC with $L = 1.3\ \mu m$ and $S/D = 2.5\ \mu m^{-1}$ are plotted. (b) The schematic of shallow etched device is illustrated. (c) The EBIC data from the deep etched and its model with $L = 1.3\ \mu m$ and $S/D = 0.01\ \mu m^{-1}$ are plotted. (d) The schematic of deep etched device is illustrated.

both device architectures is the same.

When it comes to the EBIC modeling, the shallow etched device's best fits come from using a significantly larger surface recombination current, perhaps from the exposed barrier at the top of the device. Since the EBIC model only takes into account the S/D at the cleaved surface, the extracted S/D from the shallow etched device ends up significantly larger than that for the deep etched devices, as it potentially incorporates the behavior of the top surface (at the barrier). Therefore, the shallow etched EBIC measurements result in the

effective S/D, which consists not only the surface recombination from the cleaved surface but also perhaps from the top surface (at the barrier).

5.4 Discussion

While keeping the composition of the ternary materials in the $In_{0.88}Ga_{0.12}As/InAs_{0.65}Sb_{0.35}$ SLS's studied in this chapter constant, the thickness of each layer is varied, with thicknesses of 2.5 ML, 3 ML, 6 ML, and 9 ML being studied. The calculated effective bandgap decreases as the layer thickness increases, which is experimentally verified via PL spectroscopy.

Based on the TRPL measurements, the carrier lifetime is experimentally determined to be in the 10's of ns for the samples with layer thicknesses of 2.5 ML, 3 ML, and 9 ML, while the 6 ML sample shows a more complicated lifetime behavior, with initial fast recombination times ($\tau < 50$ ns) and then significantly longer carrier lifetime at low carrier concentrations and longer times ($\tau > 50$ ns). Based on the TRPL profile for 6 ML SLS, two different carrier lifetimes can be extracted depending on where the fitting is performed. This may indicate the presence of significant number of trap states in the 6 ML SLS, which can hold carriers for a longer period of time before they escape to the SLS miniband. If we consider the carrier lifetimes that are extracted from initial response ($\tau < 50$ ns) of the TRPL data, the carrier lifetimes are found increase with increasing unit cell thickness of the SLS. As the unit cell layer thickness decreases, the more number of interfaces exists in the absorber with the same thickness, which might result in the shorter minority carrier lifetime due to the defects at the interfaces [114].

The key result from the EBIC measurements performed in this chapter is that the photodetectors with layer thickness of 2.5 ML and 3 ML demonstrate long diffusion lengths of $\sim 2.5\ \mu m$. As the unit cell thickness gets thinner, the interaction between each layer

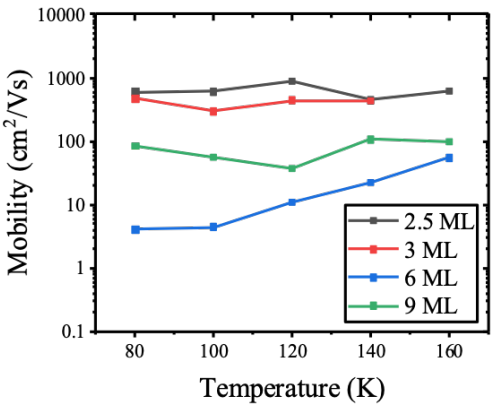

Figure 5.9: Minority carrier mobilities (μ_h) are plotted as a function of temperature for (black) 2.5 ML, (red) 3 ML, (blue) 6 ML, and (green) 9 ML $In_{0.88}Ga_{0.12}As/InAs_{0.65}Sb_{0.35}$ SLS detectors.

increases, and the short-period SL is expected to have improved vertical transport properties, as previously demonstrated in GaAs/AlGaAs superlattices using optical techniques [111]. In this work we use EBIC studies to directly extract diffusion length as a function of SL unit cell thickness in narrow bandgap materials. We demonstrate that as the unit cell layer gets thinner (< 1 nm) in InGaAs/InAsSb SLS devices, the vertical carrier diffusion length becomes similar to that of comparable alloy, AlGaAsSb [115].

Combining our EBIC and TRPL results, the vertical minority carrier (hole) mobility can be calculated. Figure 5.9 shows the vertical hole mobility of the four samples studied in this chapter as a function of increasing temperature. Due to the anomalously long carrier lifetime, possibly a result of trap states, as well as the short diffusion lengths extracted from our EBIC studies, the 6 ML sample shows very low mobility, which is almost two orders of magnitude lower, when compared to that of the 2.5 ML or 3 ML devices. Please note that the longer lifetimes of the 6 ML SLS are used to calculate the minority carrier mobilities, since the trap states need to be considered when studying mobility. As expected, the other SLS samples' data show increasing hole mobility as the unit cell layer thickness decreases.

Another interesting observation is that the mobilities of 2.5 ML, 3 ML, and 9 ML are almost independent of the temperature, while that of the 6ML increases as the temperature increases (resulting from the significant temperature dependence of the minority carrier lifetime and the extracted diffusion lengths). The vertical hole mobilities are also extracted via external quantum efficiency (EQE) measurements. Since the diffusion lengths are studied to be longer than the thickness of the absorber, the internal quantum efficiency (IQE) is found to be ~ 1 as the period gets shorter, commensurate with our results showing the shortest unit cell thickness devices (2.5 and 3 ML) having diffusion lengths greater than the absorber thickness.

Chapter 6

2D Cross-Sectional Electron Beam Induced Current

The ability to accurately extract the optical and electronic properties of SLS materials is of vital importance for the continued improvement of existing SLS absorber designs, and the accurate characterization of new SLS material systems or growth techniques. A number of characterization techniques are typically utilized to study SLS material quality or SLS detector performance, such as transmission electron microscopy (TEM), scanning tunneling microscopy (STM), x-ray diffraction (XRD), photoluminescence (PL) or absorption spectroscopy and time resolved photoluminescence (TRPL) [45, 62, 63, 67, 118, 119, 120, 121]. Such techniques typically probe either the quality of the epitaxial growth (TEM, STM, XRD) or alternatively, as discussed in previous chapters of this thesis, the optical properties of the epitaxial material (PL, TRPL, absorption spectroscopy). Extracting the electronic properties of the detector materials, however, is a slightly more challenging task. Hall measurements are often used to extract the in-plane mobility of semiconductor materials [122, 123], but the vertical mobility is different from the lateral mobility in anisotropic materials [107, 108, 109]. Moreover, for narrow band-gap materials grown on GaSb or InAs wafers (as most SLSs are), conductivity in the substrate significantly complicates the extraction of the lateral mobility of the SLS structure.

Cross-sectional electron beam induced current (EBIC) measurements offer a potentially useful approach to quantitatively study the vertical carrier transport of SLS materials [64, 124, 125, 126, 127]. In these experiments, discussed in great detail throughout the

course of this thesis, samples are often fabricated with top contacts having lateral length scales much larger than the electron hole pair generation volume, such that the detector is effectively a 1D system, and the EBIC signal across the lateral direction of the detector face can be integrated and fitted with a 1D model. Because most detectors' quantum efficiencies are directly tied to the vertical transport of their minority carriers, the extracted vertical mobility is the key parameter indicating the electronic quality of the absorber material. However, growing interest in IR focal plane arrays (FPAs), and a concurrent interest in decreasing the pixel size and pitch of these FPAs, makes the lateral transport of excited charge take on an added importance. For closely spaced pixels in an FPA, high lateral mobility could result in cross talk between adjacent pixels, to the detriment of the resulting image resolution. While the lateral mobility of (isotropic) bulk materials such as InSb and HgCdTe could reasonably be expected to mirror the materials' vertical mobility, this would not necessarily be the case for SLS materials, whose quantum-engineered band structure introduces an intrinsic anisotropy in the charge carrier dispersion.

There have been several proposed approaches to obtain the lateral diffusion length or the lateral mobility of SLS materials [107, 108, 109]. In 2011, Szmulowicz et. al. calculated both lateral and vertical mobilities of InAs/GaSb SLS materials using an interface roughness scattering (IRS) model from a rigorous solution of the Boltzmann transport equation [107]. Klipstein et. al. demonstrated a technique for measuring minority carrier lifetime and diffusion length of p-type InAs/GaSb SLS materials using dark-current and photo-current measurements combined with k·p calculations [109]. In these approaches, lateral diffusion length is either modeled from first principles or extrapolated from experimental measurements combined with theoretical models of the device band structure. Neither offers a direct measurement of minority carrier diffusion, however, without relying on bandstructure calculations of the epitaxial structure. In this chapter, the EBIC technique

is adjusted to simultaneously provide both the vertical and lateral diffusion lengths of semiconductor materials. This chapter describes the sample preparation and EBIC measurement process, as well as the EBIC modeling required to extract the anisotropic mobility. Then, the newly developed 2D-EBIC approach is applied to mid-wave IR (MWIR) SLS detectors and both vertical and lateral mobility are extracted for the material under test, showing a significant anisotropy in the experimentally determined mobilities.

6.1 Experimental Setup

The detector studied is a nBn structured InGaAs/InAsSb SLS photodetector grown by molecular beam epitaxy (MBE). From the top surface down, our device consists of a 200 nm n-type contact, 200 nm electron barrier, and 2 μm of SLS absorber material, where each period of the absorber consists of 6ML $In_{0.88}Ga_{0.12}As$ / 6ML $InAs_{0.65}Sb_{0.35}$. The detector structure is grown on a GaSb substrate following the growth of a p-type ($1\times10^{17}cm^{-3}$) GaSb contact layer, which is designed to form a tunnel junction with the SLS absorber region. The temperature-dependent PL and TRPL of the SLS material are depicted in Figure 6.1 (a) and (b), showing an effective band edge of 5.7 μm at 77 K, with lifetimes ranging from 129 ns at 77 K to 40 ns at 180 K. The sample investigated in this chapter is the same 6 ML $In_{0.88}Ga_{0.12}As$ / 6ML $InAs_{0.65}Sb_{0.35}$ SLS detector characterized in Chapter 5. Though anomalous minority carrier lifetimes and diffusion lengths were extracted from this device, and proposed to be a result of carrier trapping processes in the SLS, such effects do not detract from the primary objective of the current chapter, which is to measure the anisotropy in the minority carrier diffusion in SLS materials.

In a typical EBIC measurement, the detector device would be fabricated with wide top contacts, resulting in a uniform EBIC profile across the lateral extent of the detector cross-section. Such a device architecture, of course, is effectively 1D, and offers no oppor-

tunity to explore lateral mobility of the absorber material. In order to obtain information on the lateral transport of minority charge carriers, we altered the design of our fabricated detectors. First, we lithographically define and chemically wet etch large-area deep-etched mesas through our absorber to the bottom contact layer. The mesa width is designed to be significantly larger than the presumed lateral diffusion length of the minority charge carriers (> 100's μm). Following the large mesa etch, we lithographically define and then chemically wet-etch a smaller, shallow-etched mesa stripe in the center of the large, deep-etched mesa. For the shallow mesa, the highly-doped top contact layer is etched away from the majority of the large mesa surface, thus localizing carrier collection to this center stripe of the mesa. Finally, we perform a third lithographic patterning to define our metal contacts, and deposit Ti/Pt/Au (10 nm/15 nm/150 nm) for both top and bottom contacts. The top contact is positioned at the very center of the shallow-etched mesa located at the center of the larger mesa. The bottom contacts encircle the larger deep-etched mesa. Figure 6.1 (c) illustrates the layer structure and the (not-to-scale) cross-section of the fabricated device. Figure 6.1 (d) shows a schematic of the top view of the fabricated device. The width of the shallow-etched contact layer, W_{sh}, is about 15 μm, and the width of the metal contact, W_m, is about 8 μm.

The fabricated detector is then cleaved across the narrow top contact/shallow mesa stripe and the cleaved device is indium bonded to a custom-made EBIC mount, along with Au-coated ceramic contact pads. The top and bottom contacts are then ball-bonded to each of the ceramic contact pads. The wire-bonded sample on the EBIC mount is then placed in the vacuum chamber of a TESCAN Vega 3 scanning electron microscope (SEM), with the cleaved facet of the detector facing the electron beam of the scanning electron microscope. The contact pads are then connected to the BNC feedthroughs of the SEM vacuum chamber, and the EBIC signal from the sample is sent through a low-noise current

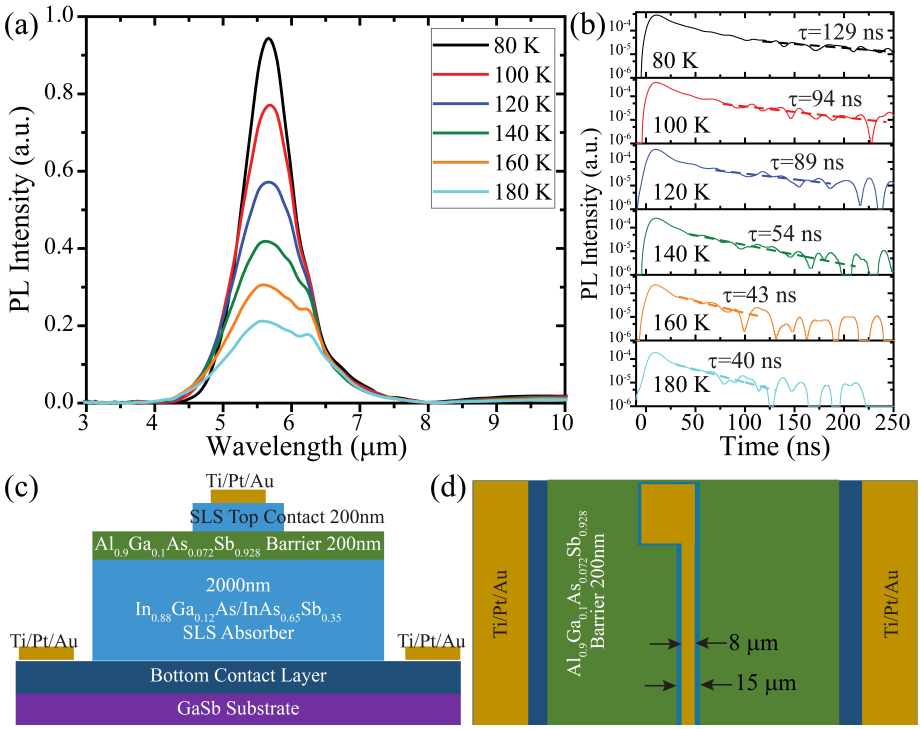

Figure 6.1: (a) Photoluminescence spectra from InGaAs/InAsSb SLS material as a function of temperature. (b) TRPL data (solid lines) from an SLS sample as a function of temperature, with exponential fits (dashed lines) showing extracted low-injection lifetimes of 129 ns at 77K down to 40 ns at 180K. (c) Cross-sectional and (d) bird-eye view illustrations of fabricated detector structure for 2D EBIC studies.

preamplifier (Stanford Research Systems SR570) into the auxiliary input of the SEM. By reading the EBIC current as a function of beam position, an EBIC image of the detector cross-section is generated. The nitrogen-cooled EBIC stage and temperature controller (Gatan, Inc.), allow for temperature-dependent EBIC images. The narrow contact and shallow etched mesa result in a lateral localization of charge collection and thus a lateral variation in EBIC signal, unlike what is observed in the more typical broad-area metal contact devices.

6.2 Experimental Cross-Sectional 2D Data on InGaAs/InAsSb SLS device

Figure 6.2 shows a representative experimental cross-sectional 2D EBIC image from the facet of the detector (whose schematic outline is superimposed on the EBIC data) at 80 K with an electron beam energy of 20 keV. The EBIC image of Figure 6.2 provides a qualitative indication that the lateral diffusion length seems to be significantly longer than the vertical diffusion length (note the different length scales in the lateral and vertical directions of the contour plot), as predicted in previously published theoretical models of SLS carrier transport. However, a full characterization of the anisotropic carrier mobility requires a mechanism to extract quantitative data for both lateral and vertical diffusion lengths. In this chapter, we present our approach to quantitative modelling of cross-sectional 2D EBIC, in order to simultaneously extract both lateral and vertical diffusion lengths. We present results from the above-described SLS detector, and demonstrate significant anisotropy in the observed carrier transport.

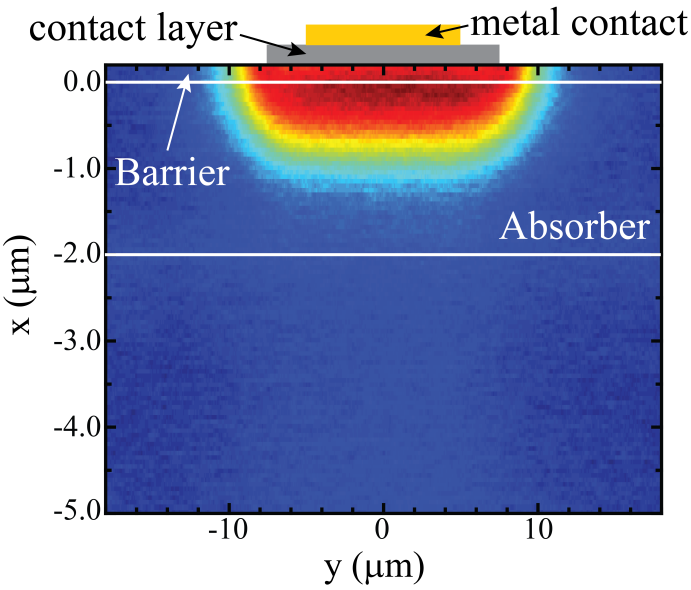

Figure 6.2: Representative experimental cross-sectional 2D-EBIC data from InGaAs / InAsSb SLS detector at 80 K with 20 keV beam voltage. Note the different x- and y-axis scales.

6.3 Cross-Sectional 2D EBIC Model

As discussed in previous work demonstrating the utility of EBIC for characterization of SLS materials [64], effective parameter extraction from EBIC data requires accurate modelling of both the position-dependent carrier generation volume and probability of collection. While previous EBIC profiles have purely been treated as 1D functions of position along growth direction, the narrow contact structures in our device result in a 2D EBIC image (a function of both x and y position), as shown in Figure 6.2. For 2D EBIC modeling, the two-dimensional probability of collection should be properly modeled, must now be expressed in the following form: $\phi_{2D}(x, y) = \int \phi(x, y, z)dz$, as we can no longer assume uniformity in the y-direction. The probability of collection in three-dimensional space, $\phi(x, y, z)$, is described below:

$$\phi(x, y, z) = [\phi(x, y, z_1), \phi(x, y, z_2), ..., \phi(x, y, z_n)]; \tag{6.1}$$

$$\phi(x, y, z_i) = \phi_{vert}(x, z_i) \cdot \phi_{lat}(x, y), \tag{6.2}$$

where $\phi_{vert}(x, z_i)$ is the vertical probability of collection, and $\phi_{lat}(x, y)$ is the lateral probability of collection. For the nBn devices, $\phi_{vert}(x, z)$, is a function of vertical hole diffusion length, $L_{h,vert}$, and the surface recombination velocity to diffusivity ratio, S_h/D_h [64] and $\phi_{lat}(x, y)$ is a function of lateral hole diffusion length, $L_{h,lat}$. When the top contact layer is infinitely long compared to the absorber thickness, $\phi_{lat}(x, y) = 1$ for any x and y, because the probability of collection becomes independent of the lateral position, which results in $\phi(x, y, z) = \phi_{vert}(x, z)$. When collection is localized to a thin strip of contact layer, as described in Figure 6.1 (c-d), however, the lateral probability of collection, $\phi_{lat}(x, y)$, must be considered. Here we model the lateral probability of collection outside of the top contact stripe as a decaying exponential function of position with decay constant given by the lateral vertical diffusion length, $L_{h,lat}$, whereas under the contact layer we assume unity lateral probability of collection, as described in the following equations:

$$\phi_{lat}(\tilde{x}, \tilde{y}) = e^{-\frac{\tilde{y}}{L_{h,lat}}}; y > \frac{W_{sh}}{2}; \tag{6.3}$$

$$\phi_{lat}(\tilde{x}, \tilde{y}) = 1; -\frac{W_{sh}}{2} < y < \frac{W_{sh}}{2}, \tag{6.4}$$

where $\tilde{y} = y - \frac{W_{sh}}{2} = 0$ is at the edge of the top contact layer, and $\tilde{x} = x + t_{barrier} = 0$ is at the top contact/barrier interface. The two-dimensional probability of collection, $\phi_{2D}(x, y) = \int \phi(x, y, z)dz$, is shown in Figure 6.3 (a). However, simply taking the product of the two probabilities of collection overestimates the collection probability, as carriers which diffuse sufficiently in the vertical collection to reach the top contact will only be collected if their simultaneous lateral diffusion is sufficient to reach the region beneath the contact before the carriers reach the surface at x=0. For this reason, we add a geometric factor, $\Omega(\theta)$, to the calculation of the collection probabilities. The $\Omega(\theta)$ term describes the relative probability of carrier collection as a function of the relative position from a

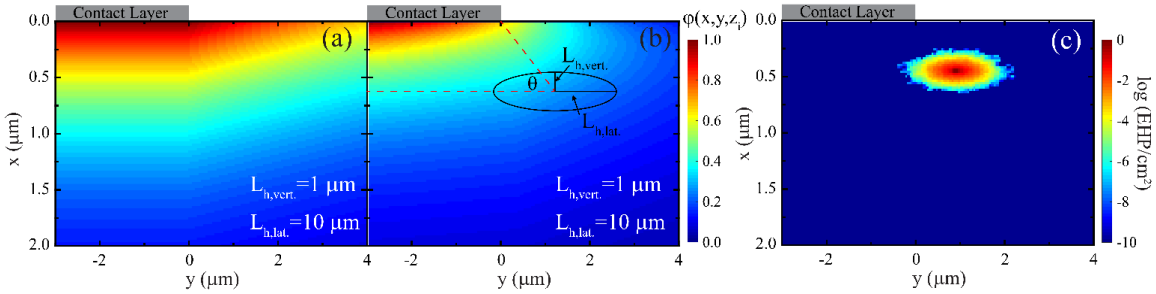

Figure 6.3: (a) The probability of collection contour plot with $L_{h,vert} = 1$ μm and $L_{h,lat} = 10$ μm (b) The adjusted probability collection taking into account the geometric correction factor, $\Omega(\theta)$. (c) The carrier generation cross sectional plot $h(x, y, z)$ for a 10 keV electron beam. Note the anisotropy of the carrier generation resulting from the layered SLS material.

generated carrier, (x_c, y_c), to the top contact layer and corresponds to the fractional area of an elliptical sector within a full ellipse described by axes with relative lengths given by the lateral and vertical diffusion lengths of the anisotropic material ($L_{h,vert} \neq L_{h,lat}$):

$$\left(\frac{\tilde{x} - x_c}{L_{h,vert}}\right)^2 + \left(\frac{\tilde{y} - y_c}{L_{h,lat}}\right)^2 = 1. \tag{6.5}$$

The fractional area of the elliptical sector is calculated as:

$$\Omega(\theta) = \frac{1}{\pi}\left[\theta - tan^{-1}\left(\frac{(b-a) * sin(2\theta)}{b + a + (b-a) * cos(2\theta)}\right)\right], \tag{6.6}$$

where $2a = 2L_{h,lat}$ is the major axis of the ellipse, $2b = 2L_{h,vert}$ is the minor axis of the ellipse, and θ is the angle from a generated carrier at (x_c, y_c) to the top contact, $\theta = tan^{-1}\left(\frac{\tilde{x}-x_c}{\tilde{y}-y_c}\right)$. The effect of including the geometric factor, $\Omega(\theta)$, on the product of the collection probabilities is shown in Figure 6.3 (b).

Next, the carrier generation volume, $h_{E_b}(x - x_o, y - y_o)$ when the electron beam is impinging at (x_o, y_o) with a beam energy of E_b, is determined numerically using CASINO Monte Carlo simulation software [86]. Because the InGaAs/InAsSb superlattice is an anisotropic material, the carrier generation volume spread in x- and y-axes are quite different,

as shown in Figure 6.3 (c). Finally, the 2D collection efficiency, $\eta_{2D}(x_o, y_o)$, can be expressed as:

$$\eta_{2D}(x_o, y_o) = \sum_{i=-\infty}^{+\infty} \sum_{j=-\infty}^{+\infty} \phi_{2D}(x_i, y_j) h_{E_b}(x - x_o, y - y_o) \Delta x_{ij}. \tag{6.7}$$

6.4 Extraction of Vertical and Lateral Diffusion Lengths

Figure 6.4 (a) shows the experimental EBIC data at 160 K with 10 keV and (d) shows the corresponding EBIC model, with the vertical hole diffusion length of 1.7 μm and the lateral hole diffusion length of 8 μm. In order to fit the experimental data with the model, both lateral and vertical line profiles at various positions are plotted as shown in Figure 6.4 (b-c) and the best combination of the vertical diffusion length, $L_{h,vert}$, and lateral diffusion length, $L_{h,lat}$, is extracted corresponding to the best fits for all line profiles.

The 2D EBIC measurements are repeated for temperatures ranging from 80K to 180K in 20K steps, and the vertical and lateral diffusion lengths are extracted for each temperature by fitting the line profiles along the lateral and vertical directions, as shown in Figure 6.4 (b) and (c). Figure 6.5 shows the extracted vertical and lateral hole diffusion lengths as a function of temperature. It also shows the vertical and lateral hole mobilities, which are calculated based on the Einstein equation, $k_B T/q = D/\mu$, and the diffusion length equation, $L = \sqrt{D\tau}$, where k_B is the Boltzmann's constant, T is the temperature, q is the charge of the electron, D is the diffusivity, μ is the mobility, L is the diffusion length, and τ is the carrier lifetime. For the 6ML InGaAs/6ML InAsSb SLS studied in this work, the lateral hole diffusion lengths are approximately 4 to 7 times longer than the vertical hole diffusion lengths. The vertical hole diffusion lengths range from 0.6 μm to 2 μm, while the lateral hole diffusion lengths range from 3 μm to 15 μm.

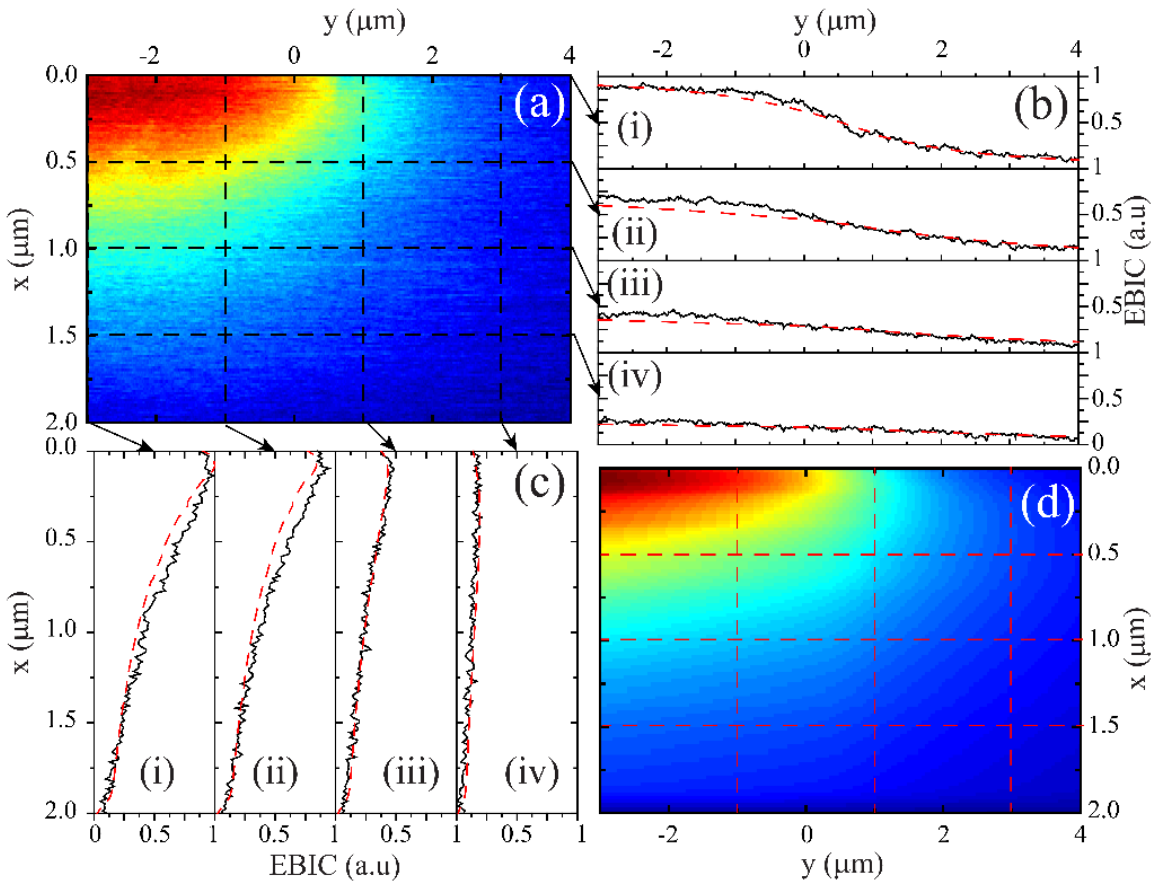

Figure 6.4: (a) Experimental 2D EBIC data from the SLS sample at 160 K with 10 keV electron beam energy, with extracted (b) lateral line profiles at positions (i) x = 0 μm, (ii) x = 0.5 μm , (iii) x = 1.0 μm, and , (iv) x = 1.5 μm. (c) vertical line profiles at positions (i) y = -3 μm, (ii) y = -1 μm , (iii) y = 1.0 μm, and , (iv) y = 3 μm. (d) Modeled 2D EBIC image with $L_{h,vert}$= 1.7 μm and $L_{h,lat}$=8 μm. Model line profiles for the same line positions as the experimental line profiles in (b) and (c) are shown as dashed red lines.

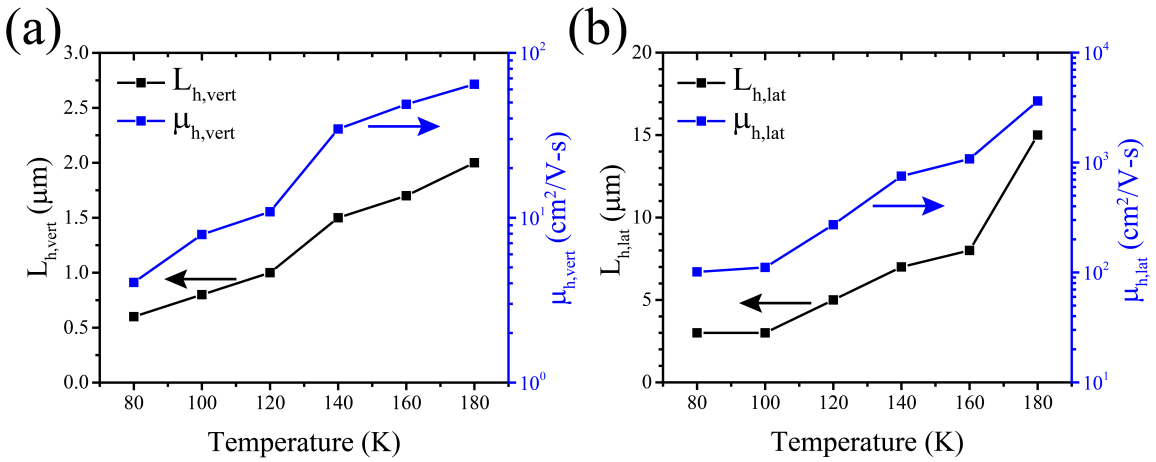

Figure 6.5: (a) The vertical hole diffusion lengths, $L_{h,vert}$, (black) and the vertical hole mobilities, $\mu_{h,vert}$, (blue) are plotted as a function of temperature, and (b) the lateral hole diffusion lengths, $L_{h,lat}$, (black) and the lateral hole mobilities, $\mu_{h,lat}$, (blue) are also plotted as a function of temperature.

6.5 Conclusion

We demonstrate the potential for electron beam induced current measurements to simultaneously extract both vertical and lateral diffusion lengths. We adjust our traditional EBIC device structure slightly, removing the lateral translational symmetry of the device cross-section by etching away the majority of the device top contact layer and using a narrow stripe contact to the remaining contact layer. Doing so results in EBIC data which has a dependence on the lateral position of the electron beam. We adjust our EBIC modeling approach so that from this EBIC data we are able to extract both lateral and vertical minority carrier diffusion length and mobility. We demonstrate the efficacy of our approach on SLS MWIR detector materials with 6ML InGaAs/6ML InAsSb SLS absorbers, extracting both the vertical and lateral hole diffusion lengths in the absorber material. We observed the vertical hole diffusion length in our material varying from 0.6 μm to 2 μm, and the lateral hole diffusion length varying from 3 μm to 15 μm, for temperatures ranging from 80 K to 180 K. With minority carrier lifetimes extracted from

time-resolved photoluminescence measurements, the vertical and lateral hole mobilities were also calculated. Our results indicate a significant anisotropy in our minority carrier mobility, in line with the predicted anisotropy from theoretical models of SLS materials [107, 108, 109]. The presented technique offers a reasonably straightforward approach to characterization of minority carrier transport in narrow bandgap materials, one which might find particular utility in new classes of IR detector materials expected to exhibit significant anisotropy. The presented approach may be of interest for designers of MWIR and LWIR FPAs, or more generally, those interested in utilizing anisotropic materials for optoelectronic applications across the visible to THz wavelength ranges.

Chapter 7

Novel Device Architectures for Long-Wavelength Photodetectors

[1]Despite the projected benefits of SLS-based detectors as discussed in Chapter 1.4.3, SLS absorber materials tend to have weak absorption and short diffusion lengths, when compared to bulk narrow band-gap materials [128], complicating the development of efficient SLS-based MWIR and LWIR detectors.

A standard measure of detector performance is external quantum efficiency (EQE), as described in Chapter 2.5, measured as the percentage of incident photons converted to an electrical signal. EQE effectively depends on three factors: the percentage of photons entering the absorber, the percentage of those photons absorbed by the detector and converted to electron hole pairs (EHPs), and finally, the fraction of the photo-excited charge carriers collected at the detector junction. While the first can be optimized by use of anti-reflection coatings, optimization of the latter two often involves trade-offs. For instance, thick absorber layers could be grown [9], maximizing the fraction of photons converted to EHPs, but with a deleterious effect on collection efficiency, as charge carriers created further from the detector junction are less likely to be collected. Moreover, EQE is far from the only metric of detector performance. The thicker absorber material results in higher dark currents, increased growth time and thus material costs, and stricter limits on growth accuracy

[1]This work has been published as "Ultra-thin enhanced-absorption long-wave infrared detectors" in Appl. Phys. Lett., vol. 112, no. 9, p. 091104, 2018. S. Wang, N. Yoon, A. Kamboj, and P. Petluru have proposed an architecture for enhanced absorption in ultra-thin SLS detectors utilizing a hybrid optical cavity design.

(due to strain accumulation). Thus, for a given SLS absorber material, there is interest in developing device architectures with strongly enhanced absorption in thin absorbing layers.

7.1 Detectors with Enhanced Absorption

There have been a number of reported efforts to enhance absorption in mid-IR detector structures limited by weak absorber layers. Type-II superlattice (T2SL) absorber material, embedded in a Fabry-Perot cavity with metallic nanoantennae patterned on one side, has demonstrated enhanced detector response with a predicted detector absorption of ~80% and demonstrated EQEs of ~40% [129]. These structures, however, require SLS thicknesses on the order of 1.8 μm and, as such, show non-unity collection efficiencies. In addition, these architectures require a substrate removal process in order to fabricate the two sides of the optical cavity. An alternative approach utilized coupling of substrate-side incident light to one-dimensional metallic gratings patterned on a T2SL detector top surface, demonstrating enhanced response by means of coupling to surface modes at the metal/T2SL interface [130]. Such work followed similar efforts using periodic metal hole arrays for enhanced response of quantum dot infrared photodetectors (QDIPs) [131] and later SLS-based detectors [132]. The use of metallic gratings (either continuous or hole arrays) has been demonstrated to offer significant enhancement, though the absorber layer thicknesses utilized remain on the order of microns. Moreover, the (typically) narrow absorption features in these detector architectures are strongly angle-, and in some cases polarization-, dependent, potentially limiting their utility for some applications.

7.2 Proposed Architectures

Here, we propose a LWIR detector architecture which allows for strongly enhanced absorption in ultra-thin SLS layers. We demonstrate >50% absorption in absorber layers of 280 nm (λ_o/35) and near 50% absorption in layers as thin as 180 nm (λ_o/50). We explore the absorption efficiency as a function of device geometry and incidence angle. Though we use a SLS design previously characterized in the literature as our absorber, integrated into an nBn detector architecture, the results presented here could be extended to a range of LWIR absorber materials and detector designs. The proposed architecture requires no substrate removal and no additional fabrication processes when compared to current LWIR detectors, while achieving strong absorption in layers thin enough to offer near 100% collection efficiency.

Highly absorbing three-layer (metal/dielectric/air) systems have been demonstrated by engineering the metal/dielectric coefficient of reflection to achieve destructive interference of reflected light with ultra-thin dielectric layers [133, 134]. This effect can be observed using doped semiconductors as the "metal" groundplane layer [133]. Unlike traditional metals, whose large, negative real permittivity gives a reflection coefficient ($r \cong -1$) effectively equivalent to that of a perfect electrical conductor (PEC), doped semiconductors offer markedly smaller real permittivity near their plasma frequencies of ω_p where $\epsilon(\omega_p) \approx 0$ [135, 136], and thus, a significant variation of reflection amplitude and phase in proximity to ω_p. Control over the complex reflection coefficient allows for strong absorption features in dielectric layers with $d \ll \lambda/4n$ (where $d \approx \lambda/4n$ corresponds to the smallest-d absorption resonance of a PEC/dielectric/air structure) [133]. In addition, unlike the case of the PEC, which effectively nulls the electric field at the PEC/dielectric interface, strong field confinement can be obtained at the "designer metal"/dielectric interface for reflection phase shifts ≈ 0.

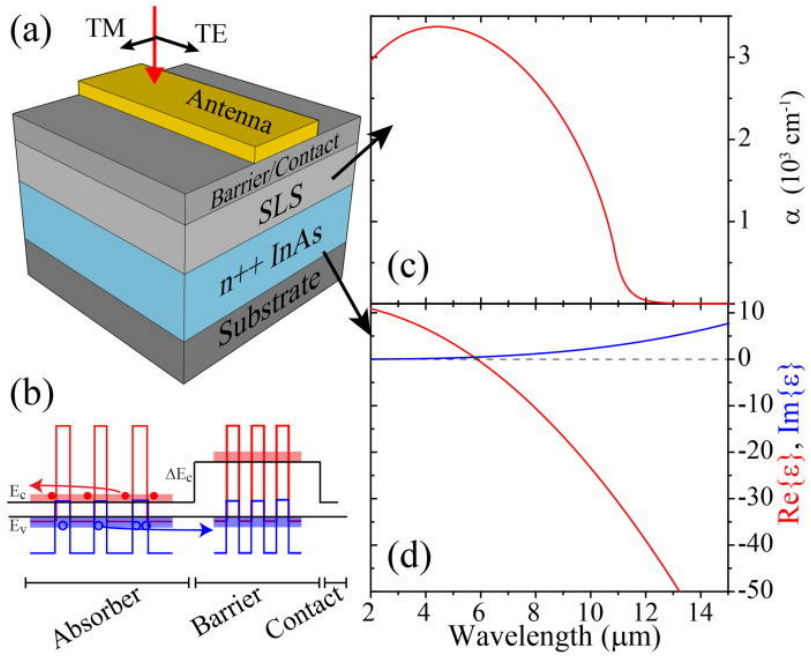

Figure 7.1: (a) Schematic of the ultra-thin enhanced absorption LWIR detector. (b) Schematic of nBn detector architecture with bandstructure schematics of the SLS absorber and barrier layers. (c) Absorption coefficient of SLS fitted using the expression developed in Ref. [8] to experimental data from Ref. [9]. (d) Drude model-calculated real and imaginary permittivity of n^{++} InAs with plasma wavelength $\lambda_p = 5.9\mu$m and $\gamma = 1.2 \times 10^{13} s^{-1}$.

The as-grown layer structure of our device is shown in Figure 7.1 (a). The structure sits on an InAs (or alternatively, GaSb) substrate and, from bottom to top, begins with 1.5 μm thick highly doped InAs (n^{++} InAs), followed by the SLS absorber layer, a SLS barrier layer, and a thin top contact layer of an n-doped material. We hold the combined barrier (145 nm) and contact layer (5 nm) thicknesses fixed in all of our simulations. Here, we use the n^{++} InAs, which has been shown to behave as a mid-IR "designer metal" [135, 136], as the monolithically integrated ground plane of our thin-film cavity, while the SLS absorber (and barrier/contact layer) serves as the cavity material.

While the use of the highly doped semiconductor groundplane will result in free-carrier absorption in the n^{++} InAs, it also allows for the demonstration of ultra-thin optical

cavities and more importantly for this work, strong absorption enhancement in cavities having weak absorption coefficients. The ultra-thin, high-index cavity results in weak angle-dependence, important for IR detector or focal plane array (FPA) applications. Additionally, the doped semiconductor ground plane provides the opportunity to control the structure's optical properties by simple tuning of doping density. The ultimate fabricated detector element includes a 50 nm thick metal (Au) antenna, with period Λ and width $w \approx \Lambda/2$, which further improves the absorption of the SLS layer and, at the same time, can serve as a top electrical contact to the device, such that no more than 500 nm of lateral diffusion is required for charge collection (well below even the experimentally obtained vertical diffusion lengths for SLS materials) [64, 137]. Though here we investigate 1D antenna arrays (metal stripes) giving polarization-dependent response, our design can be adjusted to use a 2D array of patch antennas for polarization independent response.

The SLS layer used in this work is based on a previously published binary superlattice using a single-period InAs/ GaSb (13/7 ML) design with InSb forced interfaces [61]. The absorption coefficient for this structure is described by the empirical relation derived in Ref. [8] and is plotted in Figure 7.1 (c). The n^{++} InAs is modeled as a Drude metal with $\epsilon_m(\omega) = \epsilon_\infty\left(1 - \frac{\omega_p^2}{\omega(\omega+i\gamma)}\right)$, where $\omega_p = \frac{2\pi}{\lambda_p}$, $\lambda_p = 5.9\mu$m, $\gamma = 1.2 \times 10^{13} s^{-1}$, and $\epsilon_\infty = 12.3$, values obtained from previous work demonstrating highly doped InAs as a mid-IR plasmonic material [138], and plotted in Figure 7.1 (d). The undoped barrier, consisting of an InAs/GaSb (8/8 ML) SLS, is modeled with a lossless, constant permittivity ($\epsilon = 13.3$) using a weighted average of the constituent materials. The top contact layer is modeled with the same permittivity of the SLS absorber, and the Au permittivity is taken from Ref. [139].

The optical properties of the LWIR detectors are calculated by (2D) Rigorous Coupled Wave Analysis (RCWA) [140]. RCWA simulations were run for a broad range

of the design parameter space (layer thicknesses, antenna width and cell period, incidence angle, and polarization). From these, we obtain the transmission and reflection from the entire detector structure and are able to calculate the total absorption of our system, using $A_{tot} = 1 - R - T$. The RCWA software also returns the fields in our system, from which we can obtain the absorption (α_n) in each layer n of the detector by dividing the cross-sectional area of the simulated structure into differential elements ΔS_i and using

$$\alpha_n(\lambda) = \sum_i \frac{\omega \epsilon'' |E_i(\lambda)|^2}{2} \Delta S_i, \tag{7.1}$$

where $E_i(\lambda)$ is the electric field in, and ϵ'' is the imaginary part of the material permittivity of, the ith element of layer n, for incident wavelength λ and angular frequency $\omega = 2\pi c/\lambda$. The normalized absorption of each layer n can then be written as

$$A_n(\lambda) = A_{tot}(\lambda) \frac{a_n(\lambda)}{\sum_n a_n(\lambda)}. \tag{7.2}$$

The absorption in each material layer of our detector structure can thus be determined, and the detector design process looks to optimize absorption in the SLS absorber layer.

In order to understand the extent of the absorption enhancement, as well as the enhancement mechanisms, we first simulate 4 representative structures, each based on the same basic nBn structure using a 180 nm thick absorber SLS layer (a-SLS) and a 150 nm thick barrier/contact layer. The structures simulated, shown in Figures 7.2 (a)-(d), can be described as the nBn structure (1) on an unintentionally doped (UID) InAs substrate, (2) on the UID substrate with an Au antenna, (3) on an n^{++} InAs groundplane, and finally, (4) on an n^{++} InAs groundplane with the Au antenna. Figures 7.2 (e) and (g) show the total (TE- and TM-polarized) absorption of the structures, while Figures 7.2 (f) and (h) show only the (TE- and TM-polarized) a-SLS absorption. For the stand-alone nBn detector, the a-SLS absorption remains quite weak (<3%) across the entire LWIR, a result of the

ultra-thin and inherently weakly absorbing a-SLS layer. The addition of an Au antenna does little to improve this, having little effect on both TE and TM absorption in our system. When we add the n^{++} InAs layer under the nBn [Figure 7.2 (c)], a strong absorption peak appears at $\lambda \approx 8.7\mu$m for both TE and TM polarized light. This absorption occurs both in the n^{++} InAs, due to free carrier absorption [dashed green line in Figure 7.2 (f)], and in the a-SLS layer, where a peak absorption of $\approx 29\%$ is observed. This peak reflects the enhanced absorption resulting from the ultra-thin cavity achieved by control of the reflection phase shift at the n^{++} InAs/nBn interface. The field enhancement at this interface is clearly observed in the $|H_y|$ field plot in Figure 7.2 (i).

The introduction of the metal antenna to the structure with the n^{++} InAs ground plane results in a significant enhancement in the TM, and a near-quenching of the TE, a-SLS absorption. The antenna can be thought of as introducing a frequency-dependent reflection coefficient to the nBn/air interface, which, for the proper antenna width, strengthens the destructive interference maximum and thus enhances field confinement and absorption in the a-SLS layer, as shown in the $|H_y|$ field plot in Figure 7.2 (j). As can be seen in Figure 7.2 (g) (red line), near perfect total absorption is achieved, on resonance ($\lambda_o = 9.15\mu$m), for this architecture, indicating that the n^{++} InAs and Au antenna are absorbing slightly more than 50% of the incident light. The free carrier absorption in the n^{++} InAs is shown by the dashed red line in Figure 7.2 (h). Though there is strong absorption in the n^{++} InAs groundplane, we are nonetheless able to obtain $\approx 47\%$ absorption in a 180 nm ($\lambda_o/50$) a-SLS layer, an 18 $\times$ absorption enhancement compared to the absorption in the thin nBn detector without the doped semiconductor ground plane and Au antenna. It bears noting that even though we observe our strongest absorption enhancement on resonance, our detector architecture provides enhancement over the stand-alone nBn across the entire LWIR (for TM polarized light). The 1D grating array of antennas provides a strong polarization

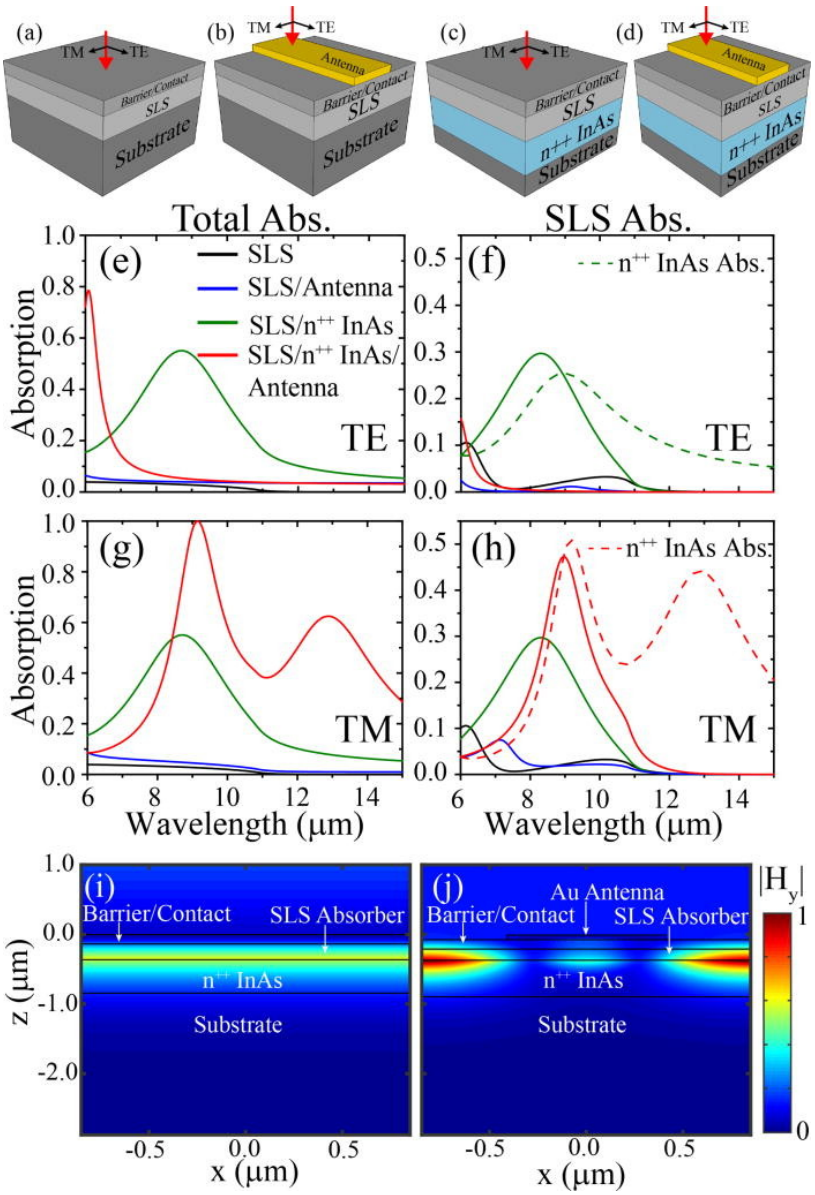

Figure 7.2: (a)-(d) Schematics of the four nBn detector architectures investigated. TE-polarized (e) total and (f) a-SLS and TM-polarized (g) total and (h) a-SLS absorption for each of the four architectures. Absorption in the n^{++} groundplane for the structures in (c) and (d) is shown as dashed lines in (f) and (g). $|H_y|$ field plots, for normal incidence light, for the architectures having (i) nBn on n^{++} InAs ($\lambda = 8.5\mu$m) and (j) nBn on n^{++} InAs with the Au antenna ($\lambda = 9\mu$m).

dependent absorption, with a TM/TE absorption ratio of $\approx$ 200 on resonance, offering the opportunity for highly polarization-selective detection with the proposed architecture. Alternatively, a 2D array of Au patches would provide strong, polarization-independent, absorption enhancement, the subject of ongoing investigation.

We can adjust our ultra-thin hybrid optical cavity LWIR detector design in order to control the spectral position of peak absorption across a range of LWIR wavelengths. In Figure 7.3 (a), we show the simulated TM-absorption from our hybrid optical cavity design for a range of a-SLS thicknesses, holding the barrier/contact layer thickness constant (150 nm) and adjusting Λ and w to maximize the peak absorption for each a-SLS thickness. For comparison, we show the simulated a-SLS absorption from a bare nBn detector structure as a function of a-SLS thickness in Figure 7.3 (b) (note the difference in scale between the two contour plots). As expected, the a-SLS absorption in our detector architecture dwarfs that in the bare nBn across all thicknesses. In addition, we show that our absorption resonance can be tuned from 8.7 to 10.6 μm, with peak a-SLS absorption of over 50% observed at $\Lambda \approx 9.9$ μm for an a-SLS thickness of 280 nm.

Lastly, we investigate the angular dependence of our 180 nm thick detector design, in comparison to a bare nBn detector (thickness 5.8 μm) designed to provide equivalent a-SLS absorption ($\approx$50%) to our proposed detector, on resonance. Absorption enhancement schemes relying on coupling of incident light into propagating surface modes will result in a strong angle dependence of the enhancement, due to momentum matching requirements. Our proposed detector design offers largely angle-independent absorption spectra. As shown in Figure 7.4, absorption is essentially unchanged from 0° to 35°, and less than a 10% decrease in a-SLS absorption is observed for angles as large as 60°, with almost no change in the general form of the absorption spectrum.

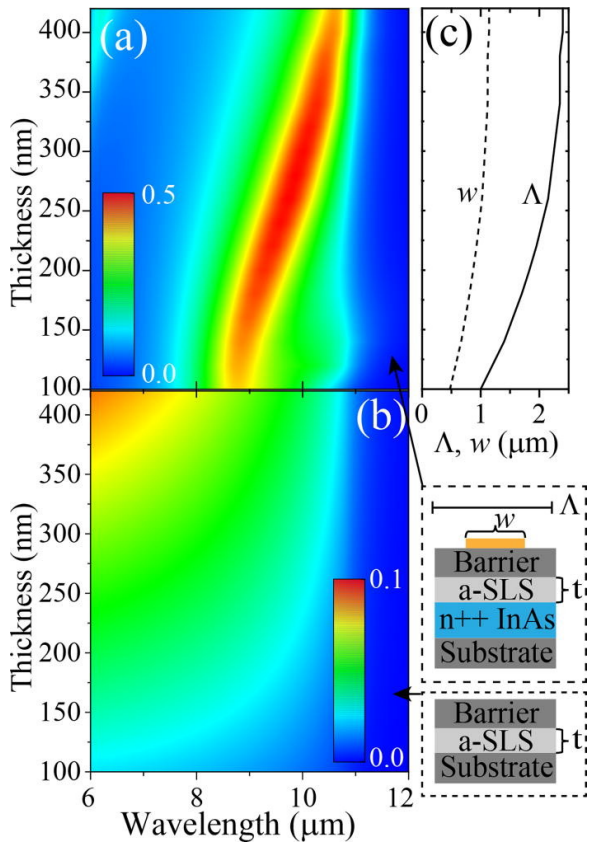

Figure 7.3: SLS absorption for an nBn detector (a) embedded in the proposed hybrid optical cavity and (b) on an undoped substrate, unpatterned, as a function of a-SLS thickness. Note $\times 5$ difference in color scale between (a) and (b). (c) Antenna width (w) and periodicity (Λ) used to optimize absorption in (a).

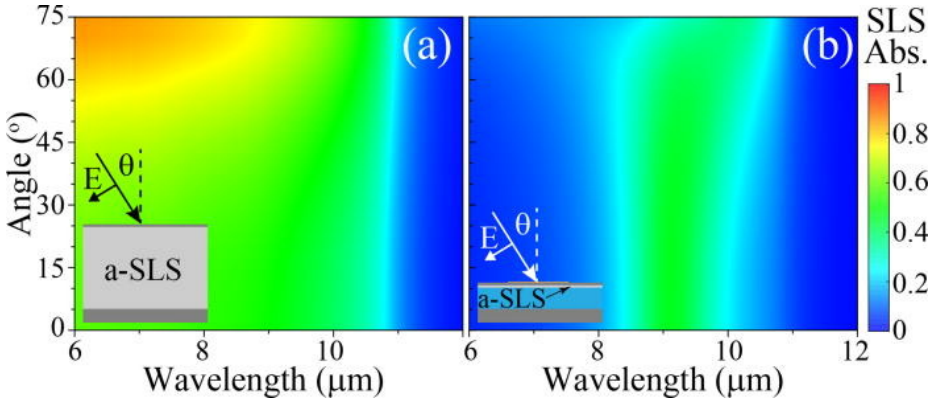

Figure 7.4: SLS TM-polarized absorption as a function of incidence angle for (a) a 5.8 μm thick SLS on an undoped InAs substrate and (b) our hybrid optical cavity SLS (a-SLS thickness of 180 nm).

7.3 Conclusion

we demonstrate a proposed architecture for enhanced absorption in ultra-thin type-II superlattice detectors utilizing a hybrid optical cavity design. By introducing an n^{++} InAs ground plane, with a plasma wavelength in the mid-IR, we are able to control the complex reflection coefficient at the n^{++} InAs/SLS interface, allowing for the strong confinement of incident light in our ultra-thin a-SLS layer. The addition of the metal antenna on the top surface of our device allows for further control of the optical properties of our detectors, giving near perfect total absorption and additional absorption enhancement in our a-SLS layer. Using our hybrid optical cavity, we demonstrate the potential for near 50% detector absorption in a-SLS layers with thicknesses of approximately $\lambda_o/50$. By adjusting the device geometry, we demonstrate tuning of the absorption resonance from $\lambda = 8.7\mu$m to $\lambda = 10.6\mu$m with little to no degradation in the a-SLS absorption. We also show the absorption enhancement mechanism to be largely angle-independent for incidence angles up to 60°. The device architecture presented offers the potential for strong polarization-selectivity, ultra-thin, high efficiency detectors with minimized growth costs and relaxed

design parameters.

Chapter 8

Conclusions and Future Work

Two sets of (Ga-dependent and unit cell thickness-dependent) InGaAs/InAsSb SLS materials have been characterized via electron beam induced current (EBIC) as well as time-resolved photoluminesence (TRPL) measurements. The results from these studies provide valuable insights into the carrier dynamics of anisotropic quantum-engineered mid-IR absorber materials for IR detector applications. First, our results show increasing vertical mobility for minority charge carriers as the composition of Ga increases in InGaAs/InAsSb T2SL materials. Our second study, looking to understand the effects of unit cell thickness on the performance of mid-wave IR T2SL absorbers, demonstrates increasing diffusion lengths for decreasing unit cell thickneses in InGaAs/InAsSb superlattices. With a deeper understanding of the InGaAs/InAsSb T2SL material system, these results provide insights into the development and design of next generation mid wave IR detectors.

In addition, we describe and demonstrate a new EBIC modeling method, designed to reduce the uncertainty of the extracted parameters (the diffusion lengths and the surface recombination velocity). This work opens the door to deeper approaches to EBIC measurements where the beam energy is used as a tunable parameter for better understanding carrier concentration-based transport in mid-IR optoelectronic materials. By controlling the beam energies impinging on the device under study, the EBIC technique shows a potential to characterize device properties as a function of injection regime.

We also describe new avenues for extending the utility of the EBIC technique,

demonstrating a new approach, two dimensional cross-sectional EBIC (2D-EBIC), developed to study both the lateral and the vertical diffusion lengths in IR detector materials. This technique shows great potential for understanding semiconductor materials, especially anisotropic materials such as strained-layer superlattices. The first demonstration of the cross-sectional 2D-EBIC technique has been applied to nBn detectors utilizing 6ML $In_{0.88}Ga_{0.12}As$ / 6ML $InAs_{0.65}Sb_{0.35}$ absorbers, and the lateral diffusion length is determined to be 5 to 7 times longer than the vertical diffusion length. With a continued reduction in the pixel spacing of T2SL FPAs, cross sectional 2D-EBIC may prove to be a powerful technique for the study of both lateral and vertical diffusion characteristics in infrared semiconductor materials.

Due to the experimentally studied short diffusion length of T2SL materials, there has been a great effort to enhance the light absorption in the absorbing materials in the T2SL-based infrared photodetectors. In this dissertation we provide a potential detector architecture for enhanced absorption in ultra-thin T2SL detectors. The highly doped semiconductors have been utilized to create an optical cavity in a thin absorber. With realistic material properties, near 50% absorption in a λ_o/50-thick absorber has been predicted. This proposed detector architecture offers a great opportunity for the development of high efficiency photodetectors with minimal growth and fabrication costs.

There remains much to be investigated for the InGaAs/InAsSb SLS materials, and there is also much to be explored in the continuing development of EBIC measurements. New materials, and new methods for interrogating these materials, offer opportunities for the continued development and improvement of infrared detectors and infrared optoelectronic materials. The results and techniques proposed and demonstrated in this dissertation can provide direction for the further improvement of infrared material growth and material development. In addition, there exists a wide range of opportunities for integration of highly

doped semiconductors with infrared optoelectronic devices, including infrared photodetectors. Continued study of these materials and concepts can be leveraged to improve the field of infrared optoelectronic materials and devices.

Appendices

Appendix A

Fabrication and Sample Preparation for EBIC

Steps	Top and side view	Fab process	Notes
1.		Clean wafer	a. Acetone soak for 5 mins b. IPA soak for 5 mins c. Rinse with DI water d. N_2 dry
2.		Photoresist	a. Dehydration bake at 120 °C for 5 mins b. Spin AZ-5214 at 4500 rpm for 1 min c. Prebake at 90 °C for 1 min
3.		Exposure & Develop	a. Pattern exposure for 7 sec (MA6, 7.5mW) b. Post bake at 115 °C for 2 mins c. Flood exposure for 17 sec (MA6, 7.5mW) d. Develop for 55 sec (MF-26A)
4.		Wet etch	a. Citric acid monohydrate: DI (1 g: 0.83 ml) stir for 4 hrs+ b. Citric acid: H_2O_2: H_3PO_4: DI (55: 5: 3: 220) stir for 1 hr+ c. Etch the patterned region
5.		Strip PR	a. Acetone soak for 5 mins b. IPA soak for 5 mins c. Rinse with DI water d. N_2 dry

Steps	Top and side view	Fab process	Notes
6.		Photoresist	a. Dehydration bake at 120 °C for 5 mins b. Spin AZ-5214 at 4500 rpm for 1 min c. Prebake at 90 °C for 1 min
7.		Exposure & Develop	a. Pattern exposure for 7 sec (MA6, 7.5mW) b. Post bake at 115 °C for 2 mins c. Flood exposure for 17 sec (MA6, 7.5mW) d. Develop for 55 sec (MF-26A)
8.		Metal Deposition	a. Native oxide removal for 1 min in HCl: DI (1: 10) b. Deposit metal Ti (150 Å)/ Pt (450 Å)/ Au (2400 Å)
9.		Metal liftoff	a. Acetone soak until PR is removed b. IPA soak for 5 mins c. Rinse with DI water d. N_2 dry

Appendix B

List of Acronyms

CBIRD - complementary barrier infrared detector

EBIC - electron beam induced current

EHP - electron-hole-pair

EM - electromagnetic

EQE - external quantum efficiency

FIR - far infrared (15 μm - 100 μm)

FPA - focal plane array

FTIR - Fourier transform infrared

IR - infrared

IRS - interface roughness scattering

LBIC - laser beam induced current

LWIR - long-wave infrared (8 μm - 15 μm)

MWIR - mid-wave infrared (3 μm - 8 μm)

MBE - molecular beam epitaxy

MCT - mercury cadmium telluride (HgCdTe)

ML - monolayer

NIR - near infrared (750 nm - 1 μm)

PL - photoluminescence

SEM - scanning electron microscope

SL - superlattice

SLS - strained-layer superlattice

SRH - Shockley-Read-Hall

SSE - sum of squared error

STM - scanning tunneling microscopy

SWIR - short-wave infrared (1 μm - 3 μm)

TEM - transmission electron microscopy

TRPL - time-resolved photoluminescence

T2SL - type-II superlattice

THz - terahertz

QWIP - quantum well infrared photodetector

QDIP - quantum dot infrared photodetector

XBIC - x-ray beam induced current

XRD - x-ray diffraction

Bibliography

[1] G. Ariyawansa, C. J. Reyner, E. H. Steenbergen, J. M. Duran, J. D. Reding, J. E. Scheihing, H. R. Bourassa, B. L. Liang, and D. L. Huffaker, "InGaAs/InAsSb strained layer superlattices for mid-wave infrared detectors," *Appl. Phys. Lett.*, vol. 108, no. 2, p. 022106, 2016.

[2] "Atmospheric Transmittance," https://en.wikipedia.org/wiki/Infrared_window#/media/File:Atmosfaerisk_spredning.png.

[3] "Molecular Absorption," https://www.photonics.com/images/Web/Articles/2016/10/24/Pilot_Chemical.jpg.

[4] D. R. Rhiger, "Performance Comparison of Long-Wavelength Infrared Type II Superlattice Devices with HgCdTe," *J. Electron. Mater.*, vol. 40, no. 8, p. 1815, 2011.

[5] E. A. Plis, "InAs/GaSb Type-II Superlattice Detectors," *Adv. Electron.*, vol. 2014, p. 1, 2014.

[6] "Laser Interferometers," https://www.muelaner.com/laser-interferometers/.

[7] D. Zuo, R. Liu, J. Mabon, Z.-Y. He, S. Liu, Y.-H. Zhang, E. A. Kadlec, B. Olson, E. A. Shaner, and D. Wasserman, "Diffusion Characterization Using Electron Beam Induced Current and Time-Resolved Photoluminescence of InAs/InAsSb Type-II Superlattices," *CLEO conference presentation*, 2015.

[8] G. Ariyawansa, M. Grupen, J. M. Duran, J. E. Scheihing, T. R. Nelson, and M. T. Eismann, "Design and modeling of InAs/GaSb type II superlattice based dual-band infrared detectors," *J. Appl. Phys.*, vol. 111, no. 7, p. 073107, 2012.

[9] B.-M. Nguyen, D. Hoffman, Y. Wei, P.-Y. Delaunay, A. Hood, and M. Razeghi, "Very high quantum efficiency in type-II superlattice photodiode with cutoff of 12 μm," *Appl. Phys. Lett.*, vol. 90, no. 23, p. 231108, 2007.

[10] B. Stuart, *Infrared Spectroscopy: Fundamentals and Applications*. Wiley, 2004.

[11] W. Herschel, "XIV. Experiments on the refrangibility of the invisible rays of the sun," *Phil. Trans. R. Soc.*, vol. 90, p. 284, 1800.

[12] S. P. Langley, "The bolometer and radiant energy," *Proc. Am. Acad. Arts Sci.*, vol. 8, p. 343, 1881.

[13] C. Kittel, *Introduction to Solid State Physics*, 1986.

[14] S. Maimon and G. W. Wicks, "nBn detector, an infrared detector with reduced dark current and higher operating temperature," *Appl. Phys. Lett*, vol. 89, no. 15, p. 151109, 2006.

[15] D. Z.-Y. Ting, C. J. Hill, A. Soibel, S. A. Keo, J. M. Mumolo, J. Nguyen, and S. D. Gunapala, "A high-performance long wavelength superlattice complementary barrier infrared detector," *Appl. Phys. Lett*, vol. 95, no. 2, p. 023508, 2009.

[16] I. Vurgaftman, E. H. Aifer, C. L. Canedy, J. G. Tischler, J. R. Meyer, J. H. Warner, E. M. Jackson, G. Hildebrandt, and G. J. Sullivan, "Graded band gap for dark-current suppression in long-wave infrared W-structured type-II superlattice photodiodes," *Appl. Phys. Lett*, vol. 89, no. 12, p. 121114, 2006.

[17] B.-M. Nguyen, S. Bogdanov, S. A. Pour, and M. Razeghi, "Minority electron unipolar photodetectors based on type II InAs/GaSb/AlSb superlattices for very long wavelength infrared detection," *Appl. Phys. Lett*, vol. 95, no. 18, p. 183502, 2009.

[18] D. L. Smith, T. C. McGill, and J. N. Schulman, "Advantages of the HgTe-CdTe

superlattice as an infrared detector material," *Appl. Phys. Lett.*, vol. 43, no. 2, p. 180, 1983.

[19] Y. Wei, A. Gin, M. Razeghi, and G. J. Brown, "Advanced InAs/GaSb superlattice photovoltaic detectors for very long wavelength infrared applications," *Appl. Phys. Lett.*, vol. 80, no. 18, p. 3262, 2002.

[20] S. L. Chuang, *Physics of Photonic Devices*. Wiley, 2009.

[21] B. G. Streetman and S. K. Banerjee, *Solid State Electronic Devices*. Prentice Hall, 2005.

[22] A. Rogalski, *Infrared Detectors*. CRC Press, 2010.

[23] R. Hui and M. O'Sullivan, *Fiber Optic Measurement Techniques*. Academic Press, 2009.

[24] P. D. Grant, R. Dudek, M. Buchanan, L. Wolfson, and H. Liu, "An ultra fast quantum well infrared photodetector," *Appl. Phys. Lett.*, vol. 47, p. 144, 2005.

[25] S. Steinkogler, H. Schneider, R. Rehm, M. Walther, and P. Koidl, "Electron transport studies on $In_{0.30}Ga_{0.70}As$/GaAs-quantum-well infrared photodetectors using time-resolved photocurrent measurements," *Appl. Phys. Lett.*, vol. 81, no. 18, p. 3401, 2002.

[26] S. Steinkogler, H. Schneider, M. Walther, and P. Koidl, "Determination of the electron capture time in quantum-well infrared photodetectors using time-resolved photocurrent measurements," *Appl. Phys. Lett.*, vol. 82, no. 22, p. 3925, 2003.

[27] L. Esaki and R. Tsu, "Superlattice and Negative Differential Conductivity in Semiconductors," *IBM J. Res. Dev.*, vol. 14, no. 1, p. 61, 1970.

[28] G. A. Sai-Halasz, R. Tsu, and L. Esaki, "A new semiconductor superlattice," *Appl. Phys. Lett.*, vol. 30, no. 12, p. 651, 1977.

[29] G. A. Sai-Halasz, L. Esaki, and W. A. Harrison, "InAs-GaSb superlattice energy structure and its semiconductor-semimetal transition," *Phys. Rev. B*, vol. 18, no. 6, p. 2812, 1978.

[30] H. Sakaki, L. L. Chang, G. A. Sai-Halasz, C. A. Chang, and L. Esaki, "Two-dimensional electronic structure in InAs-GaSb superlattices," *Solid State Commun.*, vol. 26, no. 9, p. 589, 1978.

[31] Y.-C. Chang and J. N. Schulman, "Interband optical transitions in GaAs-$Ga_{1-x}Al_xAs$ and InAs-GaSb superlattices," *Phys. Rev. B*, vol. 31, no. 4, p. 2069, 1985.

[32] J. N. Schulman and T. C. McGill, "The CdTe/HgTe superlattice: Proposal for a new infrared material," *Appl. Phys. Lett.*, vol. 34, no. 10, p. 663, 1979.

[33] M. E. Flatté and C. H. Grein, "Theory and modeling of type-II strained-layer superlattice detectors," *Proc. SPIE*, vol. 7222, p. 72220Q, 2009.

[34] C. H. Grein and H. Ehrenreich, "Improvement of infrared detector performance in carrier depleted strained layer type II superlattices," *J. Appl. Phys.*, vol. 82, no. 12, p. 6365, 1997.

[35] C. H. Grein, W. H. Lau, T. L. Harbert, and M. E. Flatté, "Modeling of Very Long Infrared Wavelength InAs/GaInSb Strained Layer Superlattice Detectors," *J. Appl. Phys.*, vol. 4795, p. 39, 2002.

[36] C. H. Grein, P. M. Young, and H. Ehrenreich, "Minority carrier lifetimes in ideal InGaSb/InAs superlattices," *Appl. Phys. Lett.*, vol. 61, no. 24, p. 2905, 1992.

[37] C. H. Grein, P. M. Young, M. E. Flatté, and H. Ehrenreich, "Long wavelength

InAs/InGaSb infrared detectors: Optimization of carrier lifetimes," *J. Appl. Phys.*, vol. 78, no. 12, p. 7143, 1995.

[38] G. Ariyawansa, E. Steenbergen, L. J. Bissell, J. M. Duran, J. E. Scheihing, and M. T. Eismann, "Absorption characteristics of mid-wave infrared type-II superlattices," *Proc. SPIE*, vol. 9070, p. 90701J, 2014.

[39] H. Katayama, T. Takekawa, M. Kimata, H. Inada, and Y. Iguchi, "Measurement of absorption and external quantum efficiency of an InAs/GaSb Type II superlattice," *Infrared Phys. Technol.*, vol. 70, p. 53, 2015.

[40] G. C. Osbourn, "InAsSb strained-layer superlattices for long wavelength detector applications," *J. Vac. Sci. Technol. B*, vol. 2, no. 2, p. 176, 1984.

[41] G. S. Lee, Y. Lo, Y. F. Lin, S. M. Bedair, and W. D. Laidig, "Growth of $InAs_{1-x}Sbx$ (0<x<1) and InSb-InAsSb superlattices by molecular beam epitaxy," *Appl. Phys. Lett.*, vol. 47, no. 11, p. 1219, 1985.

[42] D. L. Smith and C. Mailhiot, "Proposal for strained type II superlattice infrared detectors," *J. Appl. Phys.*, vol. 62, no. 6, p. 2545, 1987.

[43] S. R. Kurtz, L. R. Dawson, T. E. Zipperian, and S. R. Lee, "Demonstration of an InAsSb strained-layer superlattice photodiode," *Appl. Phys. Lett.*, vol. 52, no. 19, p. 1581, 1988.

[44] S. R. Kurtz, "Development of Infrared Detectors Based on Type II, InAsSb Strained-Layer Superlattices," *MRS Proceedings*, vol. 216, p. 163, 1990.

[45] R. H. Miles, D. H. Chow, J. N. Schulman, and T. C. McGill, "Infrared optical characterization of $InAs/Ga_{1-x}In_xSb$ superlattices," *Appl. Phys. Lett.*, vol. 57, no. 8, p. 801, 1990.

[46] D. H. Chow, R. H. Miles, J. N. Schulman, D. A. Collins, and T. C. McGill, "Type II superlattices for infrared detectors and devices," *Semicond. Sci. Technol.*, vol. 6, no. 12C, p. C47, 1991.

[47] C. A. Hoffman, J. R. Meyer, E. R. Youngdale, F. J. Bartoli, and R. H. Miles, "Interface roughness scattering in semiconducting and semimetallic InAs/$Ga_{1-x}In_xSb$ superlattices," *Appl. Phys. Lett.*, vol. 63, no. 16, p. 2210, 1993.

[48] R. M. Feenstra, D. A. Collins, D. Z.-Y. Ting, M. W. Wang, and T. C. McGill, "Scanning tunneling microscopy of InAs/GaSb superlattices: Subbands, interface roughness, and interface asymmetry," *J. Vac. Sci. Technol. B*, vol. 12, no. 4, p. 2592, 1994.

[49] C. M. Ciesla, B. N. Murdin, C. R. Pidgeon, R. A. Stradling, C. C. Phillips, M. Livingstone, I. Galbraith, D. A. Jaroszynski, C. J. G. M. Langerak, P. J. P. Tang, and M. J. Pullin, "Suppression of Auger recombination in arsenic-rich $InAs_{1-x}Sb_x$ strained layer superlattices," *J. Appl. Phys.*, vol. 80, no. 5, p. 2994, 1996.

[50] L. Bürkle, F. Fuchs, J. Schmitz, and W. Pletschen, "Control of the residual doping of InAs/(GaIn)Sb infrared superlattices," *Appl. Phys. Lett.*, vol. 77, no. 11, p. 1659, 2000.

[51] Y. Wei, A. Gin, M. Razeghi, and G. J. Brown, "Type II InAs/GaSb superlattice photovoltaic detectors with cutoff wavelength approaching 32 μm," *Appl. Phys. Lett.*, vol. 81, no. 19, p. 3675, 2002.

[52] W. A. Cabanski, K. Eberhardt, W. Rode, J. C. Wendler, J. Ziegler, J. Fleissner, F. Fuchs, R. H. Rehm, J. Schmitz, H. Schneider, and M. Walther, "Third-generation focal plane array IR detection modules and applications," *Proc. SPIE*, Orlando, Florida, 2004.

[53] A. Gin, Y. Wei, A. Hood, A. Bajowala, V. Yazdanpanah, M. Razeghi, and M. Tidrow, "Ammonium sulfide passivation of Type-II InAs/GaSb superlattice photodiodes," *Appl. Phys. Lett.*, vol. 84, no. 12, p. 2037, 2004.

[54] R. Rehm, M. Walther, J. Schmitz, J. Fleissner, F. Fuchs, W. Cabanski, and J. Ziegler, "InAs/(GaIn)Sb short-period superlattices for focal plane arrays," *Proc. SPIE*, vol. 5783, p. 123, 2005.

[55] P.-W. Liu, G. Tsai, H. H. Lin, A. Krier, Q. D. Zhuang, and M. Stone, "Photoluminescence and bowing parameters of InAsSb/InAs multiple quantum wells grown by molecular beam epitaxy," *Appl. Phys. Lett.*, vol. 89, no. 20, p. 201115, 2006.

[56] R. Rehm, M. Walther, J. Schmitz, J. Fleissner, J. Ziegler, W. Cabanski, and R. Breiter, "Dual-colour thermal imaging with InAs/GaSb superlattices in mid-wavelength infrared spectral range," *Electron. Lett.*, vol. 42, no. 10, p. 577, 2006.

[57] A. Khoshakhlagh, J. B. Rodriguez, E. Plis, G. D. Bishop, Y. D. Sharma, H. S. Kim, L. R. Dawson, and S. Krishna, "Bias dependent dual band response from InAs/Ga(In)Sb type II strain layer superlattice detectors," *Appl. Phys. Lett.*, vol. 91, no. 26, p. 263504, 2007.

[58] D. Lackner, O. J. Pitts, M. Steger, A. Yang, M. L. W. Thewalt, and S. P. Watkins, "Strain balanced InAs/InAsSb superlattice structures with optical emission to 10 μm," *Appl. Phys. Lett.*, vol. 95, no. 8, p. 081906, 2009.

[59] S. D. Gunapala, D. Z. Ting, C. J. Hill, J. Nguyen, A. Soibel, S. B. Rafol, S. A. Keo, J. M. Mumolo, M. C. Lee, J. K. Liu, B. Yang, and A. Liao, "Demonstration of 1Kx1K long-wave and mid-wave superlattice infrared focal plane arrays," *Proc. SPIE*, San Diego, California, 2010.

[60] E. H. Steenbergen, B. C. Connelly, G. D. Metcalfe, H. Shen, M. Wraback, D. Lubyshev, Y. Qiu, J. M. Fastenau, A. W. K. Liu, S. Elhamri, O. O. Cellek, and Y.-H. Zhang, "Significantly improved minority carrier lifetime observed in a long-wavelength infrared III-V type-II superlattice comprised of InAs/InAsSb," *Appl. Phys. Lett.*, vol. 99, no. 25, p. 251110, 2011.

[61] H. S. Kim, O. O. Cellek, Z.-Y. Lin, Z.-Y. He, X.-H. Zhao, S. Liu, H. Li, and Y.-H. Zhang, "Long-wave infrared nBn photodetectors based on InAs/ InAsSb type-II superlattices," *Appl. Phys. Lett.*, vol. 101, no. 16, p. 161114, 2012.

[62] B. V. Olson, E. A. Shaner, J. K. Kim, J. F. Klem, S. D. Hawkins, L. M. Murray, J. P. Prineas, M. E. Flatté, and T. F. Boggess, "Time-resolved optical measurements of minority carrier recombination in a mid-wave infrared InAsSb alloy and InAs/InAsSb superlattice," *Appl. Phys. Lett.*, vol. 101, no. 9, p. 092109, 2012.

[63] G. Ariyawansa, C. J. Reyner, E. H. Steenbergen, J. M. Duran, J. D. Reding, J. E. Scheihing, H. R. Bourassa, B. L. Liang, and D. L. Huffaker, "InGaAs/InAsSb strained layer superlattices for mid-wave infrared detectors," *Appl. Phys. Lett.*, vol. 108, no. 2, p. 022106, 2016.

[64] N. Yoon, C. J. Reyner, G. Ariyawansa, J. M. Duran, J. E. Scheihing, J. Mabon, and D. Wasserman, "Modified electron beam induced current technique for In(Ga)As/InAsSb superlattice infrared detectors," *J. Appl. Phys.*, vol. 122, no. 7, p. 074053, 2017.

[65] J. Shen, S. Y. Ren, and J. D. Dow, "Deep levels in type-II InAs/GaSb superlattices," *Phys. Rev. B*, vol. 46, no. 12, p. 6938, 1992.

[66] "Closed Cycle Cryogenic Probe Station," https://static1.squarespace.com/static/

59cd15448a02c76b45c2281e/t/5a0b06d7f9619a1bb07939ff/1510672089086/DS-PS-CC.pdf, from Advanced Research Systems.

[67] J. D. Vincent, *Fundamentals of Infrared Detector Operation and Testing*, 1989.

[68] G. Ariyawansa, J. M. Duran, C. J. Reyner, E. H. Steenbergen, N. Yoon, D. Wasserman, and J. E. Scheihing, "Growth and characterization of $In_{1-x}Ga_xAs/InAs_{0.65}Sb_{0.35}$ strained layer superlattice infrared detectors," *Proc. SPIE*, vol. 10177, p. 1017712, 2017.

[69] G. Ariyawansa, M. Grupen, J. M. Duran, J. E. Scheihing, T. R. Nelson, and M. T. Eismann, "Design and modeling of InAs/GaSb type II superlattice based dual-band infrared detectors," *J. Appl. Phys.*, vol. 111, no. 7, p. 073107, 2012.

[70] G. Ariyawansa, E. Steenbergen, L. J. Bissell, J. M. Duran, J. E. Scheihing, and M. T. Eismann, "Absorption characteristics of mid-wave infrared type-II superlattices," *Proc. SPIE*, vol. 9070, p. 90701J, 2014.

[71] L. Jastrzebski, J. Lagowski, and H. C. Gatos, "Application of scanning electron microscopy to determination of surface recombination velocity: GaAs," *Appl. Phys. Lett.*, vol. 27, no. 10, p. 537, 1975.

[72] F. Berz and H. K. Kuiken, "Theory of life time measurements with the scanning electron microscope: Steady state," *Solid-State Electron.*, vol. 19, no. 6, p. 437, 1976.

[73] M. Watanabe, G. Actor, and H. C. Gatos, "Determination of minority-carrier life-time and surface recombination velocity with high spacial resolution," *IEEE Trans. Electron Devices*, vol. 24, no. 9, p. 1172, 1977.

[74] H. J. Leamy, "Charge collection scanning electron microscopy," *J. Appl. Phys.*, vol. 53, no. 6, p. R51, 1982.

[75] C. Donolato, "On the analysis of diffusion length measurements by SEM," *Solid-State Electron.*, vol. 25, no. 11, p. 1077, 1982.

[76] K. L. Luke, O. von Roos, and L.-J. Cheng, "Quantification of the effects of generation volume, surface recombination velocity, and diffusion length on the electron-beam-induced current and its derivative: Determination of diffusion lengths in the low micron and submicron ranges," *J. Appl. Phys.*, vol. 57, no. 6, p. 1978, 1985.

[77] C. Donolato, "Reciprocity theorem for charge collection by a surface with finite collection velocity: Application to grain boundaries," *J. Appl. Phys.*, vol. 76, no. 2, p. 959, 1994.

[78] J.-M. Bonard and J. D. Ganière, "Quantitative analysis of electron-beam-induced current profiles across p-n junctions in GaAs/$Al_{0.4}Ga_{0.6}As$ heterostructures," *J. Appl. Phys.*, vol. 79, no. 9, p. 6987, 1996.

[79] P. R. Edwards, S. A. Galloway, and K. Durose, "EBIC and luminescence mapping of CdTe/CdS solar cells," *Thin Solid Films*, vol. 372, p. 284, 2000.

[80] M. Kittler, W. Seifert, T. Arguirov, I. Tarasov, and S. Ostapenko, "Room-temperature luminescence and electron-beam-induced current (EBIC) recombination behaviour of crystal defects in multicrystalline silicon," *Sol. Energy Mater. Sol. Cells*, vol. 72, p. 465, 2002.

[81] D. Zuo, P. Qiao, D. Wasserman, and S. L. Chuang, "Direct observation of minority carrier lifetime improvement in InAs/GaSb type-II superlattice photodiodes via interfacial layer control," *Appl. Phys. Lett.*, vol. 102, no. 14, p. 141107, 2013.

[82] D. Zuo, R. Liu, D. Wasserman, J. Mabon, Z.-Y. He, S. Liu, Y.-H. Zhang, E. A. Kadlec, B. V. Olsen, and E. A. Shaner, "Direct minority carrier transport characterization of InAs/InAsSb superlattice nBn photodetectors," *Appl. Phys. Lett.*, vol. 106, no. 7, p. 071107, 2015.

[83] O. F. Vyvenko, T. Buonassisi, A. A. Istratov, H. Hieslmair, A. C. Thompson, R. Schindler, and E. R. Weber, "X-ray beam induced current - a synchrotron radiation based technique for the *insitu* analysis of recombination properties and chemical nature of metal clusters in silicon," *J. Appl. Phys.*, vol. 91, no. 6, p. 3614, 2002.

[84] J. Bajaj and W. E. Tennant, "Remote contact LBIC imaging of defects in semiconductors," *J. Cryst. Growth*, vol. 103, p. 170, 1990.

[85] V. I. Orlov, O. V. Feklisova, and E. B. Yakimov, "A Comparison of EBIC, LBIC and XBIC Methods as Tools for Multicrystalline Si Characterization," *Solid State Phenom.*, vol. 205/6, p. 142, 2013.

[86] D. Drouin, A. R. Couture, D. Joly, X. Tastet, V. Aimez, and R. Gauvin, "CASINO V2.42-A Fast and Easy-to-use Modeling Tool for Scanning Electron Microscopy and Microanalysis Users," *Scanning*, vol. 29, no. 3, p. 92, 2007.

[87] O. Marcelot, S. I. Maximenko, and P. Magnan, "Study of CCD Transport on CMOS Imaging Technology: Comparison Between SCCD and BCCD, and Ramp Effect on the CTI," *IEEE Trans. Electron Devices*, vol. 61, no. 3, p. 2437, 2014.

[88] D. L. Smith and C. Mailhot, "Proposal for strained type II superlattice infrared detectors," *J. Appl. Phys.*, vol. 62, no. 6, p. 2545, 1987.

[89] E. R. Youngdale, J. R. Meyer, C. A. Hoffman, F. J. Bartoli, C. H. Grein, P. M. Young, H. Ehrenreich, R. H. Miles, and D. H. Chow, "Auger lifetime enhancement in InAs/$Ga_{1-x}In_xSb$ superlattices," *Appl. Phys. Lett.*, vol. 64, no. 23, p. 3160, 1994.

[90] C. H. Grein, M. E. Flatté, J. T. Olesberg, S. A. Anson, L. Zhang, and T. F. Boggess, "Auger recombination in narrow-gap semiconductor superlattices incorporating antimony," *J. Appl. Phys.*, vol. 92, no. 12, p. 7311, 2002.

[91] H. J. Haugan, F. Szmulowicz, G. J. Brown, and K. Mahalingam, "Band gap tuning of InAs/GaSb type-II superlattices for mid-infrared detection," *J. Appl. Phys.*, vol. 96, no. 5, p. 2580, 2004.

[92] C. H. Grein, J. Garland, and M. E. Flatté, "Strained and Unstrained Layer Superlattices for Infrared Detection," *J. Electron. Mater.*, vol. 38, no. 8, p. 1800, 2009.

[93] B. V. Olson, E. A. Shaner, J. K. Kim, J. F. Klem, S. D. Hawkins, L. M. Murray, J. P. Prineas, M. E. Flatté, and T. F. Boggess, "Time-resolved optical measurements of minority carrier recombination in a mid-wave infrared InAsSb alloy and InAs/InAsSb superlattice," *Appl. Phys. Lett.*, vol. 101, no. 9, p. 092109, 2012.

[94] G. A. Umana-Membreno, B. Klein, H. Kala, J. Antoszewski, N. Gautam, M. N. Kutty, E. Plis, S. Krishna, and L. Faraone, "Vertical minority carrier electron transport in p-type InAs/GaSb type-II superlattices," *Appl. Phys. Lett.*, vol. 101, no. 25, p. 253515, 2012.

[95] B. V. Olson, E. A. Shaner, J. K. Kim, J. F. Klem, S. D. Hawkins, M. E. Flatté, and T. F. Boggess, "Identification of dominant recombination mechanisms in narrow-bandgap InAs/InAsSb type-II superlattices and InAsSb alloys," *Appl. Phys. Lett.*, vol. 103, no. 5, p. 052106, 2013.

[96] B. C. Connelly, G. D. Metcalfe, H. Shen, M. Wraback, C. L. Canedy, I. Vurgaftman, J. S. Melinger, C. A. Affouda, E. M. Jackson, J. A. Nolde, J. R. Meyer, and E. H. Aifer, "Investigation of Trap States in Mid-Wavelength Infrared Type II Superlattices

Using Time-Resolved Photoluminescence," *J. Electron. Mater.*, vol. 42, no. 11, p. 3203, 2013.

[97] Y. Aytac, B. V. Olson, J. K. Kim, E. A. Shaner, S. D. Hawkins, J. F. Klem, M. E. Flatté, and T. F. Boggess, "Effects of layer thickness and alloy composition on carrier lifetimes in mid-wave infrared InAs/InAsSb superlattices," *Appl. Phys. Lett.*, vol. 105, no. 2, p. 022107, 2014.

[98] B. V. Olson, E. A. Kadlec, J. K. Kim, J. F. Klem, S. D. Hawkins, E. A. Shaner, and M. E. Flatté, "Intensity- and Temperature-Dependent Carrier Recombination in InAs/$InAs_{1-x}Sb_x$ Type-II Superlattices," *Phys. Rev. Appl.*, vol. 3, no. 4, p. 044010, 2015.

[99] H. J. Haugan, G. J. Brown, B. V. Olson, E. A. Kadlec, J. K. Kim, and E. A. Shaner, "Minority carrier lifetimes in very long-wave infrared InAs/GaInSb superlattices," *J. Vac. Sci. Technol. B*, vol. 34, no. 2, p. 02L104, 2016.

[100] H. J. Haugan, B. V. Olson, G. J. Brown, E. A. Kadlec, J. K. Kim, and E. A. Shaner, "Significantly enhanced carrier lifetimes of very long-wave infrared absorbers based on strained-layer InAs/GaInSb superlattices," *Opt. Eng.*, vol. 56, no. 9, p. 091604, 2017.

[101] E. H. Steenbergen, K. Nunna, L. Ouyang, B. Ullrich, D. L. Huffaker, D. J. Smith, and Y.-H. Zhang, "Strain-balanced InAs/$InAs_{1x}Sb_x$ type-II superlattices grown by molecular beam epitaxy on GaSb substrates," *J. Vac. Sci. Technol. B*, vol. 30, no. 2, p. 02B107, 2012.

[102] O. Klin, N. Snapi, Y. Cohen, and E. Weiss, "A study of MBE growth-related defects in InAs/GaSb type-II supperlattices for long wavelength infrared detectors," *J. Cryst. Growth*, vol. 425, p. 54, 2015.

[103] H. Kim, Y. Meng, J.-L. Rouviére, D. Isheim, D. N. Seidman, and J.-M. Zuo, "Atomic resolution mapping of interfacial intermixing and segregation in InAs/GaSb superlattices: A correlative study," *J. Appl. Phys.*, vol. 113, no. 10, p. 103511, 2013.

[104] R. K. Ahrenkiel, "Measurement of minority-carrier lifetime by time-resolved photoluminescence," *Solid-State Electron.*, vol. 35, no. 3, p. 239, 1992.

[105] E. A. Kadlec, B. V. Olson, M. D. Goldflam, J. K. Kim, J. F. Klem, S. D. Hawkins, W. T. Coon, M. A. Cavaliere, A. Tauke-Pedretti, T. R. Fortune, C. T. Harris, and E. A. Shaner, "Effects of electron doping level on minority carrier lifetimes in n-type mid-wave infrared InAs/$InAs_{1-x}Sb_x$ type-II superlattices," *Appl. Phys. Lett.*, vol. 109, no. 26, p. 261105, 2016.

[106] D. Z. Ting, A. Soibel, and S. D. Gunapala, "Hole effective masses and subband splitting in type-II superlattice infrared detectors," *Appl. Phys. Lett.*, vol. 108, no. 18, p. 183504, 2016.

[107] F. Szmulowicz, H. J. Haugan, S. Elhamri, and G. J. Brown, "Calculation of vertical and horizontal mobilities in InAs/GaSb superlattices," *Phys. Rev. B*, vol. 84, no. 15, p. 155307, 2011.

[108] F. Szmulowicz and G. J. Brown, "Calculation of interface roughness scattering-limited vertical and horizontal mobilities in InAs/GaSb superlattices as a function of temperature," *J. Appl. Phys.*, vol. 113, no. 1, p. 014302, 2013.

[109] P. C. Klipstein, Y. Benny, S. Gliksman, A. Glozman, E. Hojman, O. Klin, L. Langof, I. Lukomsky, I. Marderfeld, M. Nitzani, N. Snapi, and E. Weiss, "Minority carrier lifetime and diffusion length in type II superlattice barrier devices," *Infrared Phys. Technol.*, vol. 96, p. 155, 2019.

[110] A. Chomette, B. Deveaud, J. Y. Emery, A. Regreny, and B. Lambert, "Vertical transport in GaAs/$Ga_{1-x}Al_xAs$ superlattices observed by photoluminescence," *Sol. St. Commun.*, vol. 54, p. 75, 1985.

[111] B. Lambert, F. Clerot, B. Deveaud, A. Chometlte, G. Talalaeff, A. Regreny, and B. Sermage, "Electron and Hole Transport Properties in GaAs-AlGaAs Superlattices," *J. Lumin.*, vol. 44, p. 277, 1989.

[112] M. P. Lumb, I. Vurgaftman, C. A. Affouda, J. R. Meyer, E. H. Aifer, and R. J. Walters, "Quantum wells and superlattices for III-V photovoltaics and photodetectors," *Proc. SPIE*, vol. 8471, p. 84710A, 20012.

[113] Z.-Y. Lin, S. Liu, E. H. Steenbergen, and Y.-H. Zhang, "Influence of carrier localization on minority carrier lifetime in InAs/InAsSb type-II superlattices," *Appl. Phys. Lett.*, vol. 107, no. 20, p. 201107, 2015.

[114] B. Klein, N. Gautam, E. Plis, T. Schuler-Sandy, T. J. Rotter, S. Krishna, B. C. Connelly, G. D. Metcalfe, P. Shen, and M. Wraback, "Carrier lifetime studies in midwave infrared type-II InAs/GaSb strained layer superlattice," *J. Vac. Sci. Technol. B*, vol. 32, p. 02C101, 2014.

[115] R. U. Martinelli, D. Z. Garbuzov, H. Lee, N. Morris, T. Odubanjo, G. C. Taylor, and J. C. Connolly, "Minority-Carrier Transport in InGaAsSb Thermophotovoltaic Diodes," *AIP Conf. Proc.*, vol. 401, p. 389, 1997.

[116] E. H. Aifer, J. H. Warner, C. L. Canedy, I. Vurgaftman, E. M. Jackson, J. G. Tischler, J. R. Meyer, S. P. Powell, K. Olver, and W. E. Tennant, "Shallow-Etch Mesa Isolation of Graded-Bandgap "W"-Structured Type II Superlattice Photodiodes," *J. Electron. Mater.*, vol. 39, no. 7, p. 1070, 2010.

[117] X. Du, G. R. Savich, B. T. Marozas, and G. W. Wicks, "Suppression of Lateral Diffusion and Surface Leakage Currents in nBn Photodetectors Using an Inverted Design," *J. Electron. Mater.*, vol. 47, no. 2, p. 1038, 2018.

[118] G. J. Sullivan, A. Ikhlassi, J. Bergman, R. E. DeWames, J. R. Waldrop, C. Grein, M. Flatté, K. Mahalingam, H. Yang, M. Zhong, and M. Weimer, "Molecular beam epitaxy growth of high quantum efficiency InAs/GaSb superlattice," *J. Vac. Sci. Technol. B*, vol. 23, no. 3, p. 1144, 2005.

[119] X.-M. Shen, H. Li, S. Liu, D. J. Smith, and Y.-H. Zhang, "Study of InAs/InAsSb type-II superlattices using high-resolution x-ray diffraction and cross-sectional electron microscopy," *J. Cryst. Growth*, vol. 381, p. 1, 2013.

[120] Y. Huang, J.-H. Ryou, R. D. Dupuis, V. R. D'Costa, J. Steenbergen, E. H.and Fan, Y.-H. Zhang, M. Petschke, A.and Mandl, and S.-L. Chuang, "Epitaxial growth and characterization of InAs/GaSb and InAs/InAsSb type-II superlattices on GaSb substrates by metalorganic chemical vapor deposition for long wavelength infrared photodetectors," *J. Cryst. Growth*, vol. 314, no. 1, p. 92, 2011.

[121] H. Katayama, T. Takekawa, M. Kimata, H. Inada, and Y. Iguchi, "Measurement of absorption and external quantum efficiency of an InAs/GaSb Type II superlattice," *Infrared Phys. Technol.*, vol. 70, p. 53, 2015.

[122] A. E. Brown, N. Baril, D. Zuo, L. A. Almeida, J. Arias, and S. Bandara, "Characterization of n-Type and p-Type Long-Wave InAs/InAsSb Superlattices," *J. Electron. Mater.*, vol. 46, no. 9, p. 5367, 2017.

[123] E. H. Steenbergen, S. Elhamri, W. C. Mitchel, S. Mou, and G. J. Brown, "Carrier transport properties of Be-doped InAs/InAsSb type-II infrared superlattices," *Appl. Phys. Lett.*, vol. 104, no. 1, p. 011104, 2014.

[124] C. Donolato, "Reciprocity theorem for charge collection by a surface with finite collection velocity: Application to grain boundaries," *J. Appl. Phys.*, vol. 76, no. 2, p. 959, 1994.

[125] J. Bonard and J. Ganière, "Quantitative analysis of electron-beam-induced-current profiles across p-n junctions in GaAs/$Al_{0.4}Ga_{0.6}As$ heterostructures," *J. Appl. Phys.*, vol. 79, no. 9, p. 6987, 1996.

[126] D. Zuo, R. Liu, D. Wasserman, J. Mabon, Z.-Y. He, S. Liu, Y.-H. Zhang, E. A. Kadlec, B. V. Olson, and E. A. Shaner, "Direct minority carrier transport characterization of InAs/InAsSb superlattice nBn photodetectors," *Appl. Phys. Lett.*, vol. 106, no. 7, p. 071107, 2015.

[127] D. Zuo, P. Qiao, D. Wasserman, and S. L. Chuang, "Direct observation of minority carrier lifetime improvement in InAs/GaSb type-II superlattice photodiodes via interfacial layer control," *Appl. Phys. Lett.*, vol. 102, no. 14, p. 141107, 2013.

[128] I. Vurgaftman, G. Belenky, Y. Lin, D. Donetsky, L. Shterengas, G. Kipshidze, W. L. Sarney, and S. P. Svensson, "Interband absorption strength in long-wave infrared type-II superlattices with small and large superlattice periods compared to bulk materials," *Appl. Phys. Lett.*, vol. 108, no. 22, p. 222101, 2016.

[129] M. D. Goldflam, E. A. Kadlec, B. V. Olson, J. F. Klem, S. D. Hawkins, S. Parameswaran, W. T. Coon, G. A. Keeler, T. R. Fortune, A. Tauke-Pedretti, J. R. Wendt, E. A. Shaner, P. S. Davids, J. K. Kim, and D. W. Peters, "Enhanced infrared detectors using resonant structures combined with thin type-II superlattice absorbers," *Appl. Phys. Lett.*, vol. 109, no. 25, p. 251103, 2016.

[130] J. A. Nolde, M. Ki, C. S. Kim, E. M. Jackson, C. T. Ellis, J. Abell, O. J. Glembocki, C. L. Canedy, J. G. Tischler, I. Vurgaftman, J. R. Meyer, and E. H. Aifer, "Resonant

quantum efficiency enhancement of midwave infrared nBn photodetectors using one-dimensional plasmonic gratings," *Appl. Phys. Lett.*, vol. 106, no. 26, p. 261109, 2015.

[131] S. C. Lee, S. Krishna, and S. R. J. Brueck, "Quantum dot infrared photodetector enhanced by surface plasma wave excitation," *Opt. Express*, vol. 17, no. 25, p. 23160, 2009.

[132] M. Zamiri, E. Plis, J. O. Kim, S. C. Lee, A. Neumann, S. Myers, E. P. Smith, A. M. Itsuno, J. G. A. Wehner, S. M. Johnson, S. R. J. Brueck, and S. Krishna, "MWIR superlattice detectors integrated with substrate side-illuminated plasmonic coupler," *Proc. SPIE*, Baltimore, Maryland, 2014.

[133] W. Streyer, S. Law, G. Rooney, T. Jacobs, and D. Wasserman, "Strong absorption and selective emission from engineered metals with dielectric coatings," *Opt. Express*, vol. 21, no. 7, p. 9113, 2013.

[134] M. A. Kats, R. Blanchard, P. Genevet, and F. Capasso, "Nanometre optical coatings based on strong interference effects in highly absorbing media," *Nat. Mater.*, vol. 12, p. 20, 2013.

[135] S. Law, D. C. Adams, A. M. Taylor, and D. Wasserman, "Mid-infrared designer metals," *Opt. Express*, vol. 20, no. 11, p. 12155, 2012.

[136] S. Law, L. Yu, and D. Wasserman, "Epitaxial growth of engineered metals for mid-infrared plasmonics," *J. Vac. Sci. Technol. B*, vol. 31, no. 3, p. 03C121, 2013.

[137] D. Zuo, P. Xiao, D. Wasserman, and S. L. Chuang, "Direct observation of minority carrier lifetime improvement in InAs/GaSb type-II superlattice photodiodes via interfacial layer control," *Appl. Phys. Lett.*, vol. 102, no. 14, p. 141107, 2013.

[138] S. Law, C. Roberts, T. Kilpatrick, L. Yu, T. Ribaudo, E. A. Shaner, V. Podolskiy,

and D. Wasserman, "All-semiconductor negative-index plasmonic absorbers," *Phys. Rev. Lett.*, vol. 112, no. 1, p. 017401, 2014.

[139] P. B. Johnson and R. W. Christy, "Optical constants of the noble metals," *Phys. Rev. B*, vol. 6, no. 12, p. 4370, 1972.

[140] C. Roberts and V. Podolskiy, "MATLAB implementation of the RCWA numerical method," http://viktor-podolskiy-research.wiki.uml.edu/RCWA, from V. Podolskiy's Research Group.